Stable Oxidative Cytosine Modifications Accumulate in Cardiac Mesenchymal Cells from Type2 Diabetes Patients: Rescue by alpha Ketoglutarate and TET-TDG Functional Reactivation

Stable oxidative cytosine modifications accumulate in cardiac mesenchymal cells from Type2 diabetes patients: rescue by alpha-ketoglutarate and TET-TDG functional reactivation.

Francesco Spallotta[1#], Chiara Cencioni[1#], Sandra Atlante[1], Davide Garella[2], Mattia Cocco[2], Mattia Mori[3], Raffaella Mastrocola[2], Carsten Kuenne[4], Stefan Guenther[4], Simona Nanni[5], Valerio Azzimato[6], Sven Zukunft[1], Angela Kornberger[7], Duran Sürün[1], Frank Schnütgen[1], Harald von Melchner[1], Antonella Di Stilo[2], Manuela Aragno[2], Maarten Braspenning[8], Wim van Criekinge[9], Miles De Blasio[10], Rebecca H. Ritchie[10], Germana Zaccagnini[11], Fabio Martelli[11], Antonella Farsetti[1,12], Ingrid Fleming[1], Thomas Braun[4], Andres Beiras-Fernandez[7], Bruno Botta[13], Massimo Collino[2], Massimo Bertinaria[2], Andreas M. Zeiher[1], Carlo Gaetano[1*]

1 Goethe University, 60596-Frankfurt am Main, Germany.
2 University of Turin 10125-Torino, Italy.
3 Istituto Italiano di Tecnologia, 00161-Rome, Italy.
4 Max Planck Institute for Heart and Lung Research, 61231-Bad Nauheim, Germany.
5 Università Cattolica del Sacro Cuore, Rome, Italy.
6 Karolinska Institutet. 14157-Huddinge, Sweden.
7 University of Mainz, Mainz, Germany.
8 NXT-Dx, Ghent, Belgium.
9 Ghent University, Ghent, Belgium.
10 Baker IDI Heart and Diabetes Institute, 3004-Melbourne VIC, Australia.
11 Policlinico San Donato, San Donato Milanese, 20097-Milan, Italy.
12 National Research Council, Rome, Italy.
13 Sapienza University of Rome, 00185-Rome, Italy.

# Dr. Spallotta and Cencioni contributed equally to this work

*Current address: Laboratorio di Epigenetica, Istituti Clinici Scientifici Maugeri, Via Maugeri 4, Pavia, Italy.

Corresponding authors:
Prof. Carlo Gaetano MD, FAHA.
Division of Cardiovascular Epigenetics, Department of Cardiology, Goethe University, Frankfurt am Main 60590, Germany
E-Mail: gaetano@em.uni-frankfurt.de; Tel.: +49-69-6301-87963; Fax: +49-69-6301-86095.

Dr. Francesco Spallotta, PhD
Division of Cardiovascular Epigenetics, Department of Cardiology, Goethe University, Frankfurt am Main 60590, Germany
E-Mail: fspallotta@gmail.com; Tel.: +49-69-6301-87957; Fax: +49-69-6301-86095.

Running title: Metabolism & DNA methylation.
Keywords: DNA methylation, TET, TDG, α-ketoglutarate, hyperglycemia, diabetes, heart, cardiac fibroblasts.
Subject codes: Metabolism, Epigenetics, Type 2 Diabetes
Word counts: 9871

ABSTRACT

Rationale: Human cardiac mesenchymal cells (CMSCs) are a therapeutically-relevant primary cell population. Diabetes compromises CMSC function as consequence of metabolic alterations and incorporation of stable epigenetic changes.

Objective: To investigate the role of α-ketoglutarate (αKG) in the epi-metabolic control of DNA demethylation in CMSCs.

Methods & results: Quantitative global analysis, methylated and hydroxymethylated DNA sequencing and gene specific GC methylation detection revealed an accumulation of 5mC, 5hmC and 5fC in the genomic DNA of human CMSCs isolated from diabetic (D) donors (D-CMSCs). Whole heart genomic DNA analysis revealed iterative oxidative cytosine modification accumulation in mice exposed to high fat diet (HFD), injected with streptozotocin (STZ) or both in combination (STZ-HFD). In this context, untargeted and targeted metabolomics indicated an intracellular reduction of αKG synthesis in D-CMSCs and in the whole heart of HFD mice. This observation was paralleled by a compromised thymine DNA glycosylase (TDG) and ten eleven translocation protein 1 (TET1) association and function with TET1 relocating out of the nucleus. Molecular dynamics and mutational analyses showed that αKG binds TDG on Arg275 providing an enzymatic allosteric activation. As a consequence, the enzyme significantly increased its capacity to remove G/T nucleotide mismatches or 5fC. Accordingly, an exogenous source of αKG restored the DNA demethylation cycle by promoting TDG function, TET1 nuclear localization and TET/TDG association. TDG inactivation by CRISPR/Cas9 knockout or TET/TDG siRNA knockdown induced 5fC accumulation thus partially mimicking the diabetic epigenetic landscape in cells of non-diabetic origin. The novel compound (S)-2-[(2,6-dichlorobenzoyl)amino]succinic acid (AA6), identified as an inhibitor of αKG-dehydrogenase, increased the αKG level in D-CMSCs and in the heart of HFD and STZ mice eliciting, in HFD, DNA demethylation, glucose uptake and insulin response.

Conclusions: Restoring the epi-metabolic control of DNA demethylation cycle promises beneficial effects on cells compromised by environmental metabolic changes.

INTRODUCTION

Human cardiac mesenchymal cells (CMSCs) do not naturally exert contractile functions and do not spontaneously generate cardiomyocytes. Under appropriate conditions, however, they may be genetically redirected to differentiate into cardiomycytes and contribute *in situ* to cardiac regeneration.[1] These cells are relatively simple to isolate and expand *ex vivo*[2] as a population enriched in cells of mesenchymal origin (≥90% CD29-CD90-CD146 positive).[2] For this reason and thanks to their secretory properties, CMSCs have been recently considered of therapeutic interest for cardiac repair.[3, 4] However, little is still known about the effect of the cardiac metabolic microenvironment on the biological properties of cardiac non-myocyte cell populations.[5]

Clinical trials for type 1 and 2 diabetes demonstrated that early glycemic control reduces incidence and progression of diabetic complication.[6] On the other hand, epidemiological and prospective data revealed that in the cardiovascular system diabetes stressors may persist in spite of glycemic control.[7] Indeed, a prolonged impairment of glucose homeostasis is a condition that often precedes and accompanies obesity, metabolic syndrome, insulin resistance and type 1 and 2 diabetes. The permanent or long-term consequence of an early inefficient glucose handling has been defined as "hyperglycemic memory",[8-10] a phenomenon believed of epigenetic origin[11] where specific changes in the histone code and DNA methylation level may provide the mechanistic basis for the perpetuation of an altered metabolic signals.[12, 13] In spite of some advances, how mechanistically epigenetic changes may affect function of CMSCs is still poorly characterized. Recent work, however, provided some evidence that DNA methylation plays an important role in this process.[14, 15]

The recent discovery of ketoglutaric acid (αKG)-, iron- and oxygen-dependent TET-1,-2,-3 proteins shed light on DNA demethylation mechanisms *via* conversion of 5-methyl-cytosine (5mC) into its oxidized forms such as 5-hydroxymethyl- (5hmC), 5-formyl- (5fC) and 5-carboxyl- (5caC) cytosines.[16] The outcome of this process is active demethylation of targeted DNA regions. Remarkably, once acquired, some of the 5mC iterative modifications, including 5hmC and 5fC, remain stable in the DNA of non-regenerating adult mouse organs including brain and heart.[17, 18]

Several epigenetic enzymes contributes to the DNA demethylation process including members of the AID/APOBEC family and the thymine DNA glycosylase (TDG).[19, 20] In particular, TDG plays a fundamental role, alone or in association with TET1,[21] in the formation of an abasic site that can be reconverted to unmethylated cytosine with the final contribution of the base excision repair (BER) machinery.[22] To our knowledge, TDG has never been reported metabolically regulated. The evidence that it may form a complex with TET1,[21] however, opens up to the possibility that specific pathophysiological metabolic environments, such as those in cancer, chronic inflammation, insulin resistance or diabetes, may have implications on TET/TDG function and DNA demethylation.[23, 24]

In the present work, we took advantage from the possibility to isolate human primary CMSCs from diabetic (D) and non-diabetic (ND) donors analyzing them after few rounds of *ex vivo* expansion. We found that some important epigenetic alterations resided in D-CMSCs compared to ND-CMSCs cultured in the same condition. Information is reported here about how epigenetic changes were determined in D-CMSCs, with special attention paid to the mechanism of iteratively oxidized DNA cytosine accumulation[25], and how to pharmacologically rescue this alteration.

METHODS

An expanded Material and Method section is included in the Online Data Supplement.

RESULTS

Accumulation of methylated cytosines and their iteratively oxidized modifications occurs in human CMSCs from diabetic donors, in the heart of mice with impaired glucose homeostasis and in human endothelial cells exposed to high glucose.

Accumulation of 5mC, and/or that of its oxidized products, 5hmC and 5fC, occurred in the DNA of human CMSCs obtained from type 2 diabetic (D-CMSCs) compared to non-diabetic (ND-CMSCs) donors (Online Table I; Figure 1A-C). Notably, peripheral blood mononuclear cells (PBMCs), isolated from the same diabetic donors did not show a similar pattern for cytosine modifications (Online Figure I A-C). In D-PBMCs, in fact, only 5fC significantly accumulated (Online Figure I C) suggesting this modification as one of the oxidized DNA cytosine modifications most sensitive to the metabolic environment. These observations, about the accretion of 5hmC and 5fC in D-CMSCs, were confirmed at single cell level by in-cell western and confocal analyses (Figure 1D, E). Further, exploring 5mC and 5hmC accumulation in the mitochondrial DNA of a subset of randomly chosen human ND- and D-CMSCs, we found a pronounced accumulation of 5hmC in comparison to 5mC (Online Figure I D, right and left panel respectively). Of note, there were no apparent differences between cultured ND- and D-CMSCs regarding 8-oxoguanine accumulation (not shown).

Remarkably, modifications similar to those present in D-CMSCs were observed in the whole heart and in the brain of different animal models of impaired glucose handling such as in high fat diet (HFD) fed mice, mice injected with high dose streptozotocin (STZ) or treated with low dose STZ plus HFD[26] (Online Figure II A-F; Online Figure XI A-D). Confocal analysis, performed at the latest experimental time points, confirmed the presence of 5hmC also in cardiomyocytes of HFD, STZ and STZ+HFD mice (Figure 6K; Online Figure XI A, B). Because of their intrinsically stable inability to handle blood glucose (Online Figure II E) mice made hyperglycemic by STZ injection were analyzed in greater detail. In them, cardiac DNA hypermethylation, characterized by accumulation of 5mC, 5hmC, and 5fC, became detectable as early as one month after blood glucose rose above 200mg/dL. Interestingly, the level of those cytosine modifications remained relatively stable during a time course from 5 to 25 weeks (Online Figure II G). Accordingly, we found that a monolayer of confluent human endothelial cells (HUVEC), exposed to high glucose (25mM) for 72 hours, rapidly accumulated methylated cytosines and their iteratively oxidized forms (Online Figure II H-J).

An integrated OMIC approach reveals altered functional pathways in human CMSCs of diabetic origin.

The reduced representation of bisulfite genomic sequencing validated the presence of a significant accumulation of 5mC and 5hmC in D-CMSCs. Among the genomic features, modified CpG sequences were abundant in the promoter regions (Figure 2A, B). In particular, the coincident presence of 5mC and 5hmC, interested repressed genes involved in transcriptional processes, proliferation, metabolism and regulation of glucose import (Online Table II), as indicated by gene ontology (GO) analysis (Online Figure III A).

RNA sequencing (RNA-seq), performed in phenotypically consistent but independent subsets of ND- and D-CMSCs, revealed a large number of differentially regulated genes that clearly separated the two populations (Figure 2C; Online Table III). Interestingly, the transcripts upregulated in D-CMSCs were involved in matrix synthesis, cell adhesion, signaling, motility, and apoptosis, consistent with cell activation and death programs (Figure 2D, red bars). The downregulated transcripts (Figure 2D, blue bars), instead, belonged to transcriptional regulation, proliferation, and DNA metabolism, indicative of a potentially causal link with the original pathophysiological environment. Similarly, KEGG pathway analysis indicated extracellular matrix synthesis, cell adhesion, apoptosis and cytoskeletal remodeling as the most represented pathways (Online Figure III B, red bars). Cell metabolism, DNA replication, mismatch, and excision repair were, instead, among the most down-regulated functions in D-CMSCs (Online Figure III B, blue bars). This evidence prompted us to analyze the metabolome of ND- and D-CMSCs in greater detail. Consistent with the genomic and transcriptomic analyses, D- and ND-CMSCs could be well separated according to their origin (Figure 2E). Untargeted metabolomics of D-CMSCs, in fact, indicated a significant underrepresentation of some metabolites (Online Table IV; Online Figure IV A) belonging to the amino acid, energy, carbohydrate, nucleotide and other minor metabolic pathways (Figure 2F). The reduced intracellular content of glucose, pyruvate and αKG was validated by ELISA (Online Figure IV B-D). However, because of its relevance in the regulation of DNA demethylases, we further confirmed the reduction in αKG intracellular content of D-CMSCs by targeted metabolomics (Figure 2G). In D-CMSCs, a significant reduction of isocitrate

dehydrogenease (IDH) activity, the enzyme resposible for αKG synthesis, was detected (Online Figure IV E). A similar finding was observed in HUVEC exposed to high glucose (Online Figure IV F, G).[27]

αKG rescues cellular function in D-CMSCs.

Experiments were performed to evaluate the effect of a cell-permeable modified αKG[28] administered to D-CMSCs as extracellular source. Notably, αKG rescued cell proliferation (Online Figure V A) and glucose uptake (Online Figure V B). Further genome sequencing revealed a significant enrichment in methylated and hydroxymethylated cytosines in the promoter and coding region of the insulin response substrate 1 and 2 genes (Irs1; Irs2) in D-CMSCs (Online Figure III C). Interestingly, αKG significantly reduced levels of methylation and hydroxymethylation on their promoters (Online Figure V C, D) in parallel with an increase in the expression at mRNA level (Online Figure V E).

As a potential read out of cellular function we analyzed the fission/fusion mitochondrial ratio in the presence/absence of αKG. Mitochondrial fission was abundant in isolated D-CMSCs compared to their controls (Online Figure V F-I). However, in the presence of exogenous αKG the number of mitochondrial fusion significantly increased (Online Figure V F, G). This qualitative change was paralleled by a functional recovery as demonstrated by the membrane potential-dependent compound JC-1 green/red color conversion (Online Figure V H, I). To further investigate this aspect we evaluated αKG impact on the expression of molecules involved in the mitochondrial fission/fusion conversion and the rate of oxygen consumption (OCR). Mitofusin1 (Mfn1) was reduced in D-CMSCs conversely the Dynamin-like 1 protein (Drp1), abundant during mitochondrial fission, was significantly increased (Online Figure V J). This phenotype was rescued by αKG treatment. Consistently, OCR returned to control value in the presence of αKG (Online Figure V K). However, exogenous αKG supplementation was of little or no effect on ND-CMSCs in terms of proliferation (Online Figure VI A), mitochondrial structure (Online Figure VI B, C), OCR (Online Figure VI D), and DNA demethylation (Online Figure VI E, F).

TET1/TDG association is compromised in human CMSCs from type 2 diabetes patients.

To further explore TET/TDG activity in CMSCs, total TET and TDG activities were measured in a series of *in vitro* assays. Online Figure VII A and B show that both enzymes were hypo-functioning in D-CMSCs. This finding was paralleled by the evidence that TET1 and TDG did not associate well in D-CMSCs (Online Figure VII C). Intriguingly, experiments with oxalomalic acid, an IDH inhibitor (Online Figure VII D), reproduced the phenotype of D-CMSCs in ND-CMSCs. Specifically, the inhibition of IDH reduced αKG and the TET/TDG association (Online Figure VII E, F). These results suggest that αKG may be important for TET/TDG complex formation and function which is compromised in an αKG reduced intracellular environment such as that of D-CMSCs or in the heart of HFD fed mice (see below).

In order to explore αKG effect, confocal analysis was performed in ND- and D-CMSCs (Figure 3A). As expected, TDG (green) has been found localized into the nucleus. Surprisingly, TET (red) localization was nuclear in ND-CMSCs and cytoplasmic in D-CMSCs. This alteration was rescued by adding an αKG extracellular source (Figure 3A). Interestingly, an extranuclear distribution of TET1 was observed in ND-CMSCs treated with okadaic acid, an inhibitor of cellular phospatases of the PP2a family (Online Figure VII G). These results were consistent with our prior work providing evidence that in human endothelial cells the class II HDAC nuclear localization was sensitive to the action of PP2a phosphatase family.[29]

αKG triggers TET1/TDG complex formation and TDG activation.

Among the multiple roles assigned to αKG, the effect on DNA demethylation was further investigated in our system. Figure 3B and C show that the addition of an exogenous source of αKG to D-CMSCs reduced the presence of 5hmC and 5fC in their genomic DNA as well as that of 5hmC in the mitochondrial one (Online Figure VII H). This observation suggested that the metabolite triggered an active DNA demethylation process in these metabolically compromised cells.

The experimental evidence that αKG induced global DNA demethylation including a significant reduction in 5fC prompted us to consider that TDG itself could be sensitive to the intracellular level of this metabolite. No information, however, is currently available regarding the impact that αKG might have on TET/TDG complex formation[21] or TDG function *per se*. Figure 3D

shows that TET1/TDG association is significantly improved in D-CMSCs by αKG, an evidence paralleled by the intra-nuclear re-localization of TET1 (Figure 3A lower panels). Unexpectedly, Figure 3E shows that an exogenous source of αKG significantly increased TDG activity in cellular extracts obtained from D-CMSCs thus suggesting for a direct effect of this metabolite on TDG.

αKG is an allosteric cofactor of TDG and regulates its activity.

Although no prior knowledge is available about αKG as a potential cofactor/modulator of TDG, we found an αKG binding consensus motif, RxxxxxR,[30] at position 275-281 of the human TDG protein (Figure 4A) similar to that of the RNA demethylase ALKBH5.[30, 31] In this motif, the Arginine at position 275 (Arg275) was the most interspecies conserved residue (Figure 4A). Thus, we speculated that αKG might interact directly with TDG to regulate its function. To explore this possibility we took advantage from molecular dynamic (MD) simulation. αKG was found to rapidly (~10 nanoseconds) approach the TDG protein surface stably binding to the enzyme (Figure 4B). Notably, the metabolite did not access to the catalytic core but remained anchored to the positively charged region at its entrance resulting in a local variation of the electrostatic surface potential (Figure 4C; Online Table V A). A persistent interaction with Arg275 (R275) was established, which was identified as the key determinant for recognition and interaction between αKG and TDG (Figure 4D). The MD analysis of a TDG R275→Ala (A) mutant (TDG^{R275A}) further substantiated this model by showing a complete loss of affinity between αKG and TDG^{R275A} (Online Figure VIII A). Moreover, αKG was unable to recognize a preformed TDG/DNA-5fC complex (Online Figure VIII B). In this context, some H-bond interactions between αKG and TDG resulted in the most populated cluster of MD conformations (37.5% of MD time). Specifically, H-bond interactions were established with Gly156 (also bridged by a water molecule), Asn157, and Ser273 (Online Figure VIII C). In MD simulation, the binding of αKG to TDG induced a slight conformational change in the loops Pro270-Arg281, Gly149-His158, and Asn191-Gly199, possibly allowing the catalytic active site to accommodate a αKG molecule (Online Figure VIII D, E). Further, to identify the potential relevance of αKG-TDG interaction additional MD simulations were performed on: i) TDG and DNA bearing 5fC in the TDG catalytic site (DNA-5fC), the structure was adapted from the protein crystallographic data (ID 3UO7)[22]; ii) the ternary complex TDG/αKG/DNA-5fC. These analyses demonstrated that TDG/αKG preformed complex binds DNA-5fC in a conformationally stable structure (Online Figure VIII F left; Online Table V A). Specifically, αKG, in the most populated cluster of MD conformations (58.5% of MD time), occupied the TDG catalytic pocket without hampering or competing with the binding to 5fC (Online Figure VIII F right). Theoretical affinity calculations (Online Table V B) suggest that, in the presence of αKG, TDG has a reduced affinity for its target DNA. Taken together, MD simulations indicated that αKG does not hamper the excision repair mechanism of TDG; rather it might exert an allosteric function with potential consequences for the catalytic activity turnover of the enzyme.

To validate the MD prediction that αKG modulated TDG affinity for its DNA targets, experiments were performed assessing the effect of exogenous αKG on the efficiency of TDG-dependent base-excision process and abasic sites binding. Here, evidence is provided that in the presence of αKG, a purified recombinant murine TDG protein (mrTDG) recognized more efficiently a DNA oligo bearing a G/T mismatch (Figure 5A). In parallel, the G/T excision activity of mrTDG was increased about three fold by αKG (Figure 5B). Similarly, mrTDG protein recognized genomic DNA abasic site reducing accessibility to the fluorescent ARP probe (Figure 5C, black bar). Interestingly, αKG restored ARP signal to control level (Figure 5C, gray bar) and increased the ability of mrTDG to remove 5fC from a synthetic substrate (Figure 5D). The further evidence that αKG protected the mrTDG protein against degradation in a series of thermal shift experiments (TSA)[32] supported our findings (Figure 5E), about a direct and functionally relevant interaction between αKG and TDG. Conversely, a cell extract thermal shift assay (CETSA),[33] comparing wild-type and TDG^{R275A} as well as TET1 and the TET1 mutant for the αKG responsive residue R2043→A ($TET1^{R2043A}$)[34] showed a complete loss of protection by αKG for both mutated proteins (Figure 5F). In this context, the R275A mutation of TDG abrogated αKG effect, supporting the hypothesis that R275 regulates the interaction of TDG with αKG in the context of a metabolite-dependent allosteric activation of the enzyme (Figure 5G). To explore further this evidence experiments were performed in HEK293T cells in which the endogenous TDG was knocked-out (KO) by CRISPR/Cas9 technology and reconstituted by transfection of wild type or mutant TDG. Figure 5H shows a representative western blotting analysis of two independent TDG^{KO}

clones and their reconstitution by myc-tagged wild type or mutant TDG. Figure 5I shows αKG effect treatment on wild type endogenous TDG before and after reconstitution in the two independent CRISPR/Cas9 clones. Always, in the presence of αKG wild type TDG activity increased twice above the basal level (Figure 5I, grey columns). The TDG^{R275A} mutant, however, abrogated this effect (Figure 5I). Similarly, TDG abrogation prevented αKG from prompting genomic DNA demethylation and specifically the removal of 5fC which accumulated in absence of TDG or in cells reconstituted with the TDG^{R275A} mutant (Figure 5J). Mechanistically, Figure 5K provides the evidence that TDG^{R275A} variant does not complex with TET1 suggesting αKG association with TDG may be important for TET/TDG complex formation and demethylation function. Similar results were obtained by siRNA knock-down of TET and TDG in ND-CMSCs and D-CMSCs. Online Figure IX A-E shows that in siRNA TET/TDG CMSCs 5fC significantly accumulated above control level and αKG response was abrogated. Further, TDG-KO in H9C2 cells differentiated into cardiomyocytes[35, 36] (Online Figure IX F) reproduced the deficient phenotype described above indicating that the TDG is active as a DNA demethylation enzymes also in cells of cardio-myogenic lineage (Online Figure IX G, H).

A synthetic α-ketoglutarate dehydrogenase inhibitor rescues intracellular αKG levels and activates TET/TDG complex formation and function reducing global DNA methylation.

Hereafter, we investigated whether our findings could be translated into a preclinical setting. Intriguingly, in diabetic patients, αKG plasma concentration has been reported to be similar to that of non-diabetic subjects.[37] We extended and confirmed this early observation by using plasma samples collected from donors as well as from HFD mice (Online Figure X A, B). In light of this evidence we reasoned that the intracellular αKG level might be the limiting factor. Considering, in fact, that unmodified αKG is hydrophilic and cannot efficiently cross the plasma membrane[28] it is conceivable that the extracellular part of this metabolite might be ineffective to rescue the alteration in DNA methylation detected in models of impaired glucose homeostasis. To circumvent this problem, we screened a library of small molecules[38] for potential regulators of DNA demethylation and identified (S)-2-[(2,6-dichlorobenzoyl)amino]succinic acid (AA6; Online Figure X C) as a direct interactor of αKG-dehydrogenase complex (OGDH), determined by CETSA[33] (Figure 6A). AA6 acts as an enzyme inhibitor (Figure 6B) able to increase αKG intracellular levels (Figure 6C). In the presence of AA6, TDG activity significantly increased (Figure 6D) while the global DNA content of 5hmC and 5fC was reduced (Figure 6E, F) at an extent similar to that observed after direct administration of the cell-permeable αKG analogue (Figure 3B, C). Notably, a similar effect was obtained in D-CMSCs by siRNA knockdown of OGDH expression as shown in Online Figure X D-F. Specifically, the reduction in OGDH expression and function determined an intracellular accumulation of αKG (Online Figure X E) with a small but significant effect on the total DNA content of 5fC (Online Figure X F).

In vivo, in HFD mice fed for five weeks and treated daily with AA6 (25mg/Kg) for additional five weeks, AA6 increased cardiac αKG levels (Figure 6G), an effect paralleled by the reassembly of TET1/TDG complex (Figure 6H) and TDG activity gain (Figure 6I). In parallel, 5mC, 5hmC and 5fC accumulation was normalized (Figure 6J). This observation was further supported by confocal analysis showing positivity for 5hmC in the nuclei of some cardiomyocytes of HFD, STZ and STZ-HFD mice (Figure 6K; Online Figure XI A, B). The number of these nuclei significantly decreased in HFD animals treated with AA6 (Figure 6K). A similar effect was detected in the genomic DNA obtained from the brain of the same animals where 5hmC and 5fC significantly accumulated and diminished after AA6 treatment (Online Figure XI C, D). Of note, no significant accumulation of modified cytosines was observed in liver with or without AA6, possibly reflecting organ-specific differences in metabolism, pharmacokinetics or cellular turn-over (Online Figure XI C, D).[17, 18]

Interestingly, during the five weeks of AA6 treatment, no adverse reactions to the drug or sudden death episodes occurred. Further, no signs of proliferation or cardiotoxicity were detected (Online Figure XI E, F).

AA6 rescues glucose uptake in D-CMSCs and insulin response in HFD mice promoting Irs-1 and 2 expression.

During the progress of this work, bioinformatic analysis revealed that in D-CMSCs, compared to ND-CMSCs, Irs1 and Irs2 gene loci were enriched in methylated cytosines at their 5'-region (Online Figure III C). In addition, a recent work showed that Irs1 and Irs2 are down regulated in the heart in

consequence of an altered metabolic state, a condition typical of HFD mice.[39] We reasoned that these two genes could be important targets in the glucose response regulation in D-CMSCs and decided to challenge the system with AA6. Remarkably, Irs1 and 2 loci were methylated and hydroxymethylated in D-CMSCs (Online Figure III C). However, AA6 reduced the level of 5mC and 5hmC in the genomic region encompassing Irs1 and Irs2 genes (Online Figure XII A, B) leading to reactivation of gene expression (Online Figure XII C). This effect was paralleled by an increase of intracellular glucose content in D-CMSCs (Online Figure XII D) and a reassessment of the mitochondrial OCR at control level while no significant effect was observed in ND-CMSCs (Online Figure XII E).

Whishing to explore AA6 effect in an *in vivo* context, a series of experiments were performed in mice exposed to HFD in the presence or absence of the drug. Figure 7A shows the results of RNAseq related to the whole heart of HFD±AA6 mice compared to control condition. Data indicate that HFD significatly changed the pattern of cardiac transcripts which was rescued in HFD animals injected with AA6 (Online Table VI; Figure 7A). In this context GO analysis revelead that some transcripts associated with important cardiac functions including contractility, metabolism and homestasis were compromised (Figure 7B). Notably, treatment with AA6 restored these pathways at control levels with a predominant transcriptional effect on the expression of genes encoding for components of the sarcomeres, or proteins involved in calcium handling and cardiac differentiation (Figure 7C). Interestingly, this pattern was at least in part similar to that observed in the transcriptomic analysis of ND- and D-CMSCs (Figure 2D). To explore further the basis of AA6 beneficial effect we measured the cardiac accumulation of advanced glycation end-products (AGEs), the body weight gain and blood gylcemia basal level in HFD mice with or without AA6. In all cases we observed a positive effect. Specifically, AGE accumulation was reduced in HFD animals treated with AA6 (Figure 7D) as well as the body weight gain and the total blood glycemia that showed a significant amelioration in the presence of the drug (Figure 7E, F). Further, the effect of AA6 was paralleled by a normalization of the glucose uptake curve (Figure 7G) and the insulin levels (Figure 7H) suggesting for a positive influence on the systemic insulin response. To explore this possibility RNAseq was performed on total RNA extracted from mouse skeletal muscle (Online Table VII; Figure 7I). Similarly to the heart, AA6 treatment had an effect on gene expression with a partial rescue at control level (Figure 7I). GO analysis indicated that signaling pathways associated with insulin response, metabolism and differentation processes were, in fact, depressed in HFD fed mice (Figure 7J). However this effect was reverted by AA6 treatment (Figure 7K). Importantly, as seen in D-CMSCs AA6 promoted Irs1 and Irs2 expression in the skeletal muscle and in the heart of HFD+AA6 treated animals (Figure 7L).

Additional experiments, performed in mice made hyperglycemic by STZ and evaluated after three months from injection showed that AA6 failed to restore normal blood glucose (Online Figure XIII A). Nevertheless the DNA demethylation determined by AA6 treatment occurred in the heart in spite the presence of high blood glucose (Online Figure XIII B-D). This effect was paralleled by an increase of total cardiac αKG level similarly to that seen in HFD mice treated with the drug (see Online Figure XIII E and Figure 6G respectively).

DISCUSSION

Mesenchymal cells are abundant in the cardiac stroma and may either represent a source of regenerating material in the occasion of heart damage as well as a potential problem in several pathophysiological conditions leading to fibrosis and heart failure.[5, 40, 41] In spite of its relevance, little is known about the effect of chronic diseases or metabolic derangements on cardiac stroma and its cellular components. Our prior work, reported that cardiac mesenchymal cells isolated from patients with clinical history of diabetes and cultured *ex vivo* demonstrated a variety of epigenetic alterations including the accumulation of specific histone code modifications and DNA cytosine methylation at cell cycle gene promoters.[14] These observations were compatible with the presence of a hyperglycemic/epigenetic memory phenotype in cells originating from diabetic donors. Recently, we observed that a similar epigenetic landscape was reproduced in the heart of mice after that hyperglycemia was caused by STZ injection (see this work and ref.[42]). This finding reinforced the concept that, in absence of other pathophysiological conditions, a prolonged period of uncontrolled hyperglycemia[9, 10, 15, 43, 44] could be sufficient to trigger for the introduction of stable and transmissible epigenetic modifications at cellular and organismal level.[17, 18]

Here, we investigated this hypothesis in the attempt to provide mechanistic information about those signals contributing to the accumulation of epigenetic modifications in human CMSCs. Specifically, attention has been paid to those changes having a direct impact on DNA structure and function such as cytosine methylation and its iterative oxidized modifications that have been recently implicated in epigenetic memory transmission.[45]

DNA methylation is emerging as an important epigenetic modification introduced and regulated by a complex network of enzymes whose activity depends on cofactors, such as S-adenosylmethionine (SAM) or αKG, synthesized during metabolic processes.[46] Specifically, αKG can regulate DNA and histone methylation level acting on TET-1,2,3 and histone lysine demethylases 2-7 (KDM2/7), all members of the so called 2-oxoglutarate-dependent dioxygenase (2-OGDO) family.[47] In particular, TET proteins are responsible of the DNA demethylation process introducing iterative oxidized variants of 5mC like 5hmC, 5fC and 5caC that are preparatory for the final removal of the modified cytosine and the reintroduction of the original unmethylated residue.[20] Indeed, variation in the αKG availability or synthesis may affect DNA methylation, gene expression and cellular differentiation.[48, 49]

The recent identification of different iterative cytosine modifications immediately opened the question about their functional role in the regulation of gene expression and their relevance in pathophysiological conditions such as cancer, cardiovascular diseases or diabetes.[50, 51] Despite a body of literature indicates that an altered DNA methylation pattern exists in all these situations, the role of the iteratively oxidized cytosine modifications remains unclear.[52] In cancer, the presence of mutations in TET2 gene suggests that its product may be crucial in the process of cellular transformation which may be, at least in part, associated with a deregulated rate of 5mC→5hmC conversion and/or that of other subsequent modifications.[53-55] Altogether, the evidence of a deregulation of DNA demethylation through mutations in TET enzymes and/or in the IDH genes, the enzymes deputed to the synthesis of their cofactor αKG, may provide a new conceptual framework for a better understanding of the interplay among metabolism, DNA methylation and the onset of specific diseases.[56] Once acquired, in fact, DNA methylation modifications, such as 5hmC and 5fC, are believed to be stable possibly contributing to epigenetic memory establishment,[43, 46, 48, 49] a condition still mechanistically poorly understood and largely underestimated at clinical level.

The DNA demethylation process not only requires TET proteins but, to complete the demethylation cycle, other enzymes including TDG must contribute. TDG, in fact, works with TET1 to facilitate 5fC and 5caC removal from genomic DNA[21, 22] generating abasic sites prone to the reconstitution of unmethylated G:C sequences by members of the AID/APOBEC and BER machinery.[57] With a similar mechanism, TDG also removes thymine, uracil and 5-bromouracil from mispairings with guanine and plays a central role in cellular defense against genetic mutation caused by spontaneous deamination of 5mC or cytosine. Of note, when TDG is hypo-functional, a relative genome enrichment in 5fC has been observed.[58]

Although associated to a metabolite-dependent protein such as TET1,[21] TDG is not known to require metabolites and/or metals to exert its function. In light of this evidence, the finding described in this manuscript about the TDG association with αKG, which acts as an enzyme allosteric activator, is novel and may contribute to understand how iteratively oxidized cytosines accumulate in cells from the heart of diabetic donors or in organs of animals with impaired glucose handling. In these conditions, TET1/TDG complex is reduced and TDG function compromised. This is a scenario compatible with a defective removal step leading to upstream modified cytosines accumulation. Additionally, prediction analysis suggested that in the presence of αKG the energy of the TDG-DNA-5fC complex increases (Online Table V A). This prediction, the mutation analysis and the functional evidence of a higher efficiency in mismatched thymine and 5fC removal further support the role of αKG in TDG regulation. Of note, TDG has an intrinsically elevated affinity for the abasic sites that it creates.[6,67] This association may slow down TDG catalytic turnover requiring post-translational modifications (e.g. ubiquitination) and the contribution of other DNA repair enzymes to facilitate TDG release from its target.[59, 60] On the contrary, the allosteric effect of αKG may improve TDG detachment from apyrimidinic sites as suggested by the abasic site measurement. Hence, we speculate here that, although αKG may not be necessary for TDG basal activity, it may be important for its optimal functional turnover.[61] Our observation, may, in fact, represent a case of “assisted allosteric activation” similar to that reported for

the epigenetic enzyme Sirtuin 1 that increases its activity in the presence of synthetic ligands binding the molecule to a single amminoacid outside the catalytic site.[62]

Noteworthy, during the progress of our work we identified a new small molecule inhibitor of OGDH, AA6, that acting along the αKG pathway, increased the intracellular αKG, TDG activity and DNA demethylation *in vitro* and *in vivo*. Similarly, OGDH siRNA knockdown largely reproduced the effect of AA6 in CMSCs further supporting the specificity of the new molecule and suggesting a role for OGDH in the control of DNA methylation/demethylation cycle. Indeed, in the presence of AA6, the genomic content of methylated and oxidized cytosines was significantly reduced with evident reactivation signs of the insulin response pathway in D-CMSCs and HFD mice possibly *via* Irs1 and Irs2 re-expression. In parallel, a beneficial effect has been observed on blood glucose and insulin level as well as body weight gain and glucose response curve. Although it remains unclear whether this metabolic amelioration has been achieved exclusively through OGDH inhibition and αKG intracellular accumulation or whether AA6 may have additional effects, based on our findings we may speculate that a dysregulation of IDH-αKG-OGDH metabolic axis may contribute to the onset of insulin resistance or other metabolic dysfunctions associated to an altered glucose homeostasis. This line of thinking is further reinforced by the evidence that in mice with prolonged hyperglycemia, evaluated after three month from STZ injection, AA6 determined cardiac DNA demethylation in absence of blood glucose normalization. Although more experiments are necessary to fully understand AA6 properties, it is coincivable that it might be the increase in αKG level to determine the beneficial action of this OGDH inhibitor.

Yu Q. *et al* reported recently that oxidative stress associated to diabetes in mice may introduce nitrated residues into OGDH protein with potential consequences on the enzyme function.[63] Our observations, in fact, indicate that the metabolic impairment, associated with the exposure to elevated glucose levels, could lead to variations in the intracellular level of key metabolites, including αKG,[64] that in turn could be the *primum movens* underlying the epigenetic DNA modifications possibly associated with an altered glucose homestasis.[9, 10] αKG response abrogation in the presence of the TDG mutant R275A, TET/TDG complex dissociation determined by the αKG synthesis inhibitor oxalomalic acid, methylated DNA accumulation seen in the heart of HFD mice and in cellular models where TET/TDG complex was genetically targeted are in favor of an important role of αKG contributing to DNA maintenance in our experimental systems.

In conclusion, as depicted in Online Figure XIV, this study suggests that pathophysiological conditions associated with impaired glucose homeostasis, such as diabetes, may trigger signals in the heart and other organs leading to DNA demethylation machinery alterations as consequence of reduced intracellular αKG content, impaired TDG activity and 5mC, 5hmC and 5fC accumulation. These alterations are well detectable *ex vivo* in human CMSCs obtained from diabetic donors and, in our opinion, their damaging effect should be taken under consideration in the context of potential therapeutic applications. In light of this evidence, the new compound AA6 may represent a prototypic metabolic enhancer of DNA demethylation and a new tool to explore the mechanism leading to the incorporation of stable DNA cytosine modifications in cells and tissues. Further experiments are required to elucidate whether αKG level regulation *via* a calibrated OGDH functional control may represent a new direction for the development of epi-metabolic drugs aimed at preventing/reducing consequences of an altered glucose handling. Indeed, the metabolic modulators of DNA demethylation may open novel avenues to the prevention or treatment of the genomic consequences associated with chronic diseases including the functional rescue of therapeutically relevant cardiac cells.[4]

Sources of Funding

The present study was supported by LOEWE Cell & Gene Therapy Center (LOEWE-CGT) Goethe University Frankfurt to C.G. and by Deutsche Forschungsgemeinschaft Program SFB834 “Endothelial Signaling and Vascular Repair,” project A9 to I.F., and project B11 to C.G. F.S. is the recipient of the LOEWE CGT grant # III L 5 - 518/17.004 (2013) and funded by the DFG (German Research Foundation), “Excellence Cluster Cardio Pulmonary System.” C.C. is the recipient of the Start-up grant 2016 from LOEWE-Forschungszentrum für Zell- und Gentherapie, gefördert durch das Hessische Ministerium für Wissenschaft und Kunst. Aktenzeichen: III L 5 - 518/17.004 (2013). The present study was supported by Università degli Studi di Torino, Ricerca Locale “Quota B” 2013 to D.G. and “Quota

A" 2015 to M.B. and M.Co., by Italian Ministry of Education, University and Research FIRB-MIUR RBFR10URHP_002 and Italian Ministry of Health GR 2011-02351557 to S.N. and RF 2010-2318330 to A.F. This work was supported by Ministero della Salute, (Ricerca Corrente, 5X1000, RF-2011-02347907 and PE-2011-02348537), Telethon-Italy (grant#GGP14092), and AFM Telethon (grant #18477) to F.M.

Disclosures
None

References

1. Song K, Nam YJ, Luo X, Qi X, Tan W, Huang GN, Acharya A, Smith CL, Tallquist MD, Neilson EG, Hill JA, Bassel-Duby R, Olson EN. Heart repair by reprogramming non-myocytes with cardiac transcription factors. *Nature*. 2012;485:599-604
2. Rossini A, Frati C, Lagrasta C, Graiani G, Scopece A, Cavalli S, Musso E, Baccarin M, Di Segni M, Fagnoni F, Germani A, Quaini E, Mayr M, Xu Q, Barbuti A, DiFrancesco D, Pompilio G, Quaini F, Gaetano C, Capogrossi MC. Human cardiac and bone marrow stromal cells exhibit distinctive properties related to their origin. *Cardiovasc Res*. 2011;89:650-660
3. Guo Y, Wysoczynski M, Nong Y, Tomlin A, Zhu X, Gumpert AM, Nasr M, Muthusamy S, Li H, Book M, Khan A, Hong KU, Li Q, Bolli R. Repeated doses of cardiac mesenchymal cells are therapeutically superior to a single dose in mice with old myocardial infarction. *Basic Res Cardiol*. 2017;112:18
4. Wysoczynski M, Guo Y, Moore JBt, Muthusamy S, Li Q, Nasr M, Li H, Nong Y, Wu W, Tomlin AA, Zhu X, Hunt G, Gumpert AM, Book MJ, Khan A, Tang XL, Bolli R. Myocardial reparative properties of cardiac mesenchymal cells isolated on the basis of adherence. *J Am Coll Cardiol*. 2017;69:1824-1838
5. Cencioni C, Atlante S, Savoia M, Martelli F, Farsetti A, Capogrossi MC, Zeiher AM, Gaetano C, Spallotta F. The double life of cardiac mesenchymal cells: Epimetabolic sensors and therapeutic assets for heart regeneration. *Pharmacol Ther*. 2016
6. White NH, Sun W, Cleary PA, Tamborlane WV, Danis RP, Hainsworth DP, Davis MD, Group D-ER. Effect of prior intensive therapy in type 1 diabetes on 10-year progression of retinopathy in the dcct/edic: Comparison of adults and adolescents. *Diabetes*. 2010;59:1244-1253
7. Zhang L, Chen B, Tang L. Metabolic memory: Mechanisms and implications for diabetic retinopathy. *Diabetes Res Clin Pract*. 2012;96:286-293
8. Roy S, Sala R, Cagliero E, Lorenzi M. Overexpression of fibronectin induced by diabetes or high glucose: Phenomenon with a memory. *Proceedings of the National Academy of Sciences of the United States of America*. 1990;87:404-408
9. Cencioni C, Spallotta F, Greco S, Martelli F, Zeiher AM, Gaetano C. Epigenetic mechanisms of hyperglycemic memory. *The international journal of biochemistry & cell biology*. 2014;51:155-158
10. El-Osta A. Glycemic memory. *Curr Opin Lipidol*. 2012;23:24-29
11. Cooper ME, El-Osta A. Epigenetics: Mechanisms and implications for diabetic complications. *Circ Res*. 2010;107:1403-1413
12. Keating ST, Plutzky J, El-Osta A. Epigenetic changes in diabetes and cardiovascular risk. *Circ Res*. 2016;118:1706-1722
13. Rodriguez H, Rafehi H, Bhave M, El-Osta A. Metabolism and chromatin dynamics in health and disease. *Mol Aspects Med*. 2017;54:1-15
14. Vecellio M, Spallotta F, Nanni S, Colussi C, Cencioni C, Derlet A, Bassetti B, Tilenni M, Carena MC, Farsetti A, Sbardella G, Castellano S, Mai A, Martelli F, Pompilio G, Capogrossi MC, Rossini A, Dimmeler S, Zeiher A, Gaetano C. The histone acetylase activator pentadecylidenemalonate 1b rescues proliferation and differentiation in the human cardiac mesenchymal cells of type 2 diabetic patients. *Diabetes*. 2014;63:2132-2147
15. Keating ST, El-Osta A. Epigenetic changes in diabetes. *Clin Genet*. 2013;84:1-10
16. Ito S, D'Alessio AC, Taranova OV, Hong K, Sowers LC, Zhang Y. Role of tet proteins in 5mc to 5hmc conversion, es-cell self-renewal and inner cell mass specification. *Nature*. 2010;466:1129-1133
17. Bachman M, Uribe-Lewis S, Yang X, Burgess HE, Iurlaro M, Reik W, Murrell A, Balasubramanian S. 5-formylcytosine can be a stable DNA modification in mammals. *Nat Chem Biol*. 2015;11:555-557

18. Bachman M, Uribe-Lewis S, Yang X, Williams M, Murrell A, Balasubramanian S. 5-hydroxymethylcytosine is a predominantly stable DNA modification. *Nat Chem*. 2014;6:1049-1055
19. Scourzic L, Mouly E, Bernard OA. Tet proteins and the control of cytosine demethylation in cancer. *Genome Med*. 2015;7:9
20. Shen L, Song CX, He C, Zhang Y. Mechanism and function of oxidative reversal of DNA and rna methylation. *Annu Rev Biochem*. 2014;83:585-614
21. Weber AR, Krawczyk C, Robertson AB, Kusnierczyk A, Vagbo CB, Schuermann D, Klungland A, Schar P. Biochemical reconstitution of tet1-tdg-ber-dependent active DNA demethylation reveals a highly coordinated mechanism. *Nat Commun*. 2016;7:10806
22. Zhang L, Lu X, Lu J, Liang H, Dai Q, Xu GL, Luo C, Jiang H, He C. Thymine DNA glycosylase specifically recognizes 5-carboxylcytosine-modified DNA. *Nat Chem Biol*. 2012;8:328-330
23. Chia N, Wang L, Lu X, Senut MC, Brenner C, Ruden DM. Hypothesis: Environmental regulation of 5-hydroxymethylcytosine by oxidative stress. *Epigenetics*. 2011;6:853-856
24. Efimova EV, Takahashi S, Shamsi NA, Wu D, Labay E, Ulanovskaya OA, Weichselbaum RR, Kozmin SA, Kron SJ. Linking cancer metabolism to DNA repair and accelerated senescence. *Mol Cancer Res*. 2016;14:173-184
25. Klungland A, Robertson AB. Oxidized c5-methyl cytosine bases in DNA: 5-hydroxymethylcytosine; 5-formylcytosine; and 5-carboxycytosine. *Free Radic Biol Med*. 2016
26. Luo J, Quan J, Tsai J, Hobensack CK, Sullivan C, Hector R, Reaven GM. Nongenetic mouse models of non-insulin-dependent diabetes mellitus. *Metabolism*. 1998;47:663-668
27. Kil IS, Lee JH, Shin AH, Park JW. Glycation-induced inactivation of nadp(+)-dependent isocitrate dehydrogenase: Implications for diabetes and aging. *Free Radic Biol Med*. 2004;37:1765-1778
28. MacKenzie ED, Selak MA, Tennant DA, Payne LJ, Crosby S, Frederiksen CM, Watson DG, Gottlieb E. Cell-permeating alpha-ketoglutarate derivatives alleviate pseudohypoxia in succinate dehydrogenase-deficient cells. *Mol Cell Biol*. 2007;27:3282-3289
29. Illi B, Dello Russo C, Colussi C, Rosati J, Pallaoro M, Spallotta F, Rotili D, Valente S, Ragone G, Martelli F, Biglioli P, Steinkuhler C, Gallinari P, Mai A, Capogrossi MC, Gaetano C. Nitric oxide modulates chromatin folding in human endothelial cells via protein phosphatase 2a activation and class ii histone deacetylases nuclear shuttling. *Circ Res*. 2008;102:51-58
30. Fu Y, Dominissini D, Rechavi G, He C. Gene expression regulation mediated through reversible m(6)a rna methylation. *Nat Rev Genet*. 2014;15:293-306
31. Feng C, Liu Y, Wang G, Deng Z, Zhang Q, Wu W, Tong Y, Cheng C, Chen Z. Crystal structures of the human rna demethylase alkbh5 reveal basis for substrate recognition. *J Biol Chem*. 2014;289:11571-11583
32. Lo MC, Aulabaugh A, Jin G, Cowling R, Bard J, Malamas M, Ellestad G. Evaluation of fluorescence-based thermal shift assays for hit identification in drug discovery. *Anal Biochem*. 2004;332:153-159
33. Martinez Molina D, Jafari R, Ignatushchenko M, Seki T, Larsson EA, Dan C, Sreekumar L, Cao Y, Nordlund P. Monitoring drug target engagement in cells and tissues using the cellular thermal shift assay. *Science*. 2013;341:84-87
34. Wu H, Zhang Y. Mechanisms and functions of tet protein-mediated 5-methylcytosine oxidation. *Genes Dev*. 2011;25:2436-2452
35. Barbati SA, Colussi C, Bacci L, Aiello A, Re A, Stigliano E, Isidori AM, Grassi C, Pontecorvi A, Farsetti A, Gaetano C, Nanni S. Transcription factor crem mediates high glucose response in cardiomyocytes and in a male mouse model of prolonged hyperglycemia. *Endocrinology*. 2017
36. Kimes BW, Brandt BL. Properties of a clonal muscle cell line from rat heart. *Exp Cell Res*. 1976;98:367-381
37. Smith MJ, Taylor KW. Blood pyruvate and alpha-ketoglutarate in normal and diabetic subjects. *Br Med J*. 1956;2:1035-1038
38. Garella D, Atlante S, Borretto E, Cocco M, Giorgis M, Costale A, Stevanato L, Miglio G, Cencioni C, de Gortari EF, Medina-Franco JL, Spallotta F, Gaetano C, Bertinaria M. Design and synthesis of n-benzoyl amino acid derivatives as DNA methylation inhibitors. *Chem Biol Drug Des*. 2016
39. Qi Y, Xu Z, Zhu Q, Thomas C, Kumar R, Feng H, Dostal DE, White MF, Baker KM, Guo S. Myocardial loss of irs1 and irs2 causes heart failure and is controlled by p38alpha mapk during insulin resistance. *Diabetes*. 2013;62:3887-3900
40. Travers JG, Kamal FA, Robbins J, Yutzey KE, Blaxall BC. Cardiac fibrosis: The fibroblast awakens. *Circ Res*. 2016;118:1021-1040
41. Zeisberg EM, Kalluri R. Origins of cardiac fibroblasts. *Circ Res*. 2010;107:1304-1312
42. Saviana A. Barbati CC, Lorenza Bacci, Aurora Aiello, Agnese Re, Egidio Stigliano, Andrea M. Isidori, Claudio Grassi, Alfredo Pontecorvi, Antonella Farsetti, Carlo Gaetano, Simona Nanni. Transcription

factor crem mediates high glucose response in cardiomyocytes and in a male mouse model of prolonged hyperglycemia *Endocrinology*. 2017 in press
43. Intine RV, Sarras MP, Jr. Metabolic memory and chronic diabetes complications: Potential role for epigenetic mechanisms. *Curr Diab Rep*. 2012;12:551-559
44. Jayaraman S. Epigenetic mechanisms of metabolic memory in diabetes. *Circ Res*. 2012;110:1039-1041
45. Blomen VA, Boonstra J. Stable transmission of reversible modifications: Maintenance of epigenetic information through the cell cycle. *Cell Mol Life Sci*. 2011;68:27-44
46. Salminen A, Kaarniranta K, Hiltunen M, Kauppinen A. Krebs cycle dysfunction shapes epigenetic landscape of chromatin: Novel insights into mitochondrial regulation of aging process. *Cell Signal*. 2014;26:1598-1603
47. Mantri M, Zhang Z, McDonough MA, Schofield CJ. Autocatalysed oxidative modifications to 2-oxoglutarate dependent oxygenases. *FEBS J*. 2012;279:1563-1575
48. Gillberg L, Ling C. The potential use of DNA methylation biomarkers to identify risk and progression of type 2 diabetes. *Front Endocrinol (Lausanne)*. 2015;6:43
49. Yara S, Lavoie JC, Levy E. Oxidative stress and DNA methylation regulation in the metabolic syndrome. *Epigenomics*. 2015;7:283-300
50. Al-Mahdawi S, Virmouni SA, Pook MA. The emerging role of 5-hydroxymethylcytosine in neurodegenerative diseases. *Front Neurosci*. 2014;8:397
51. Liyanage VR, Jarmasz JS, Murugeshan N, Del Bigio MR, Rastegar M, Davie JR. DNA modifications: Function and applications in normal and disease states. *Biology (Basel)*. 2014;3:670-723
52. Greco CM, Kunderfranco P, Rubino M, Larcher V, Carullo P, Anselmo A, Kurz K, Carell T, Angius A, Latronico MV, Papait R, Condorelli G. DNA hydroxymethylation controls cardiomyocyte gene expression in development and hypertrophy. *Nat Commun*. 2016;7:12418
53. Joshi O, Wang SY, Kuznetsova T, Atlasi Y, Peng T, Fabre PJ, Habibi E, Shaik J, Saeed S, Handoko L, Richmond T, Spivakov M, Burgess D, Stunnenberg HG. Dynamic reorganization of extremely long-range promoter-promoter interactions between two states of pluripotency. *Cell Stem Cell*. 2015;17:748-757
54. Kolodziejczyk AA, Kim JK, Tsang JC, Ilicic T, Henriksson J, Natarajan KN, Tuck AC, Gao X, Buhler M, Liu P, Marioni JC, Teichmann SA. Single cell rna-sequencing of pluripotent states unlocks modular transcriptional variation. *Cell Stem Cell*. 2015;17:471-485
55. Nakajima H, Kunimoto H. Tet2 as an epigenetic master regulator for normal and malignant hematopoiesis. *Cancer Sci*. 2014;105:1093-1099
56. Delatte B, Fuks F. Tet proteins: On the frenetic hunt for new cytosine modifications. *Brief Funct Genomics*. 2013;12:191-204
57. Krokan HE, Bjoras M. Base excision repair. *Cold Spring Harb Perspect Biol*. 2013;5:a012583
58. Wu H, Wu X, Zhang Y. Base-resolution profiling of active DNA demethylation using mab-seq and camab-seq. *Nat Protoc*. 2016;11:1081-1100
59. Hardeland U, Steinacher R, Jiricny J, Schar P. Modification of the human thymine-DNA glycosylase by ubiquitin-like proteins facilitates enzymatic turnover. *EMBO J*. 2002;21:1456-1464
60. Fitzgerald ME, Drohat AC. Coordinating the initial steps of base excision repair. Apurinic/apyrimidinic endonuclease 1 actively stimulates thymine DNA glycosylase by disrupting the product complex. *J Biol Chem*. 2008;283:32680-32690
61. Bellacosa A, Drohat AC. Role of base excision repair in maintaining the genetic and epigenetic integrity of cpg sites. *DNA Repair (Amst)*. 2015;32:33-42
62. Hubbard BP, Gomes AP, Dai H, Li J, Case AW, Considine T, Riera TV, Lee JE, E SY, Lamming DW, Pentelute BL, Schuman ER, Stevens LA, Ling AJ, Armour SM, Michan S, Zhao H, Jiang Y, Sweitzer SM, Blum CA, Disch JS, Ng PY, Howitz KT, Rolo AP, Hamuro Y, Moss J, Perni RB, Ellis JL, Vlasuk GP, Sinclair DA. Evidence for a common mechanism of sirt1 regulation by allosteric activators. *Science*. 2013;339:1216-1219
63. Yu Q, Liu B, Ruan D, Niu C, Shen J, Ni M, Cong W, Lu X, Jin L. A novel targeted proteomics method for identification and relative quantitation of difference in nitration degree of ogdh between healthy and diabetic mouse. *Proteomics*. 2014;14:2417-2426
64. Morgan PE, Sheahan PJ, Pattison DI, Davies MJ. Methylglyoxal-induced modification of arginine residues decreases the activity of nadph-generating enzymes. *Free Radic Biol Med*. 2013;61:229-242

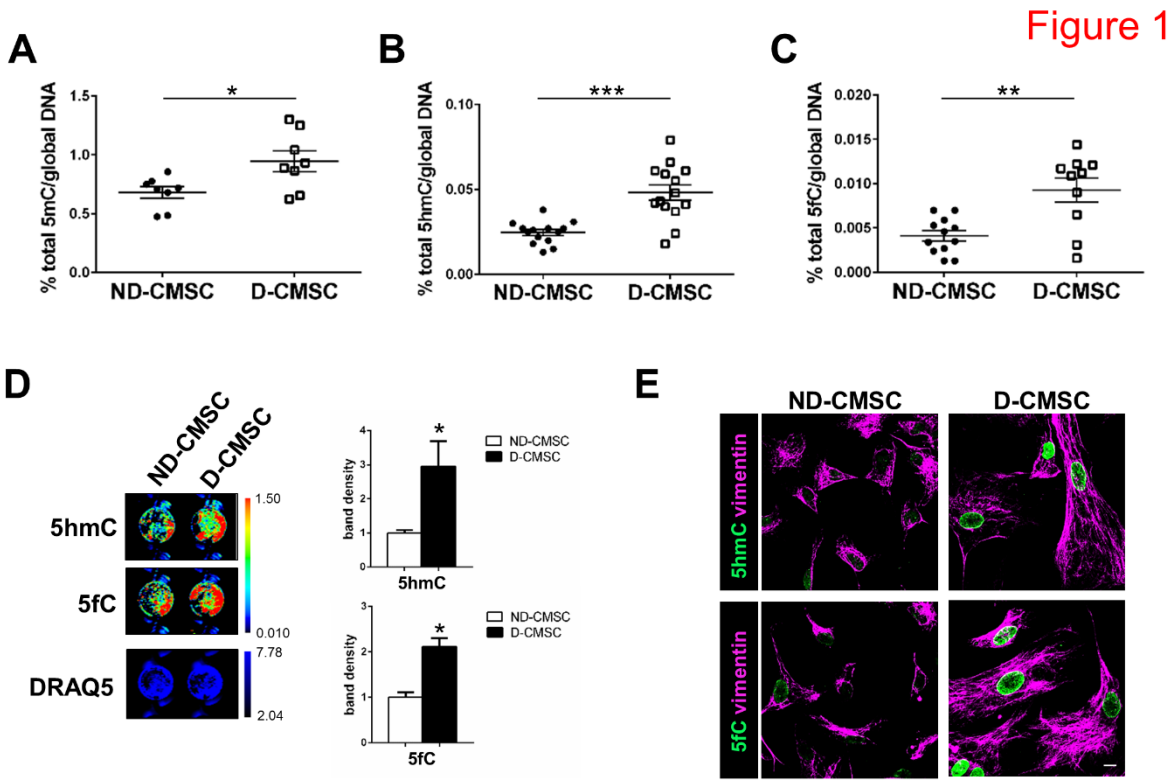

Figure 1
Global 5´cytosine modification increase in human cardiac mesenchymal cells from diabetic donors. (A) Quantification of 5mC (n=8), **(B)** 5hmC (n=14) and **(C)** 5fC (n=12) in CMSCs isolated from non-diabetic (ND-; black circles) and diabetic (D-; white squares) donors. **(D)** Left panel: Representative ICW analysis of ND- and D-CMSCs probed with anti-5hmC and 5fC antibodies. Signals normalized to DNA content according DRAQ5 staining. Right panels: densitometry of three independent experiments. **(E)** Representative confocal microscopy images depicting the intracellular content of 5hmC and 5fC in ND- and D-CMSCs. Cells probed by anti-5hmC antibody (green; upper panels) and anti-5fC antibody (green; lower panels) and counterstained with vimentin (purple). Scale bar 10µm. Error bars indicate SE. *p<0.05; **p<0.01; ***p<0.001. Data analyzed by Kolmogorov-Smirnov test.

Figure 2

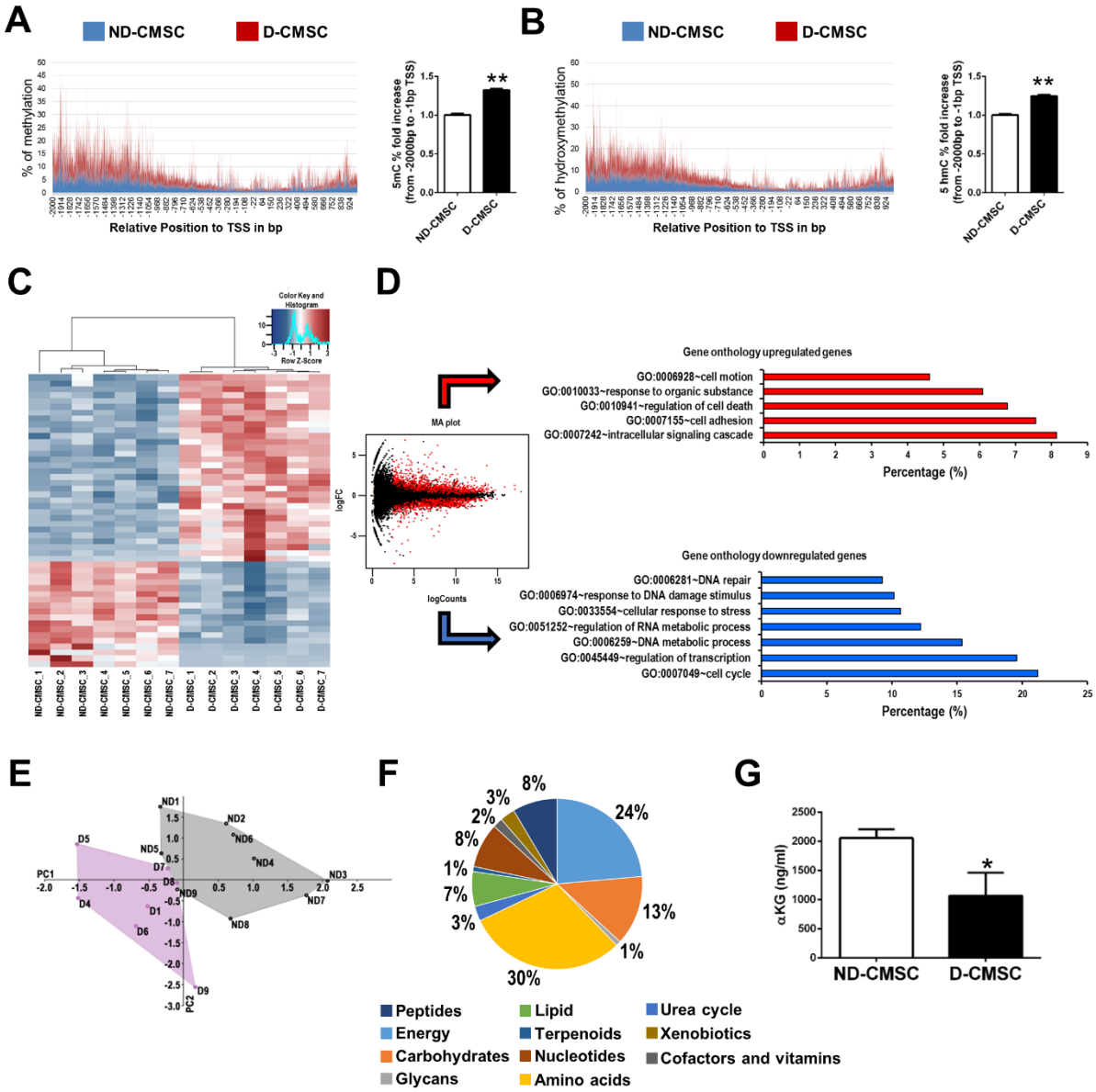

Figure 2

Integrative OMICS approach distinguished human cardiac mesenchymal cells according their origin. (A, B) Cis-regulatory Element Annotation System (CEAS) of 5mC **(A)** and 5hmC **(B)** distribution in annotated gene promoter regions of ND- (blue area) and D-CMSCs (red area). X-axis values: -2000bp to +1000bp from TSS. Right panels: relative 5mC and 5hmC enrichment in the same promoter regions. **(C)** Heatmap of 50 most differentially regulated genes in ND- and D-CMSCs by total RNA sequencing. Red and blue colors denote over- and under-represented genes, respectively. **(D)** Left panel: MA plot of regulated transcripts in ND- and D-CMSCs. Red dots: transcripts with fdr<0.05. Right panels: GO analysis. Upper panel, red bar graph: over-represented gene families; lower panel, blue bar graph: under-represented ones. **(E)** Principal component analysis of absolute metabolite levels. Gray colored convex hull: ND-donors; pink colored convex hull: D-donors. Axes are eigenvalue-scaled. **(F)** Pie chart illustrating GO analysis of annotated and down-modulated metabolites ($p<0.05$) obtained by iPath2 software. **(G)** Targeted metabolomic analysis of αKG intracellular level in ND- (white bar, n=4) and D-CMSCs (black bar, n=4). Error bars indicate SE. *$p<0.05$; **$p<0.01$. Data analyzed by Kolmogorov-Smirnov test.

Figure 3

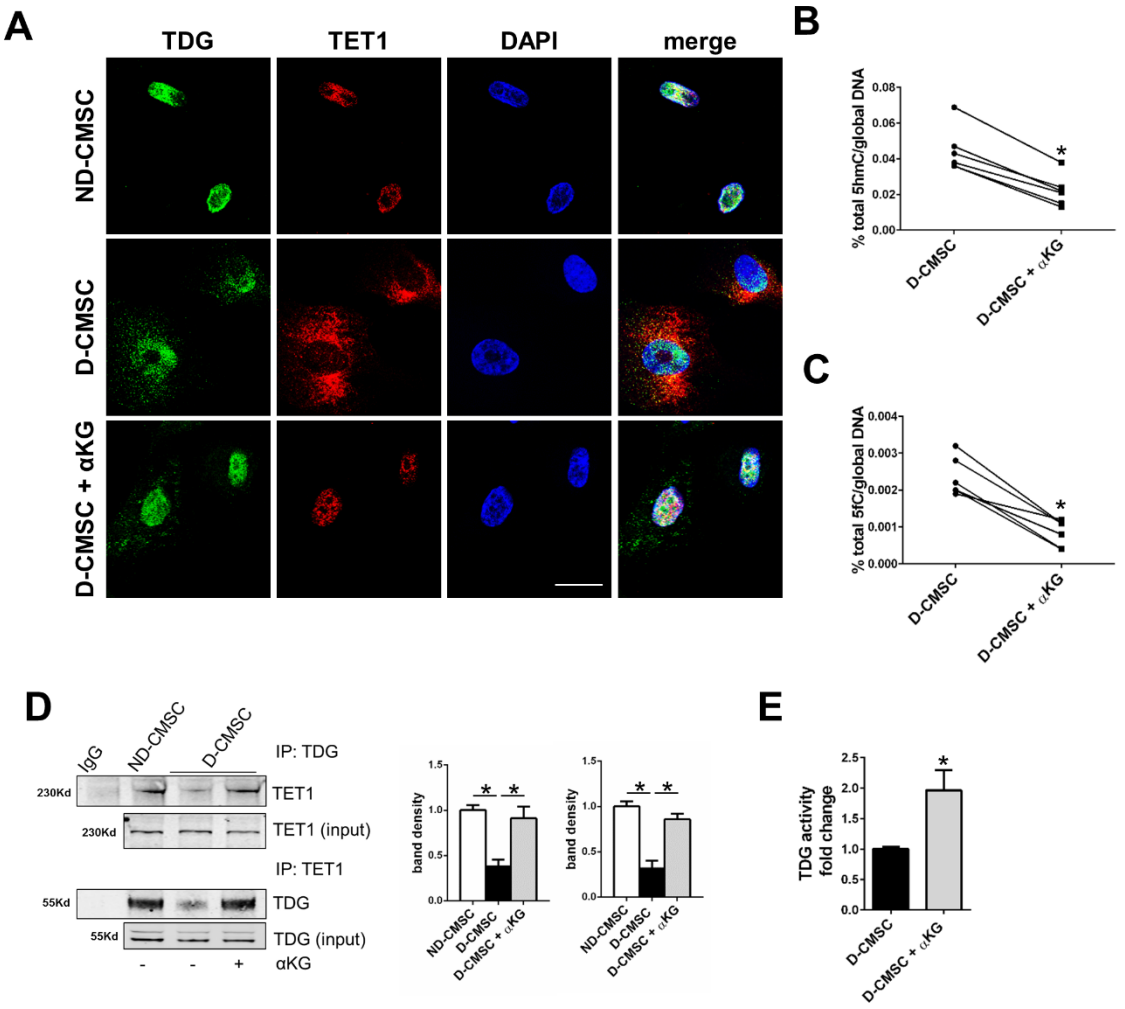

Figure 3

Alpha-ketoglutarate triggers TET1/TDG association, DNA demethylation and TDG activation. **(A)** Representative confocal microscopy images depicting ND-CMSCs and D-CMSCs±αKG. Cells probed by anti-TDG antibody (green; left panels) and anti-TET1 (red; middle left panels). Nuclei counterstained by DAPI (blue; middle right panels). Right panels: merged images. **(B-C)** Quantification of 5hmC **(B)** and 5fC **(C)** global levels in D-CMSCs±αKG. **(D)** Representative co-IP/WB analysis of TET1/TDG complex in ND-CMSCs, D-CMSCs±αKG. Right panels: densitometry of three independent experiments (TET1: left panel; TDG: right panel). **(E)** TDG activity of D-CMSCs (black bar), D-CMSCs+αKG (grey bar). Error bars indicate SE. n=6 per condition. *p<0.05. Data analyzed by Wilcoxon matched-pairs test **(B,C)** and Kolmogorov-Smirnov test **(D,E)**.

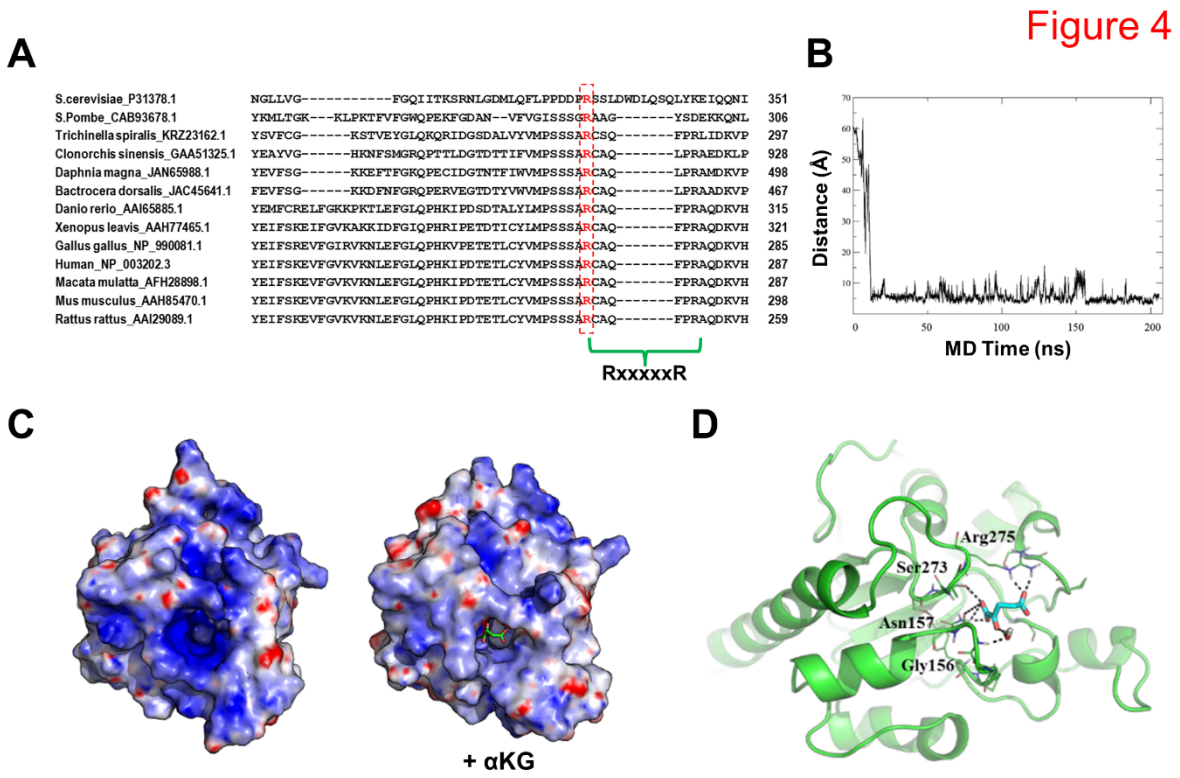

Figure 4

Alpha-ketoglutarate acts as an allosteric activator of TDG. (A) Multiple protein alignment showing arginine (R; red squared) at position 275 in human TDG protein highly interspecies conserved and predicted αKG RxxxxxR binding domain. **(B)** αKG binding to TDG investigated by MD simulations. Distance between the centroid of αKG two carboxyl groups and of Arg275 guanidine group plotted along MD simulation time. **(C)** TDG electrostatic surface potential retrieved from X-ray crystallography studies (left panel) and in complex with αKG as simulated by MD (right panel). TDG shown as surface. Positively charged regions: blue; negatively charged regions: red; neutral hydrophobic regions: white. Color intensity proportional to charge value. All surfaces calculated at the same salt concentration in aqueous medium. Same orientation of both protein structures. αKG: cyan sticks. **(D)** αKG/TDG interaction structural detail in the most populated cluster of conformations taken from MD trajectories. TDG: green cartoon, αKG: cyan sticks. Residues within 6Å from αKG mass center: lines. H-bond interactions: black dashed lines; TDG residues H-bonded to αKG are labeled.

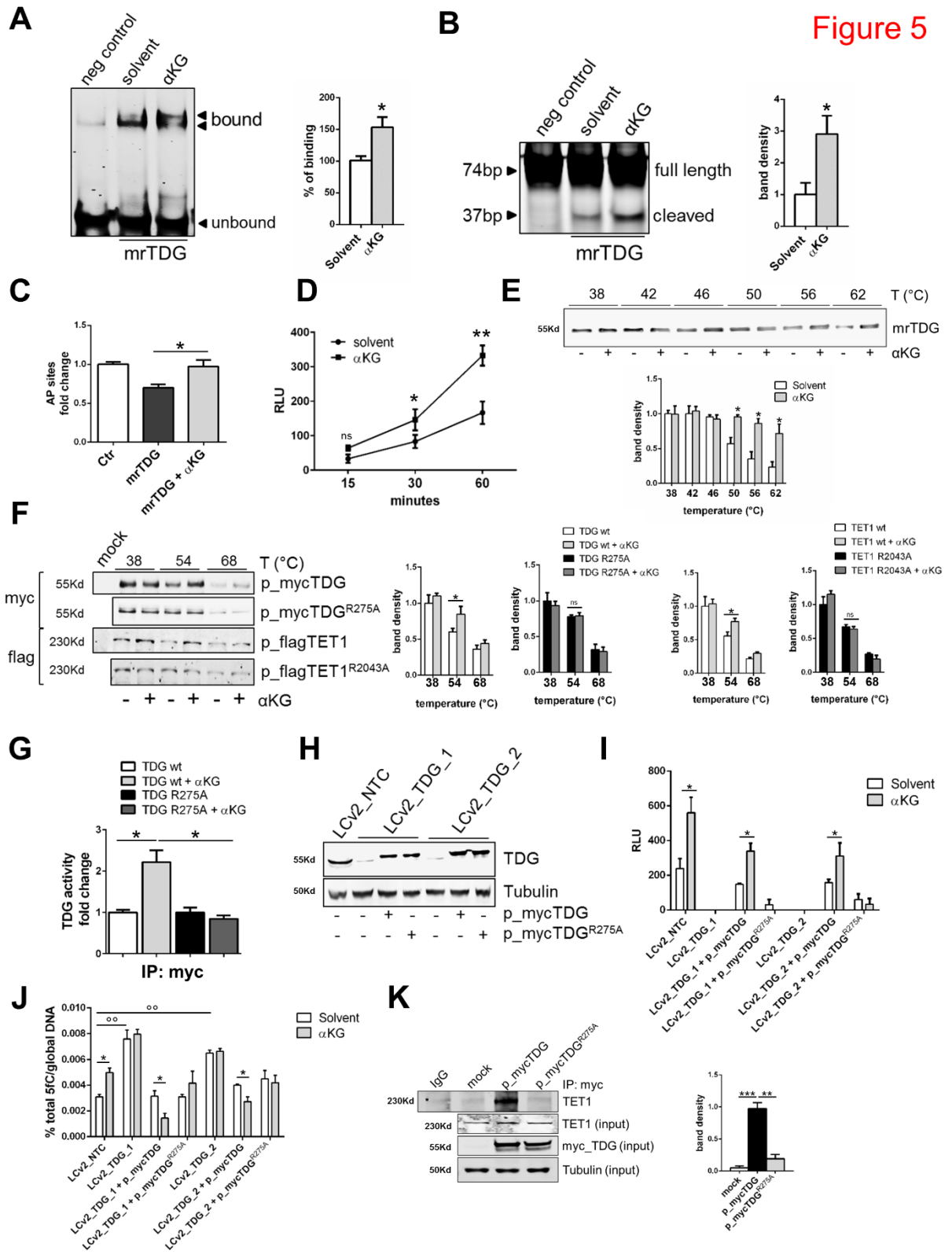

Figure 5

R275 is essential for αKG effect on TDG activity and stability. (A) EMSA determined by murine recombinant TDG protein (mrTDG)±αKG. The TDG/DNA binding detected by Top_G and Cy5.5_Bot_T primers in equimolar concentration. Signal visualized by Cy5.5 probe. Black arrows: protein-bound and unbound oligo. Right panel: TDG/DNA binding quantification in αKG absence (white bar) or presence (grey bar). Water used as solvent. n=5. **(B)** G/T glycosylase activity of

mrTDG±αKG by Top_G and Cy5.5_Bot_T primers in equimolar concentration. Signal detected by Cy5.5 probe. Right panel: densitometry of five independent experiments of TDG activity in αKG presence (grey bar). Water used as solvent (white bar). **(C)** Total AP site number on a reference DNA with mrTDG±αKG. Detection and quantification by ARP probe (n=4). **(D)** TDG activity assay of mrTDG in αKG presence (black squares). Water used as solvent (black circles). **(E)** TSA performed by mrTDG evaluated at 38, 42, 46, 50, 56 and 62°C±αKG. Right panel: densitometry of five independent experiments. **(F)** CETSA/WB analysis on myc-TDG, myc-TDG^{R275A}, flag-TET1 and flag-TET1^{R2043A}, after overexpression in HEK293T cells. Exogenous protein stability tested at 38, 54 and 68°C±αKG and detected by anti-myc and anti-flag antibodies. Lower panels: densitometry of three independent experiments. **(G)** TDGwt and TDG^{R275A} specific activity in response to αKG. Water used as solvent. Exogenous activity detected after transfection of myc-TDG and myc-TDG^{R275A} in HEK293T cells followed by IP with anti-myc antibody (n=4). **(H)** Representative WB of TDG levels in HEK293T cells after CRISPR/Cas9 inactivation (LCv2_TDG_1 and LCv2_TDG_2) compare to control vector (LCv2_NTC). TDG inactivated cells transfected by myc-TDG and myc-TDG^{R275A}. Signal from α-tubulin antibody used as loading control. **(I-J)** TDG activity assay **(I)** and 5fC quantification **(J)** performed in LCv2_NTC, LCv2_TDG_1 and LCv2_TDG_2 ± myc-TDG and myc-TDG^{R275A} ±αKG (gray bars). Water used as solvent (white bars). **(K)** Representative co-IP/WB analysis of TET1-mycTDG complex formation in HEK293T transfected with myc-TDG or myc-TDG^{R275A}. Right panel: TET1 densitometry of three independent experiments. Error bars indicate SE. *$p<0.05$; **$p<0.01$; ***$p<0.001$; °°$p<0.01$ vs LCv2_NTC. Data analyzed by Kolmogorov-Smirnov test **(A,B,C,E,F,G,I,J,K)** and 2way ANOVA **(D)**.

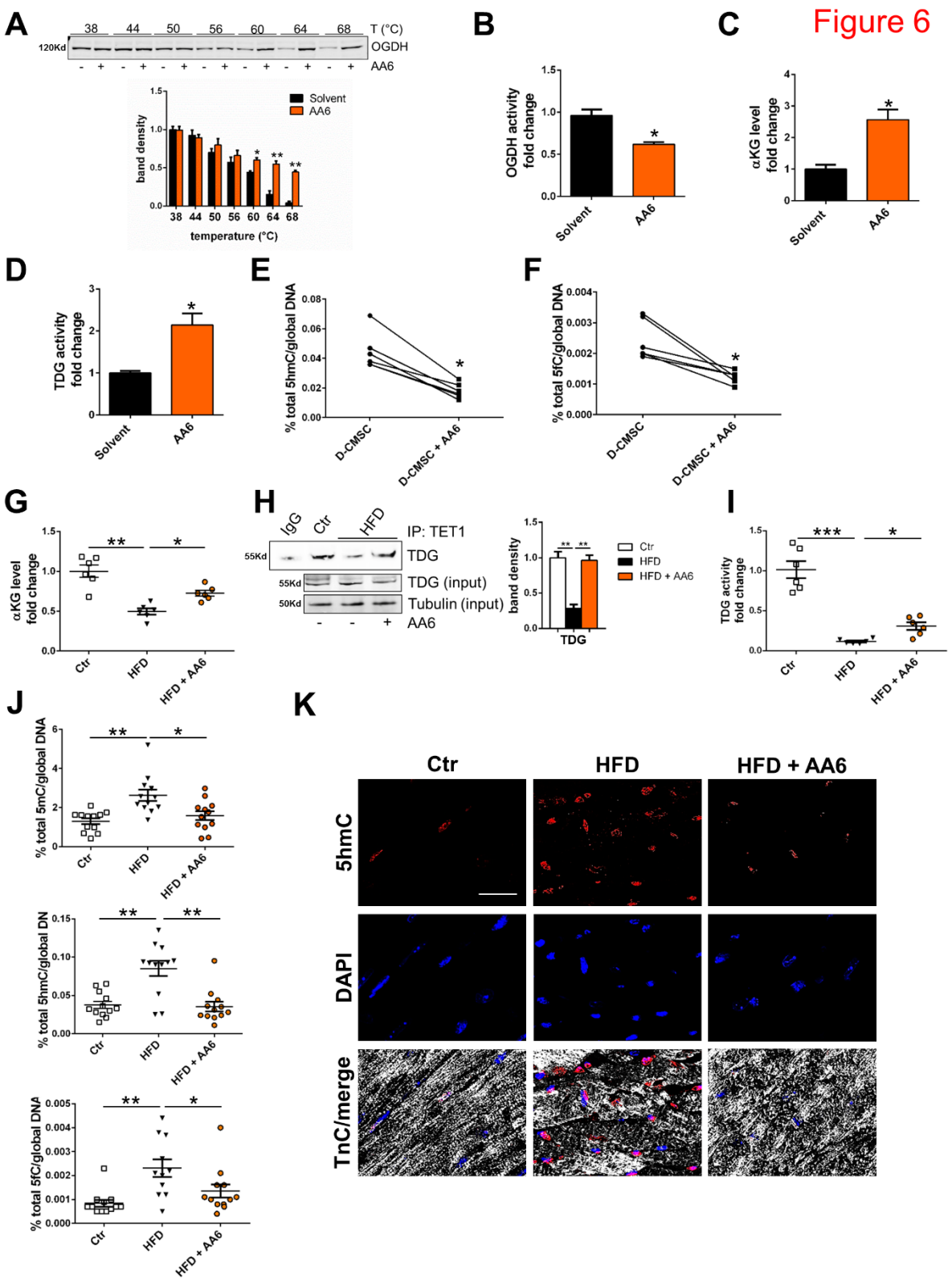

Figure 6

(S)-2-[(2,6-dichlorobenzoyl)amino]succinic acid (AA6) acts along the ODGH-αKG-TET/TDG pathway. (A) OGDH CETSA/WB analysis in D-CMSCs. Protein stability tested at 38, 44, 50, 56, 60, 64 and 68°C±AA6. Signals detected by anti-OGDH antibody. Lower panels: densitometry (n=3). **(B)** Intracellular OGDH activity in D-CMSCs treated with AA6 (orange bar). DMSO used as solvent (black bar), n=4. **(C)** αKG intracellular level quantification in D-CMSCs+AA6 (orange bar). DMSO used as solvent (black bar), n=4. **(D)** Intracellular TDG activity in D-CMSCs+AA6 (orange bar). DMSO used

as solvent (black bar), n=4. **(E, F)** Quantification of 5hmC **(E)** and 5fC **(F)** global levels in D-CMSCs±AA6. **(G)** αKG quantification in the whole heart of Ctr (1.00±0.08), HFD (0.49±0.04), and HFD+AA6 (0.72±0.04) treated mice (n=6). **(H)** Upper panel: representative co-IP/WB analysis of TET1/TDG complex in Ctr, HFD±AA6 fed mice. Lower panel: densitometry (Ctr. white bar; HFD: black bar; HFD+AA6: orange bar) n=3. **(I)** TDG activity in the whole hearts of Ctr (1.00±0.10), HFD (0.12±0.01) and HFD+AA6 (0.31±0.04) mice (n=6). **(J)** Quantification of 5mC (left panel; Ctr 1.30±0.15; HFD 2.62±0.29; HFD+AA6 1.58±0.22), 5hmC (middle panel; Ctr 0.037±0.004; HFD 0.085±0.010; HFD+AA6 0.035±0.006) and 5fC (right panel; Ctr 0.00084±0.00014; HFD 0.00230±0.00037; HFD+AA6 0.00130±0.00027) in whole heart of HFD (black triangles) and HFD+AA6 (orange circles) fed mice compared to control (white squares) (n=12). **(K)** Representative confocal microscopy images depicting Ctr, HFD and HFD+AA6 heart. Cardiac tissue probed by anti-5hmC (red) and anti-Troponin C (TnC, white) antibody. Nuclei counterstained by DAPI (blue). Scale bar 20µm. Error bars indicate SE. *$p<0.05$; **$p<0.01$. ***$p<0.001$. Data analyzed by Kolmogorov-Smirnov test **(A,B,C,D,G,H,I,J)** and Wilcoxon matched-pairs test **(E,F)**.

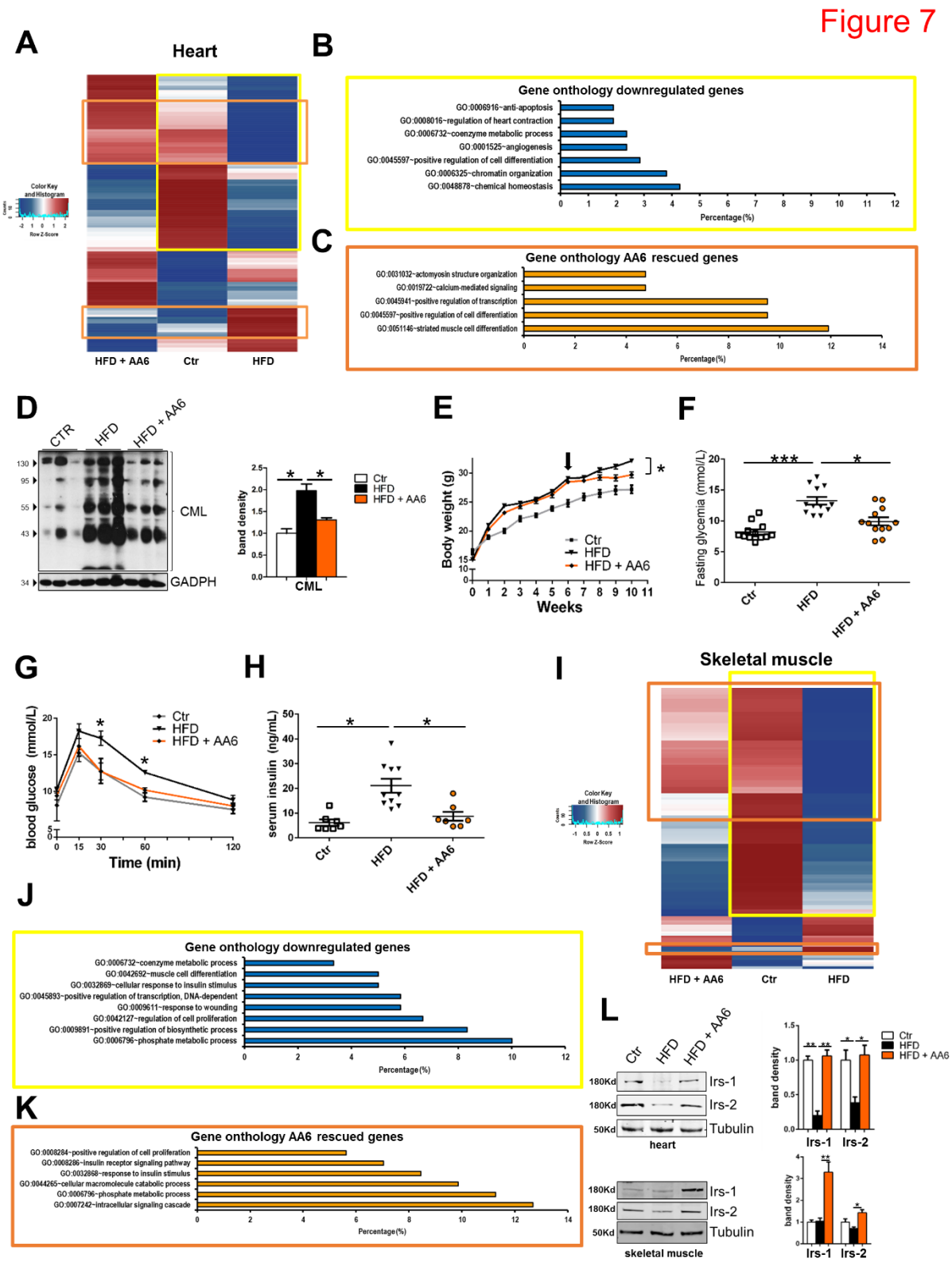

Figure 7

AA6 rescues insulin response in HFD mice. (A) Heatmap showing the 50 most differentially regulated genes in the heart of Ctr, HFD and HFD+AA6 mice by total RNA sequencing. Red and blue represent over- and under-expressed genes, respectively. Yellow square: genes differentially regulated in HFD animals (n=4). Orange squares: gene expression rescued by HFD+AA6 (n=4). **(B)** GO analysis of HFD-differentially regulated genes in the heart of Ctr and HFD fed mice (blue bar graph). **(C)** GO analysis of AA6-rescued transcripts between HFD fed mice and those treated with AA6 (orange bar graph). **(D)**

Representative WB analysis of three independent whole heart tissue lysates from Ctr, HFD±AA6 probed with CML-antibody. GADPH used as loading control. Right panel: densitometry. **(E)** Animal body weight during standard diet (Ctr) and HFD feeding. Black arrow indicates AA6 starting treatment after 6 weeks. Numeric data provided as online. **(F)** Blood glucose quantification in Ctr (white squares, n=12; 8.19±0.39), HFD (black triangles, n=12; 13.25±0.63) and HFD+AA6 (orange circles, n=12; 9.91±0.64) mice. **(G)** Oral glucose tolerance test (OGTT) in Ctr, HFD and HFD+AA6 mice. Numeric data provided as online. **(H)** Serum insulin level of mice fed with standard diet (Ctr, white squares, n=7; 6.19±1.28), HFD (black triangles, n=10; 21.06±2.82) or HFD+AA6 (orange circles, n=7; 8.67±1.81). **(I)** Heatmap showing the 50 most differentially regulated genes in tibialis muscle of Ctr, HFD and HFD+AA6 by total RNA sequencing. Red and blue represent over- and under-expressed genes respectively. Yellow square: differentially regulated genes in HFD (n=3). Orange squares: genes rescued by HFD+AA6 (n=3). **(J)** GO analysis of HFD-differentially regulated genes in tibialis muscle of Ctr and HFD (blue bar graph). **(K)** GO analysis of AA6-rescued transcripts in tibialis muscle between HFD fed mice and HFD+AA6 (orange bar graph). **(L)** Representative WB analysis of three independent tissue extracts from heart (upper panel) and tibialis muscle (lower panel) of Ctr, HFD and HFD+AA6 mice probed with Irs1 and Irs2 antibodies. α-tubulin was used as loading control. Right panels: densitometry. Error bars indicate SE. *$p<0.05$; **$p<0.01$; ***$p<0.001$. Data analyzed by Kolmogorov-Smirnov test **(D**,**L)**, 1way ANOVA with Bonferroni post-hoc test **(F,H)** and 2way ANOVA **(E,G)**.

Stable oxidative cytosine modifications accumulate in cardiac mesenchymal cells from Type2 diabetes patients: rescue by alpha-ketoglutarate and TET-TDG functional reactivation.

Francesco Spallotta[1#], Chiara Cencioni[1#], Sandra Atlante[1], Davide Garella[2], Mattia Cocco[2], Mattia Mori[3], Raffaella Mastrocola[4], Carsten Kuenne[5], Stefan Guenther[5], Simona Nanni[6], Valerio Azzimato[7], Sven Zukunft[8], Angela Kornberger[9], Duran Sürün[10], Frank Schnütgen[10], Harald von Melchner[10], Antonella Di Stilo[2], Manuela Aragno[4], Maarten Braspenning[11], Wim van Criekinge[12], Miles De Blasio[13], Rebecca H. Ritchie[13], Germana Zaccagnini[14], Fabio Martelli[14], Antonella Farsetti[15,18], Ingrid Fleming[8], Thomas Braun[16], Andres Beiras-Fernandez[9], Bruno Botta[17], Massimo Collino[2], Massimo Bertinaria[2], Andreas M. Zeiher[18], Carlo Gaetano[1*]

1 Division of Cardiovascular Epigenetics, Department of Cardiology, Goethe University, Frankfurt am Main 60596, Germany. E-Mails: fspallotta@gmail.com (FS); chcencioni@gmail.com (CC); sandra.atlas@yahoo.it (SA).
2 Dipartimento di Scienza e Tecnologia del Farmaco, Università degli Studi di Torino 10125, Torino, Italy. E-Mails: davide.garella@unito.it (DG), mattia.cocco@unito.it (MC), antonella.distilo@unito.it (AS); massimo.collino@unito.it (MCo); massimo.bertinaria@unito.it (MB)
3 Center for Life Nano Science@Sapienza, Istituto Italiano di Tecnologia, viale Regina Elena 291, 00161 Rome, Italy. E-Mail: m.mattia79@gmail.com (MM)
4 Dipartimento di Scienze Cliniche e Biologiche, Università degli Studi di Torino 10125, Torino, Italy. E-Mails: raffaella.mastrocola@unito.it (RM); manuela.aragno@unito.it (MA)
5 Bioinformatics Group, Max Planck Institute for Heart and Lung Research, Bad Nauheim 61231, Germany. E-Mails: carsten.kuenne@mpi-bn.mpg.de (CK); Stefan.Guenther@mpi-bn.mpg.de (SG)
6 Istituto di Patologia Medica, Università Cattolica del Sacro Cuore, Rome, Italy. E-Mail: simona.nanni@yahoo.it (SN)
7 Integrated Cardio Metabolic Centre, Department of Medicine, Karolinska Institutet. 141 57 Huddinge, Sweden. E-Mail: valerio.azzimato@gmail.com (VA)
8 Institute for Vascular Signaling, Goethe-University, Frankfurt am Main, Germany. E-Mails: zukunft@vrc.uni-frankfurt.de (SV); fleming@vrc.uni-frankfurt.de (IG)
9 Department of Cardiovascular Surgery, University of Mainz, Mainz, Germany. E-Mails: Angela.Kornberger@unimedizin-mainz.de (AK); Andres.Beiras@uni-mainz.de (AB)
10 LOEWE Center for Cell and Gene Therapy and Department of Medicine, Hematology/Oncology, Goethe University, Frankfurt 60596, Germany. E-Mails: d.sueruen@med.uni-frankfurt.de (DS); schnuetgen@em.uni-frankfurt.de (FSc.); melchner@em.uni-frankfurt.de (HM)
11 NXT-Dx, Ghent, Belgium. E-Mails: maarten.braspenning@nxt-dx.com (MBr)
12 Department of Mathematical Modelling, Statistics and Bioinformatics, Ghent University, Ghent, Belgium. E-Mails: Wim.VanCriekinge@UGent.be (WvC)
13 Laboratory of Heart Failure Pharmacology, Baker IDI Heart and Diabetes Institute, Melbourne VIC 3004, Australia. E-Mails: Miles.DeBlasio@baker.edu.au (MDB); Rebecca.Ritchie@baker.edu.au (RR)

14 Molecular Cardiology Laboratory, IRCCS-Policlinico San Donato, San Donato Milanese, Milan 20097, Italy. E-Mail: Germana.Zaccagnini@grupposandonato.it (GZ); fabio.martelli@grupposandonato.it (FM)
15 National Research Council, Institute of Cell Biology and Neurobiology (IBCN), Rome, Italy. E-Mail: antonella.farsetti@cnr.it (AF)
16 Department of Cardiac Development and Remodeling, Max-Planck-Institute for Heart and Lung Research, Bad Nauheim 61231, Germany. E-Mail: thomas.braun@mpi-bn.mpg.de (TB)
17 Dipartimento di Chimica e Tecnologie del Farmaco, Sapienza University of Rome, 00185 Rome, Italy. E-Mail: bruno.botta@uniroma1.it (BB)
18 Internal Medicine Clinic III, Department of Cardiology, Goethe University, Frankfurt am Main 60596, Germany. E-Mail: zeiher@em.uni-frankfurt.de (AZ)

# Dr. Spallotta and Cencioni contributed equally to this work

*Current address: Laboratorio di Epigenetica, Istituti Clinici Scientifici Maugeri, Via Maugeri 4, Pavia, Italy.

Corresponding authors:
Prof. Carlo Gaetano MD, FAHA.
Division of Cardiovascular Epigenetics, Department of Cardiology, Goethe University, Frankfurt am Main 60590, Germany
E-Mail: gaetano@em.uni-frankfurt.de; Tel.: +49-69-6301-87963; Fax: +49-69-6301-86095.

Dr. Francesco Spallotta, PhD
Division of Cardiovascular Epigenetics, Department of Cardiology, Goethe University, Frankfurt am Main 60590, Germany
E-Mail: fspallotta@gmail.com; Tel.: +49-69-6301-87957; Fax: +49-69-6301-86095.

Running title: Metabolism & DNA methylation.
Keywords: DNA methylation, TET, TDG, α-ketoglutarate, hyperglycemia, diabetes, heart, cardiac fibroblasts.
Subject codes: Metabolism, Epigenetics, Type 2 Diabetes

SUPPLEMENTAL METHODS

Animals and treatments. Insulin resistance was induced by high fat diet (HFD) in 4 weeks old male C57Bl/6j mice (Charles River Laboratories, Calco, Italy) cared in compliance with the European Council directives (No. 86/609/EEC) and with the NIH Guide for the care and use of laboratory animals (eighth edition, 2011). Treatment was approved by the Ethical Committee of the Turin University (permit number: D.M. 94/2012-B). In brief, mice were fed a standard diet (control group, n = 8) or a 60% fat diet (HFD group, n = 16) for ten weeks. Standard diet (Ssniff, Soest, Germany, R/M Control) composition was: 70% of calories in carbohydrates, 10% of calories in fat, and 20% of calories from proteins. High-fat diet (Ssniff, D12331 Surwit) composition was: 26% of calories in carbohydrates, 59% of calories in fat (hydrogenated coconut oil), and 15% of calories from proteins. All groups received drink and food *ad libitum*. After 6 weeks of diet a subgroup of mice taken from HFD group (n = 8, each) started AA6 administration (25 mg/kg dissolved in water) by daily i.p. injection. Hyperglycemia was induced in male CD1 mice (Charles River, UK) by streptozotocin injection (STZ (Sigma); 40 mg/kg i.p. per day for 5 days). Age-matched, non-diabetic control animals, received STZ-vehicle alone according to prior published protocols.[1] Hyperglycemia was confirmed measuring glucose levels in blood periodically. All these experimental procedures were conducted according European Community guidelines (Council Directive 2010/63/EU) and were approved by Italian National Institute of Health (DGSAF0005330 n° 202/2016-PR) and Institutional Animal Care of the Università Cattolica (100/2003-A). Early-stage type 2 diabetes was induced in 6 week old male FVB/N mice by using a combination of low dose streptozotocin (STZ, Sigma) followed by a HFD (42% energy intake from lipids, SF04-001, Specialty Feeds Western Australia). Mice received STZ (55 mg/kg i.p per-day) for 3 days and were then placed on a HFD until end-point. Sham non-diabetic mice are administered with the equivalent volume of a citric acid vehicle solution (3 injections over 3 days) and are fed the normal chow diet. After 20 weeks of HFD (or chow for controls) mice are killed and tissues collected for later analysis. This mouse model has been shown to mimic type 2 diabetes, resulting in a phenotype similar to that seen in humans in terms of both insulin resistance and glucose intolerance. In all experiments animals were barcoded and randomly assigned to the experimental groups so the observer was blind to the identity of the samples. All experiments were performed and annotated in compliance with the ARRIVE guidelines.[2]

HFD monitoring and blood analyses. Body weight and food intake were recorded weekly. Where required, fasting glycaemia was measured at start and every 4 weeks by using a standard glucometer (GlucoGmeter, Menarini Diagnostics) after saphenous vein puncture. After 10 weeks, mice were

anesthetized and killed by cardiac exsanguination. Blood was collected, the heart removed and snap frozen in liquid nitrogen. The plasmatic level of insulin was determined by ELISA (Mercodia AB, Uppsala, Sweden). The oral glucose tolerance test (OGTT), was performed after a fasting period of 6 h by administering glucose (2 g/kg) by oral gavage. Blood samples were obtained before glucose administration and at 15, 30, 60 and 120 minutes afterwards by saphenous vein puncture. Glucose concentration was measured by a glucometer as stated above.

Patients. The current study enrolled 50 patients (see Online Table I) undergoing CABG or VAO. Clinical information was collected for each patient and included age, sex, diabetes, surgical and medical treatments. All data were collected and analyzed anonymously. All patients were enrolled after ethical committee approval and informed consent according to standard hospital procedures. Investigations were conducted according to the principles expressed in the Declaration of Helsinki.

Cell isolation, culture, treatment and transfection. Primary human cardiac mesenchymal cells (CMSCs) were obtained from the auricles of non-diabetic (ND) and diabetic (D) donors. Cells were isolated and cultured as previously described[3]. During the progress of this work and in consequence of their different growth rate, not all primary cell isolates could always be utilized. Consequently, not all the experiments were performed with the same isolates. Before cryopreservation, all D- and ND-isolates were characterized according to previously published criteria[3], barcoded, frozen and, when necessary, randomly chosen among those available between the two groups. However, all 50 strains were assayed for proliferation. On average 5-10 independent randomly chosen cellular strains from each group, were used in all the experiments. To avoid senescence, cells were passaged no more than 4-8 times before assay. When required, CMSCs were exposed to the following compound: cell permeable Octyl-α-ketoglutarate, 20 μM (Cayman Chemical), Oxalomalic Acid, 1 mM (Cayman Chemical), AA6, 10 μM, Okadaic Acid, 10 nM (Cayman Chemical). Patient peripheral blood mononuclear cells (PBMCs) and plasma were isolated using Ficoll-Paque Plus (GE Healthcare) reagent according manufacturer instructions. For the high glucose culture experiments human umbilical vein endothelial cells (HUVEC) were maintained in EGM medium (Lonza) and exposed to 25 mM glucose (B-Braun) or an equivalent amount of mannitol (Serag Wiessner). Embryonic cardiac H9C2 cells (RRID:CVCL_0286), derived from the ventricular part of an E13 BDIX female rat heart (Sigma), were cultured and differentiated as previously described.[4] Briefly, H9C2 cells were cultured in Dulbecco's modified Eagle's medium (DMEM) supplemented with 1% donor calf serum (DCS - Sigma), 1% Pen-Strep (Sigma) and 1% Glutamine (Gibco) to induce cardiac differentiation. For gene expression experiments, HEK293T cells were maintained in DMEM (Sigma) supplemented with 10%

FBS (Millipore), 1% Pen-Strep (Sigma) and 1% Glutamine (Gibco). HEK293T cells were transfected with 200 ng/1 µg of each relevant plasmid including hTDG-(Myc-DDK-tagged (Origene), $hTDG^{R275A}$-(Myc-DDK-tagged), FH-TET1-pEF-(Flag- HA-tagged) (Addgene), $FH\text{-}TET1^{R2043A}$-pEF-(Flag-HA-tagged) according to Lipofectamine3000 standard protocol (Invitrogen). FH-TET1-pEF was kindly gifted by Anjana Rao (Addgene plasmid # 49792).[5]

Cytosine quantification. Global levels of 5mC, 5hmC, 5fC were measured by the MethylFlash Methylated DNA Quantification Kit (Epigentek), MethylFlash Hydroxymethylated DNA Quantification Kit (Epigentek) and MethylFlash 5-Formylcytosine DNA Quantification Kit (Epigentek) respectively. Briefly, from all sources genomic DNA was extracted using the E.Z.N.A. Tissue DNA kit (Omega biotek) according to manufacturer's instructions. 100-300-500 ng of total genomic DNA was used for quantification of 5-mC, 5hmC and 5fC respectively in agreement with the standard manufacturer's protocol. Optical density (OD) values were obtained by a multi-well plate reader (EnSpire® Multimode Plate Reader – Perkin Elmer) set at 450 nm. 5hmC and 5fC were further analyzed by in-cell western (ICW). Briefly, ND/D-CMSCs were plated at 70% confluence overnight in 96 multi-well-plates. Cells were fixed in 4% paraformaldehyde for 10 min at room temperature (RT), then permeabilized with HCl 1 M 1 h at 37°C. After permeabilization cells were neutralized and washed with TRIS HCl 0,1 M pH 7.4 and 0.1% Triton X-100 30 min, RT, shaking. Cells were blocked with 3% BSA and then incubated with primary antibody (anti-5hmC 1:500, Rabbit polyclonal, Active Motif; anti-5fC 1:500, Rabbit polyclonal, Active Motif). Anti-rabbit polyclonal immunoglobulins labelled with the infrared-sensitive dye, IRDyes 700/800 (Odyssey, LI-COR), were used as secondary antibody. Signal were normalized for total DNA content by DRAQ5 (1:1000, Biostatus) counterstaining. Detection was performed by Odyssey CLx Infrared Imaging System (LI-COR Biosciences). Plates were imaged with the IR imager at both 700 and 800 nm channels in a single scan.

Genomic DNA sequencing. Genomic DNA (gDNA) was extracted from 8 independent CMSC lines (4 ND- and 4 D-) by E.Z.N.A. tissue DNA kit (Omega biotek) and sent to NXT-Dx (Fr. Rooseveltlaan 349/B.43 9000 Gent – Belgium) for methylation and hydroxymethylation detection by reduced representation bisulfite (RRBS) and oxidative RRBS (oxRRBS) sequencing respectively. In brief, gDNA concentration was measured by Quant-it Picogreen dsDNA assay. After digestion and bisulfite (BS) treatment, quality control was performed on Agilent 2100 HS DNA chip. 1 µg input of gDNA was used in the MSP1 digest. Following overnight incubation at 37°C, digestion reactions were terminated by adding 0.5 M EDTA and purified on a Gene-JET PCR purification column. Libraries

were prepped using the NEBNext Ultra DNA library preparation kit from Illumina and methylated adapters (Index primers Set 1). Adapter-ligated fragments were BS converted. TrueMethyl Seq kit (CEGX, Cambridge Epigenetics) was used for denaturation, oxidation (only for OX Workflow), BS conversion and cleanup. 14 cycles of PCR were performed and the products were purified using AMPure XP beads. Quality of the final libraries was determined hybridization on a high sensitivity DNA chip (Agilent) and concentration was measured with qPCR. Sequencing was done on an Illumina HiSeq2500 PE 2x50bp. The FASTQ sequence reads were generated using the Illumina Casava pipeline. Initial quality assessment was based on data passing the Illumina Chastity filter. The second quality assessment was based on the reads using the FASTQC quality control tool version 0.10.0. The paired end 50bp sequences reads are mapped using the Bismark package v0.10.1 by using the following parameters: q (fastq file); X 1000 (max length between paired ends); non_directional (non-directional protocol); bowtie2. A coverage cutoff of 5 was adopted for reporting a CpG in a sample. These human samples were mapped on the human reference genome build hg19. Gene annotation was done with the Ensembl Homo sapiens v66 (Online Table II). CEAS (Cis-regulatory Element Annotation System) visualization at promoter regions of annotated genes from the human refseq database downloaded from UCSC (2016-03-15). An average methylation/hydroxymethylation percentage was calculated for every position in promoter region (-2000 to +1000 around TSS) within the ND and D groups. The X-axis represents the relative position to the TSS. Gene ontology on promoters exclusively regulated by diabetes (±10% methylation difference, fdr<0.05) was performed using DAVID (https://david.ncifcrf.gov/).

Detection of 5mC and 5hmC in human mitochondrial DNA (mtDNA). The enrichment of 5mC and 5hmC in specific loci (CCpGG) of the human mitochondrial DNA (mtDNA) was analyzed by Epimark® 5mC and 5hmC Analysis Kit (New England Biolabs) according to manufacturer's instruction. Briefly, mtDNA was isolated with Mitochondrial DNA Isolation kit (Biovision). The analysis was performed in unique loci of mitochondrial genes excluding those belonging to tRNAs or exclusively present in gDNA. The following primers were used:

h_mt12S_1 (chrM:870+966) Fw	CCCAGGGTTGGTCAATTTC
h_mt12S_1 (chrM:870+966) Rev	GGGAGGGGGTGATCTAAAAC
h_mtND2_3 (chrM:5199+5326) Fw	AATTCCATCCACCCTCCTCT
h_mtND2_3 (chrM:5199+5326) Rev	TGATGGTGGCTATGATGGTG
h_mtCOX1_1 (chrM:6235+6351) Fw	CTCCTGCTCGCATCTGCTAT
h_mtCOX1_1 (chrM:6235+6351) Rev	GGAGAAGATGGTTAGGTCTACGG

h_mtCOX1_5 (chrM:7119+7240) Fw	AGACCAAACCTACGCCAAAA
h_mtCOX1_5 (chrM:7119+7240) Rev	CATCGGGGTAGTCCGAGTAA
h_mtCOX3_1 (chrM:9212+9336) Fw	CCCACCAATCACATGCCTAT
h_mtCOX3_1 (chrM:9212+9336) Rev	GAGGAGCGTTATGGAGTGGA
h_mtND1 (chrM:3486+3554) Fw	CCCTAAAACCCGCCACATCT
h_mtND1 (chrM:3486+3554) Rev	GAGCGATGGTGAGAGCTAAGGT
h_mtND4_2 (chrM:12077+12199) Fw	ACACCTATCCCCCATTCTCC
h_mtND4_2 (chrM:12077+12199) Rev	AGGGGTCGTAAGCCTCTGTT
h_mtND5_1 (chrM:13277+13399) Fw	CCAACCACACCTAGCATTCC
h_mtND5_1 (chrM:13277+13399) Rev	TTGTTCATTGTTAAGGTTGTGGA
h_mtND5_2 (chrM:13594+13761) Fw	AAGCGCCTATAGCACTCGAA
h_mtND5_2 (chrM:13594+13761) Rev	GCGGGGGAAATGTTGTTAGT
h_mtD-loop_1 (chrM:23+151) Fw	CCATGCATTTGGTATTTTCG
h_mtD-loop_1 (chrM:23+151) Rev	GGATGAGGCAGGAATCAAAG

5mC and 5hmC enrichment was normalized to total mtDNA detected by ND1.

Detection of 5mC/5hmC on Irs-1 and Irs-2

Irs-1 and Irs-2 methylation/hydroxymethylation have been analyzed by Epimark® 5mC and 5hmC Analysis Kit (New England Biolabs) according to manufacturer's instruction. The amplified region was selected according to the sequencing data and the number of CCpGG sites was checked on MethPrimer 2. The following primers were used:

h_Irs-1_met Fw	GCGATCTAGTGCTTCGGTGT
h_Irs-1_met Rv	TTGCTTAGCTCCTCCTCACC
h_Irs-2_met Fw	AAGTCAATGCTGGCGTAGGT
h_Irs-2_met Rv	GCTTCCAGAATGGTCTCAACTA

mRNA extraction and qRT-PCR. RNA was extracted from CMSC (approximately $3x10^6$) or 10 mg of tissue using Tri-Reagent (Sigma) according to manufacturer's instruction. cDNA synthesis for quantitative real-time PCR (qRT-PCR) was carried out with SuperScript III First-Strand Synthesis Super Mix for qRT-PCR (Invitrogen) according to the manufacturer's protocol. All reactions were performed in 96-well format in the StepOne Plus Real-Time PCR System (Applied Biosystems) using ORA^{TM} qPCR Green ROX H Mix (HighQu). For each gene of interest, qRT-PCR was performed as

follows: each RNA sample was tested in duplicate and p0 (human and mouse) or beta Actin (rat) were used to normalize transcript abundance. mRNA expression levels were calculated by Comparative Ct Method by using the Applied Biosystem software (Applied Biosystem, CA, USA) and were presented as fold induction of transcripts for target genes. The following primers were used:

h_Irs-1 Fw	CAGAGGACCGTCAGTAGCTC
h_Irs-1 Rev	TTCTCTCATGACACGGTGGTG
h_Irs-2 Fw	ACACCTACGCCAGCATTGAC
h_Irs-2 Rev	GCCTTGTTGGTGCCTCATCT
h_p0 Fw	TCGACAATGGCAGCATCTAC
h_p0 Rev	ATCCGTCTCCACAGACAAGG
m_Nppa Fw	ACAGCTTCCGGTACCGAAGA
m_Nppa Rev	CACACCACAAGGGCTTAGGA
m_Nppb Fw	CACTCCTATCCTCTGGGAAGTCCTA
m_Nppb Rev	CTCCAGCAGCTTCTGCATCTT
m_MnSOD Fw	GTTGGCCAAGGGAGATGTTA
m_MnSOD Rev	CTGATTTGGACAAGCAGCAA
m_ACTA Fw	CCATCGGCAATGAGCGTTTC
m_ACTA Rev	CCTGATGTCGATGTCGCACT
m_ATP2a2 Fw	ACAACCAAGGGTCTCCA
m_ATP2a2 Rev	CAATGACCCAGTTCATGGTG
m_Myh6 Fw	CTCATGCGCATTGAGTTCAAG
m_Myh6 Rev	CGAATGTTCCACTGGATAACCA
m_Myh7 Fw	TCTGCTGAAGGACACTCAAATCC
m_Myh7 Rev	GTTCTCTTTCAGGTCGTCATTGG
m_Ki67 Fw	AATCCAACTCAAGTAAACGGGG
m_Ki67 Rv	TTGGCTTGCTTCCATCCTCA
m_p0 Fw	GCGTCCTGGCATTGTCTGT
m_p0 Rev	GAAGGCCTTGACCTTTTCAGTAAG
r_Adra2 Fw	CTGGCCTCAGCGGACATC
r_Adra2 Rv	GTTGGCCAAAGAAAAGGGAAT
r_Mlc2 Fw	CCTCAGACACCATGTCACCAAA
r_Mlc2 Rv	GGATCTGGGTCTGCTCAAACA
r_Nexn Fw	AAGACATGCTCGCTTCTGATGA

r_Nexn Rv	CCCTGTGAGCTTTGGGACAT
r_betaActin Fw	ACCAGTTCGCCATGGATGAC
r_betaActin Rv	TGCCGGAGCCGTTGTC

Total RNA extraction, sequencing and bioinformatics analysis. For next generation sequencing (NGS) RNA was isolated from 14 independent human cell lines (7 ND- and 7-D-), mice skeletal muscle (3 wt, 3 HFD and 3 HFD + AA6) and heart samples (4 wt, 4 HFD and 4 HFD + AA6) using the miRNeasy micro Kit (Qiagen) combined with on-column DNase digestion (DNase-Free DNase Set, Qiagen) to avoid contamination by genomic DNA. RNA and libraries integrity were verified with a BioAnalyzer 2100 (Agilent) or LabChip Gx Touch 24 (Perkin Elmer). 1 µg of total RNA was used as input for SMARTer Stranded Total RNA Sample Prep Kit - HI Mammalian (Clontech). Sequencing was performed on the NextSeq500 instrument (Illumina) using v2 chemistry, resulting in minimum of 20M reads per library with 2x75bp paired end setup. For RNA sequencing (RNA-Seq) of muscles from diabetic mice, 1 µg total RNA was used as input for Truseq Stranded mRNA Library preparation following the low sample protocol (Illumina). The resulting raw reads were assessed for quality, adapter content and duplication rates with FastQC (Available online at http://www.bioinformatics.babraham.ac.uk/projects/fastqc). Trimmomatic version 0.33 was employed to trim reads after a quality drop below a mean of Q20 in a window of 4 nucleotides.[6] Only reads above 20 nucleotides were cleared for further analyses. Trimmed and filtered reads were aligned versus the Ensembl genome version hg19 (GRCh37) for human and mm10 (GRCm38) for mouse samples using STAR 2.4.2a with the parameter “outFilterMismatchNoverLmax 0.1” to increase the maximum ratio of mismatches to mapped length to 10%.[7] The number of reads aligning to genes was counted with featureCounts 1.4.5-p1 tool from the Subread package.[8] Only reads mapping at least partially inside exons were admitted and aggregated per gene (see Online Table III, VI and VII). Reads overlapping multiple genes or aligning to multiple regions were excluded. Differentially expressed genes were identified using DESeq2 version 1.62.25. Only genes with a minimum fold change of ± 2, a maximum Benjamini-Hochberg corrected p-value of 0.05, and a minimum combined mean of 5 reads were deemed to be significantly differentially expressed. The Ensembl annotation was enriched with UniProt data (release 06.06.2014) based on Ensembl gene identifiers (Activities at the Universal Protein Resource (UniProt)).

The correlation of replicate gene counts was assessed with the Spearman ranked correlation algorithm included in R 3.11 (R: A language and environment for statistical computing). After pairwise comparison of high 5mC/high 5hmC, the overlapping extent of differentially

methylated/hydroxymethylated promoters between ND-CMSC and D-CMSC was analyzed by Venn diagrams (Venny 2.1.0 http://bioinfogp.cnb.csic.es/tools/venny/). Gene ontology and KEGG Pathways analysis on genes exclusively regulated by diabetes (± 0.5 log2 fold change, basemean > 5, fdr < 0.05) was performed using DAVID (https://david.ncifcrf.gov/), which allows to determine statistically overrepresented GO and KEGG categories in the derived biological networks.

Metabolites quantification. Untargeted metabolomics analysis was performed by Metabolomics Discoveries (Metabolomic Discoveries GmbH, Potsdam-Golm, Germany). Briefly, material from 18 independent CMSC strains (9 ND- and 9 D-) was collected for metabolite extraction (Online Table IV). Cells were disrupted by three freeze-thaw cycles, vortexed and centrifuged at 4°C at 13 500 rpm for 5 min. An aliquot of 200 µL was taken and stored at -80 °C for further GC- and LC-MS analysis. Derivatization and analyses of metabolites were performed by a GC-MS 7890A mass spectrometer (Agilent, Santa Clara, USA) as described.[9] Metabolites were identified in comparison to Metabolomic Discoveries' database entries of authentic standards. The LC separation was performed using hydrophilic interaction chromatography with a ZIC-HILIC 3.5 µm, 200 A column (Merck Sequant, Umeå Sweden), operated by an Agilent 1290 UPLC system (Agilent, Santa Clara, USA). The LC mobile phase was A) 95% Acetonitril; 5% 10 mM Ammoniumacetat and B) 95% 10 mM Ammoniumacetat; 5% Acetonitril with a gradient from 95 % A to 72 % A at 7 min, to 5 % at 8 min, followed by 3 min wash with 5 % A. The flow rate was 400 µL/min, injection volume 1 µL. The mass spectrometry was performed using a 6540 QTOF/MS Detector and an AJS ESI source (Agilent, Santa Clara, USA). The intensity of the measured metabolite was normalized to internal standards. Most relevant metabolites were validated by a targeted approach (ECCPS Metabolomic Core Facility, Goethe University, Frankfurt am Main, Germany). Briefly, analysis of metabolites was performed by LC-MS/MS using a QTrap 5500 mass spectrometer (Sciex, Darmstadt, Germany). The reversed-phase LC separation was performed using a Waters Acquity HSS T3 column (150 mm × 2.1 mm, 1.8 µm (Waters, Eschborn, Germany)) at 40°C, operated by an Agilent 1290 Infinity pump system (Agilent, Waldbronn, Germany). The LC mobile phase was A) 100% milliQ water with 0.15% formic acid and B) 100% acetonitrile with 0.15% formic acid. Starting condition for the separation was 98% solvent A hold for 1.5 min, followed by a 3 min gradient to 100% solvent B, followed by a cleaning and equilibration step, making 10 min total LC run time. The flow rate was 400 µL/min, injection volume 2.5 µL. Calibration curves were performed with authentic standards. The intensity of the measured metabolite was normalized to internal standards. Additionally ELISA according to manufacturer´s instructions (α-ketoglutarate/Pyruvate – Biovision; Glucose - Cell Biolabs, Inc) was

performed. Colorimetric and fluorimetric signal were detected by a plate reader (EnSpire® Multimode Plate Reader – Perkin Elmer).

Computational modeling. The crystallographic structure of TDG protein in complex with DNA identified by PDB ID 4Z47 was selected as starting point for MD simulations, because it is solved at the highest resolution and is endowed with the less number of gaps among crystallographic TDG structures available in the Protein Data Bank (www.rcsb.org/pdb).[10] The structure of DNA bearing mismatched carboxylcytosine in the TDG catalytic site (DNA-fC) was also retrieved from the crystallographic structure coded by PDB ID 3UO7.[11] Protein and nucleic acids were parametrized by the AMBER force field ff14SB,[12] whereas αKG was parametrize by the General Amber Force Field (GAFF)[13] αKG's point charges were calculated by *antechamber* using the am1-bcc level of theory.[14] Bond lengths, angle and dihedral values, and partial charges of the formylcytosine nucleobase were computed by the HF functional in conjunction with the 6- 311++G (d,p) basis set, after geometry optimization performed at the same level of theory. *Ab initio* calculations were performed by Gaussian 03 (revision C.02).[15] For MD simulations purposes, each system studied in this work was solvated in a cubic box of TIP3P water molecules buffering 8 Å from the surface of the macromolecule. Periodic boundary conditions were applied. The total charge of each system was neutralized by the addition of Cl^- or Na^+ counter-ions, whereas the pKa of protein residues was computed by the *H++* software (version 3.2 - http://biophysics.cs.vt.edu/H++).[16, 17] As in previous studies,[18-21] water molecules were energy minimized for 1500 steps using the Steepest Descent algorithm (SD) and a further 3500 steps using the Conjugate Gradient algorithm (CG), while keeping the solute as fixed. Removing the constraints, the solvated solute was energy minimized for 2000 steps using the SD and 8000 steps using the CG before being heated at constant volume from 0 to 300 K over 120 ps and using the Langevin thermostat. A density equilibration was carried out at constant pressure (NPT ensemble) for 120 ps, before running the production of unbiased MD trajectories for 200 ns. Trajectory analyses including clustering, imaging, RMSD and distance measurements were performed by *cpptraj*,[22] whereas energy minimization and MD simulations were carried out by Amber14 and run on a Nvidia Tesla C2075 GPU.[23, 24] The binding free energies were estimated by means of the Molecular Mechanics Poisson-Boltzmann Surface Area (MM-PBSA) approach implemented in Amber14.[25, 26] The electrostatic surface potential was computed with APBS[27, 28]. Theoretical -pKd values were calculated for aKG binding to wt- and R275A-TDG in representative snapshots from MD trajectories.

Chemistry. Commercially available reagents and solvents were used without further purification, unless otherwise noted. Reaction progress, was monitored by TLC on pre-coated silica plates (Merk 60 F254, 250 μm thickness) and spots were stained by KMnO4 (0.5 g in 100 mL 0.1 N NaOH) and UV light. Melting points were measured with a capillary apparatus (Büchi 540). 1H and 13C NMR spectra were recorded with a Bruker Avance 300 at 300 and 75 MHz respectively. Chemical shifts (δ) are given in ppm relative to tetramethylasilane, used as internal standard. 1H NMR coupling constants (J) are reported in Herz (Hz) and multiplicity is indicated as follows: s, singlet; bs, broad singlet; d, doublet; m, multiplet; Low resolutions mass spectra were recorded on Finnigan-Mat TSQ-700 in chemical ionization (CI) using isobutane. Purity was checked by LC system (Dionex Ultimate 3000 UPLC from Thermo) using gradient of 5-95% Acetonitrile / Water + 0.1% of formic acid and X-Bridge 50 mm x 2.1 mm x 3.5 um column with a flow rate of 0.8 mL/min and was > 99%. Analysis was performed by HRMS (Bruker MicrOTOF II). Compounds 1 – 27 (Extended data 5, panel d) were labelled and synthesized as previously described.[29]

(S)-2-[(2,6-dichlorobenzoyl)amino]succinic acid (AA6). 2,6-Dichlorobenzoic acid (2.00 g; 10.5 mmol) was dissolved in $SOCl_2$ (20 mL; 102 mmol) and heated at 70°C for 18 h. Excess $SOCl_2$ was evaporated under reduced pressure and the residual acyl chloride was co-evaporated with THF (3 x 30 mL). The resulting yellowish oil was dissolved in 1,4-dioxane (10 mL) and added dropwise to a solution of L-aspartic acid (1.40 g; 10.5 mmol) and Na_2CO_3 (2.65 g; 25.0 mmol) in H_2O (10 mL). The reaction mixture was stirred for 18 h at RT, treated with HCl (1.0 M, 30 mL) and extracted with EtOAc (3 x 30 mL). The combined organic fractions were washed with brine (30 mL), dried over anhydrous Na_2SO_4 and concentrated under reduced pressure.
The residue was purified by flash column chromatography on silica gel eluting with CH_2Cl_2/MeOH 98:2. The fraction containing the desired product was concentrated under reduced pressure affording 1.22 g (38%) of AA6 as a white solid. Mp 162.7 – 163.2°C ($CHCl_3$ / EtOH). 1H NMR (DMSO-d6) δ (ppm) = 2.60 – 2.85 (m, 2H, CH2COOH), 4.71 (m, 1H, NHCH), 7.39 - 7.49 (m, 3H, $C_6H_3Cl_2$), 9.11 (d, J = 6.0 Hz, 1H, NH), 12.64 (bs, 2H, 2 COOH). 13C NMR (DMSO-d6) δ (ppm) = 36.7, 49.7, 128.9, 131.9, 132.1, 136.8, 164, 172.3, 172.6. MS (CI, i-Bu): (m/z %): 306/308/310 [MH+]. HRMS calcd. for $C_{11}H_{10}Cl_2NO_5$ (m/z) [MH+] 305.9931; found 305.9948.

TDG and TET-1 mutants TDG^{R275A} and $TET\text{-}1^{R2043A}$ mutants were originated using Q5® Site-Directed Mutagenesis Kit (New England BioLabs) according to manufacturer's condition. Briefly, TDG (Myc-DDK-tagged)-Human thymine-DNA glycosylase (TDG) (Origene) and FH-TET1-pEF (Addgene) plasmids were used as template for PCR-site directed mutagenesis. The following

mutagenized primers were designed with NEBase Changer:

TDG R275A FW	5’ - ATCCAGTGCAGCATGTGCTCAGTTTC-3’
TDG R275A REV	5’- GATGGCATAACATAGCAG - 3’
TET1 R2043A FW	5’ - TCATCCAACCGCCCTCTCCCTTGTCTTTTAC - 3’
TET1 R2043A REV	5’ - TTACGGTTGGGGTGCTCA - 3’

After PCR, the amplified material was incubated for 5 min at RT directly to a unique Kinase-Ligase-DpnI (KLD) enzyme to allow circularization and template removal. Then, 5 µL of the reaction was transformed into high-efficiency NEB 5-alpha Competent *E.coli* bacteria, spread onto a specific selection plates (Kan^r for TDG and Amp^r for TET1) and incubated overnight at 37°C. Single positive colonies were then isolated using QIAprep Spin Miniprep Kit (Qiagen) and screened for correct mutations through Sanger sequencing.

CRISPR/Cas9. To knock out TDG the following target-specific sgRNAs were used:

Primer set	Forward oligo	Reverse oligo
h_TDG_1	caccgGGCATAAACCCGGGACTAA	aaacTTAGTCCCGGGTTTATGCCc
h_TDG_2	caccgCTGGAGAGATCTTTGCTGC	aaacGCAGCAAAGATCTCTCCAGc
r_TDG_1	caccgGGCATCAACCCAGGATTAA	aaacTTAATCCTGGGTTGATGCCc
r_TDG_2	caccgACTTGCGAGACCAGCTGAA	aaacTTCAGCTGGTCTCGCAAGTc

The target-specific sgRNAs were cloned into LentiCRISPR2 vector (Addgene, Cambridge, MA) using the GoldenGate protocol. All CRISPR/Cas9 experiments were compared to non-targeting control (NTC) obtained with the following sgRNAs cloned into the LentiCRISPR2 vector using the GoldenGate protocol:

Primer set	Forward oligo	Reverse oligo
NTC	caccgTTCCGGGCTAACAAGTCCT	aaacAGGACTTGTTAGCCCGGAAc

The obtained plasmids were transformed into NEB 5-alpha Competent E. coli (High Efficiency – New England Biolabs), then DNA was purified by E.Z.N.A. Fastfilter Endo-Free Plasmid DNA Maxi Kit (Omega biotek), and a concentration of 1 µg was used for transfection. After 48 h, transfected HEK293T or H9C2 cells were selected by respectively 0.5 µg or 0.25 µg puromycin. After recovery from selection, HEK293T or H9C2 cells were tested for TDG knockout by western blot.

Small interference RNA: Knockdown of TDG and TET1 expression in the CMSCs was achieved by siRNA targeting human TDG and TET1 (100 nM, Santa Cruz). Scrambled RNA sequence was

used as control. Transfection was performed by siPORT NeoFX Tranfection Agent (Ambion) according to the instructions of the manufacturer.

Immunoprecipitation and Western Blot. Co-immunoprecipitations were performed using 500 µg extracts after lysis of samples in 50 mM Tris-HCl (pH 7.4), 250 mM NaCl, 1% Triton X-100, 1% Empigene-BB supplemented with 1 mM PMSF and protease inhibitor mix using 4 µg of anti-TDG (Genetex), anti-TET1 (Genetex), anti-myc (Cell Signaling). The Ademtech Bioadembeads paramagnetic beads system was used to immunoprecipitate the specific proteins according to the manufacturer's instructions. Western blotting was performed by standard procedures after cell lysis in RIPA or Laemmli buffer. Nitrocellulose blotting membranes were probed with the following antibodies: TET-1 (Genetex); TDG (Genetex); OGDH (Genetex); Irs-1 (Santa Cruz); Irs-2 (Santa Cruz); myc (Cell Signaling); Mfn1 (Santa Cruz); Drp1 (Cell Signaling); CML (R&D); GAPDH (Abcam); flag (Sigma); α-tubulin (Cell Signaling). The list of all used antibodies is provided in Online Table VIII. Development was performed by Odyssey CLx reader (LI-COR).

Enzymatic Activity assay TET, TDG, OGDH and IDH activity were evaluated by specific ELISA activity assays according to manufacturer´s instructions (TET: Epigenase 5mC-Hydroxylase TET Activity/Inhibition Assay Kit - Epigentek; TDG: Thymine DNA Glycosylase (TDG) Activity/Inhibition Assay Kit - Epigentek; OGDH: Alpha-Ketoglutarate Dehydrogenase Activity Colorimetric Assay Kit – Biovision; IDH: Isocitrate Dehydrogenase Activity Colorimetric Assay Kit - Biovision). αKG disodium salt (Sigma) was used for cell lysates and recombinant protein treatments during assays. The level of TDG activity has been evaluated on myc-TDG^{R275A} mutant after immunoprecipitation of transfected HEK293T cells. Briefly, 500 µg of myc-TDG wt or myc-TDG^{R275A} have been immunoprecipitated with anti-myc antibody (Cell Signaling) according to Ademtech Bioadembeads paramagnetic beads manufacturer's instructions. All the incubations have been performed at +4°C to preserve the enzymatic activity.

Thermal Shift Assay (TSA) and Cellular Thermal Shift Assay (CETSA). TSA and CETSA were performed according to standard protocols.[30, 31] For CETSA briefly, cellular extract was freshly prepared in RIPA buffer (10 mM Tris HCl pH 7.4, 150 mM NaCl, 1% Igepal, 1% sodium deoxycholate (DOC), 0.1% sodium dodecyl sulfate (SDS), 0,1% glycerol, protease and phosphatase inhibitors cocktail, and 2mM 1,4-dithiothreitol (DTT)). Homogenization was performed by 3 cycles of freeze-thawing. The soluble fraction was separated from debris by centrifugation at 20000xg for 20 min at 4°C. Cell lysates were divided into two aliquots, with one aliquot being treated with the

compound of interest and the other aliquot exposed to solvent (control). After 30 min incubation at RT the lysates were divided into smaller (25 µg) aliquots and heated individually at the reported temperatures for 3 min followed by 3 min cooling at RT. The heated lysates were centrifuged at 20000xg for 20 min, at 4°C in order to separate the soluble fractions from precipitates. All supernatants were transferred into new microtubes and analyzed by western blotting decorated with the specific primary antibody of interest. αKG (Sigma) was used at 1 mM concentration using water as solvent; (S)-2-[(2,6-dichlorobenzoyl)amino]succinic acid (AA6) was used at 0,5 mM after solubilization in DMSO.

TDG glycosylase activity assay. DNA substrates for enzymatic activity were prepared by annealing equimolar amount of the following oligonucleotides:

Top_G	5’ - ACG ATT GCC GTC GAG TAC CTA CGA GCC TGA TCG ATC _G_AT CGC TAA TGT CCG GCT AGA AGC GAT TCC GTA CGA - 3’
Cy5.5_Bot_T	5’- TCG TAC GGA ATC GCT TCT AGC CGG ACA TTA GCG AT_T_ GAT CGA TCA GGC TCG TAG GTA CTC GAC GGC AAT CGT - 3’

The Bot_T oligo was 5´ cold-labelled with Cyanine 5.5 (Cy5.5) to allow detection by the Odyssey CLx Infrared Imaging System (LI-COR Biosciences). The annealing buffer: 10 mM Tris-HCl (pH 7,5), 1 mM EDTA and 100 mM NaCl. The reaction buffer: 20 mM Tris-HCl (pH 7,65), 50 mM NaCl, 5% glycerol, 1 mM DTT, 0,1 µg/µL BSA. 100 nM of DNA substrates were incubated 30 min at 37°C with 500 ng of recombinant TDG and in the presence or absence of 20 µM αKG. The reaction was halted by adding 1 µL of 1M NaOH and 10 µL Formamide buffer (90% Formamide , 10 mM EDTA, 0,1% blue bromophenol). The mixtures were heated 5 min at 95°C before loading on 15% TBE polyacrylamide gel. Running was performed in TBE 1x, at 100 V for 1 h. Detection was performed by Odyssey CLx Infrared Imaging System (LI-COR Biosciences) at 700 nm.

Electrophoretic mobility shift assay (EMSA). Binding reaction mixtures were prepared with 100 mM Tris-HCl (pH 8), 10 mM EDTA, 1 M NaCl, 50% glycerol, 1 mM DTT, 0,1 µg/µL BSA and 100 nM of Top_G, Cy5.5_Bot_T oligos and recombinant 250 ng TDG protein in the presence or absence of 20 µM αKG (Sigma). The binding reaction time was 15 min at RT. Samples were immediately loaded on a 15% denaturing TBE polyacrylamide gel and run at 100 V for 30 min. Detection was performed by Odyssey CLx Infrared Imaging System (LI-COR Biosciences) at 700 nm.

TDG-ARP competition experiments: 500 ng of DNA substrates were incubated 30 min at 37°C with 500 ng of recombinant TDG and in the presence or absence of 20 µM αKG. The reaction buffer

was: 20 mM Tris-HCl (pH 8), 50 mM NaCl, 5% glycerol, 1 mM DTT, 0.1 μg/μL BSA. After TDG-DNA pre incubation, DNA was incubated with ARP at 37°C for 1 h to tag the DNA AP site. AP sites were then detected following the standard protocol of the DNA Damage Detection Kit (PromoKine).

Mitochondrial Function. Mitochondrial function has been evaluated by JC-1 Mitochondrial Membrane Potential kit (Cayman Chemical) according to manufacturer´s instructions. Signal was detected by ELISA using a plate reader (EnSpire® Multimode Plate Reader – Perkin Elmer). Extracellular oxygen consumption rates (OCR) have been evaluated by the fluorescent-based OCR assay kit (Abcam) according manufacturer´s instructions. Briefly, ND/D-CMSCs were treated with Octyl-α-ketoglutarate 20 μM or AA6 10 μM. DMSO was used as solvent. The fluorescent signal was detected every minute for 1 h by multi-well plate reader (EnSpire® Multimode Plate Reader – Perkin Elmer) set at 37°C, Ex/Em=380/650. Signals were normalized for total DNA content by DRAQ5 (1:1000, Biostatus).

Recombinant protein. The commercially available, active full length recombinant mouse N-terminal His-tagged TDG protein (Diagenode) was used for TDG activity assay, TSA, Glycosylase activity assay, EMSA and TDG-ARP competition experiments.

Immunofluorescence and Confocal Microscopy. Confocal analysis was performed as reported previously.[32] Paraffin embedded and cryosection samples have been prepared according to standard histological procedures. anti-TET-1 (1:150, monoclonal, Genetex), anti-TDG (1:150, polyclonal, Genetex), anti-5hmC (1:150, polyclonal, Active Motif; 1:200, monoclonal, Genetex), anti-5fC (1:150, polyclonal, Active Motif), anti-Vimentin (1:200, monoclonal, ProGen), anti-Troponin C (1:200, polyclonal, Santa Cruz) were used. The list of all used antibodies is provided in Online Table VIII. Mitochondria have been visualized by MitoTracker Red CMXRos (1:2000, Thermo Scientific) and JC-1 (5 μM, AdipoGen). Samples were analyzed using a Leica TCS SP8 confocal microscope.

Data availability. All relevant data are available from the authors. The RNA and DNA sequencing datasets generated and analyzed during the current study will be available in the GEO repository.

Statistical analysis. Statistical analyses were performed using GraphPad Prism programme. Sample sizes (n) were reported in the corresponding figure legend. The present study is exploratory and primarily mechanistic. For all analyses, the observer was blind to the identity of the samples. Non

parametric student's t-test, 1-way and 2-way ANOVA were used to analyze variables. A value of $p \leq 0.05$ was deemed statistically significant. Mean values are indicated ± SE.

1. Moore A, Shindikar A, Fomison-Nurse I, Riu F, Munasinghe PE, Ram TP, Saxena P, Coffey S, Bunton RW, Galvin IF, Williams MJ, Emanueli C, Madeddu P, Katare R. Rapid onset of cardiomyopathy in stz-induced female diabetic mice involves the downregulation of pro-survival pim-1. *Cardiovascular diabetology*. 2014;13:68
2. Kilkenny C, Browne W, Cuthill IC, Emerson M, Altman DG, Group NCRRGW. Animal research: Reporting in vivo experiments: The arrive guidelines. *Br J Pharmacol*. 2010;160:1577-1579
3. Rossini A, Frati C, Lagrasta C, Graiani G, Scopece A, Cavalli S, Musso E, Baccarin M, Di Segni M, Fagnoni F, Germani A, Quaini E, Mayr M, Xu Q, Barbuti A, DiFrancesco D, Pompilio G, Quaini F, Gaetano C, Capogrossi MC. Human cardiac and bone marrow stromal cells exhibit distinctive properties related to their origin. *Cardiovascular research*. 2011;89:650-660
4. Barbati SA, Colussi C, Bacci L, Aiello A, Re A, Stigliano E, Isidori AM, Grassi C, Pontecorvi A, Farsetti A, Gaetano C, Nanni S. Transcription factor crem mediates high glucose response in cardiomyocytes and in a male mouse model of prolonged hyperglycemia. *Endocrinology*. 2017
5. Tahiliani M, Koh KP, Shen Y, Pastor WA, Bandukwala H, Brudno Y, Agarwal S, Iyer LM, Liu DR, Aravind L, Rao A. Conversion of 5-methylcytosine to 5-hydroxymethylcytosine in mammalian DNA by mll partner tet1. *Science*. 2009;324:930-935
6. Bolger AM, Lohse M, Usadel B. Trimmomatic: A flexible trimmer for illumina sequence data. *Bioinformatics*. 2014;30:2114-2120
7. Dobin A, Davis CA, Schlesinger F, Drenkow J, Zaleski C, Jha S, Batut P, Chaisson M, Gingeras TR. Star: Ultrafast universal rna-seq aligner. *Bioinformatics*. 2013;29:15-21
8. Liao Y, Smyth GK, Shi W. Featurecounts: An efficient general purpose program for assigning sequence reads to genomic features. *Bioinformatics*. 2014;30:923-930
9. Lisec J, Schauer N, Kopka J, Willmitzer L, Fernie AR. Gas chromatography mass spectrometry-based metabolite profiling in plants. *Nature protocols*. 2006;1:387-396
10. Malik SS, Coey CT, Varney KM, Pozharski E, Drohat AC. Thymine DNA glycosylase exhibits negligible affinity for nucleobases that it removes from DNA. *Nucleic Acids Res.* 2015;43:9541-9552
11. Zhang L, Lu XY, Lu JY, Liang HH, Dai Q, Xu GL, Luo C, Jiang HL, He C. Thymine DNA glycosylase specifically recognizes 5-carboxylcytosine-modified DNA. *Nat. Chem. Biol.* 2012;8:328-330
12. Maier JA, Martinez C, Kasavajhala K, Wickstrom L, Hauser KE, Simmerling C. Ff14sb: Improving the accuracy of protein side chain and backbone parameters from ff99sb. *J. Chem. Theory Comput.* 2015;11:3696-3713
13. Wang JM, Wolf RM, Caldwell JW, Kollman PA, Case DA. Development and testing of a general amber force field. *J. Comput. Chem.* 2004;25:1157-1174
14. Wang JM, Wang W, Kollman PA, Case DA. Automatic atom type and bond type perception in molecular mechanical calculations. *J. Mol. Graph. Model.* 2006;25:247-260
15. Frisch MJT, G. W.; Schlegel, H. B.; Scuseria, G. E.; Robb, M. A.; Cheeseman, J. R.; Montgomery, Jr., J. A.; Vreven, T.; Kudin, K. N.; Burant, J. C.; Millam, J. M.; Iyengar, S. S.; Tomasi, J.; Barone, V.; Mennucci, B.; Cossi, M.; Scalmani, G.; Rega, N.; Petersson, G. A.; Nakatsuji, H.; Hada, M.; Ehara, M.; Toyota, K.; Fukuda, R.; Hasegawa, J.; Ishida, M.; Nakajima, T.; Honda, Y.; Kitao, O.; Nakai, H.; Klene, M.; Li, X.; Knox, J. E.; Hratchian, H.

P.; Cross, J. B.; Bakken, V.; Adamo, C.; Jaramillo, J.; Gomperts, R.; Stratmann, R. E.; Yazyev, O.; Austin, A. J.; Cammi, R.; Pomelli, C.; Ochterski, J. W.; Ayala, P. Y.; Morokuma, K.; Voth, G. A.; Salvador, P.; Dannenberg, J. J.; Zakrzewski, V. G.; Dapprich, S.; Daniels, A. D.; Strain, M. C.; Farkas, O.; Malick, D. K.; Rabuck, A. D.; Raghavachari, K.; Foresman, J. B.; Ortiz, J. V.; Cui, Q.; Baboul, A. G.; Clifford, S.; Cioslowski, J.; Stefanov, B. B.; Liu, G.; Liashenko, A.; Piskorz, P.; Komaromi, I.; Martin, R. L.; Fox, D. J.; Keith, T.; Al-Laham, M. A.; Peng, C. Y.; Nanayakkara, A.; Challacombe, M.; Gill, P. M. W.; Johnson, B.; Chen, W.; Wong, M. W.; Gonzalez, C.; Pople, J. A.;. Gaussian 03, revision c.02. *Gaussian, Inc., Wallingford CT*. 2004

16. Anandakrishnan R, Aguilar B, Onufriev AV. H++ 3.0: Automating pk prediction and the preparation of biomolecular structures for atomistic molecular modeling and simulations. *Nucleic Acids Res.* 2012;40:W537-541
17. Myers J, Grothaus G, Narayanan S, Onufriev A. A simple clustering algorithm can be accurate enough for use in calculations of pks in macromolecules. *Proteins-Structure Function and Bioinformatics*. 2006;63:928-938
18. Cau Y, Fiorillo A, Mori M, Ilari A, Botta M, Lalle M. Molecular dynamics simulations and structural analysis of giardia duodenalis 14-3-3 protein-protein interactions. *J. Chem. Inf. Model.* 2015
19. Infante P, Mori M, Alfonsi R, Ghirga F, Aiello F, Toscano S, Ingallina C, Siler M, Cucchi D, Po A, Miele E, D'Amico D, Canettieri G, De Smaele E, Ferretti E, Screpanti I, Uccello Barretta G, Botta M, Botta B, Gulino A, Di Marcotullio L. Gli1/DNA interaction is a druggable target for hedgehog-dependent tumors. *EMBO J.* 2015;34:200-217
20. Mori M, Dietrich U, Manetti F, Botta M. Molecular dynamics and dft study on hiv-1 nucleocapsid protein-7 in complex with viral genome. *J. Chem. Inf. Model.* 2010;50:638-650
21. Mori M, Nucci A, Lang MC, Humbert N, Boudier C, Debaene F, Sanglier-Cianferani S, Catala M, Schult-Dietrich P, Dietrich U, Tisne C, Mely Y, Botta M. Functional and structural characterization of 2-amino-4-phenylthiazole inhibitors of the hiv-1 nucleocapsid protein with antiviral activity. *ACS Chem. Biol.* 2014;9:1950-1955
22. Roe DR, Cheatham TE, 3rd. Ptraj and cpptraj: Software for processing and analysis of molecular dynamics trajectory data. *J. Chem. Theory Comput.* 2013;9:3084-3095
23. Salomon-Ferrer R, Gotz AW, Poole D, Le Grand S, Walker RC. Routine microsecond molecular dynamics simulations with amber on gpus. 2. Explicit solvent particle mesh ewald. *J. Chem. Theory Comput.* 2013;9:3878-3888
24. D.A. Case, T.A. Darden, T.E. Cheatham I, C.L. Simmerling, J. Wang, R.E. Duke, R. Luo, R.C. Walker, W. Zhang, K.M. Merz, B. Roberts, S. Hayik, A. Roitberg, G. Seabra, J. Swails, A.W. Goetz, I. Kolossváry, K.F. Wong, F. Paesani, J. Vanicek, R.M. Wolf, J. Liu, X. Wu, S.R. Brozell, T. Steinbrecher, H. Gohlke, Q. Cai, X. Ye, J. Wang, M.-J. Hsieh, G. Cui, D.R. Roe, D.H. Mathews, M.G. Seetin, R. Salomon-Ferrer, C. Sagui, V. Babin, T. Luchko, S. Gusarov, Kovalenko A, Kollman PA. Amber 14, university of california, san francisco. 2015
25. Mori M, Manetti F, Botta M. Predicting the binding mode of known ncp7 inhibitors to facilitate the design of novel modulators. *J. Chem. Inf. Model.* 2011;51:446-454
26. Miller BR, McGee TD, Swails JM, Homeyer N, Gohlke H, Roitberg AE. Mmpbsa.Py: An efficient program for end-state free energy calculations. *J. Chem. Theory Comput.* 2012;8:3314-3321
27. Baker NA, Sept D, Joseph S, Holst MJ, McCammon JA. Electrostatics of nanosystems: Application to microtubules and the ribosome. *Proc. Natl. Acad. Sci. U. S. A.* 2001;98:10037-10041
28. Dolinsky TJ, Nielsen JE, McCammon JA, Baker NA. Pdb2pqr: An automated pipeline for the setup of poisson-boltzmann electrostatics calculations. *Nucleic Acids Res.* 2004;32:W665-W667

29. Garella D, Atlante S, Borretto E, Cocco M, Giorgis M, Costale A, Stevanato L, Miglio G, Cencioni C, de Gortari EF, Medina-Franco JL, Spallotta F, Gaetano C, Bertinaria M. Design and synthesis of n-benzoyl amino acid derivatives as DNA methylation inhibitors. *Chem Biol Drug Des*. 2016
30. Lo MC, Aulabaugh A, Jin G, Cowling R, Bard J, Malamas M, Ellestad G. Evaluation of fluorescence-based thermal shift assays for hit identification in drug discovery. *Analytical biochemistry*. 2004;332:153-159
31. Martinez Molina D, Jafari R, Ignatushchenko M, Seki T, Larsson EA, Dan C, Sreekumar L, Cao Y, Nordlund P. Monitoring drug target engagement in cells and tissues using the cellular thermal shift assay. *Science*. 2013;341:84-87
32. Spallotta F, Cencioni C, Straino S, Nanni S, Rosati J, Artuso S, Manni I, Colussi C, Piaggio G, Martelli F, Valente S, Mai A, Capogrossi MC, Farsetti A, Gaetano C. A nitric oxide-dependent cross-talk between class i and iii histone deacetylases accelerates skin repair. *J Biol Chem*. 2013;288:11004-11012

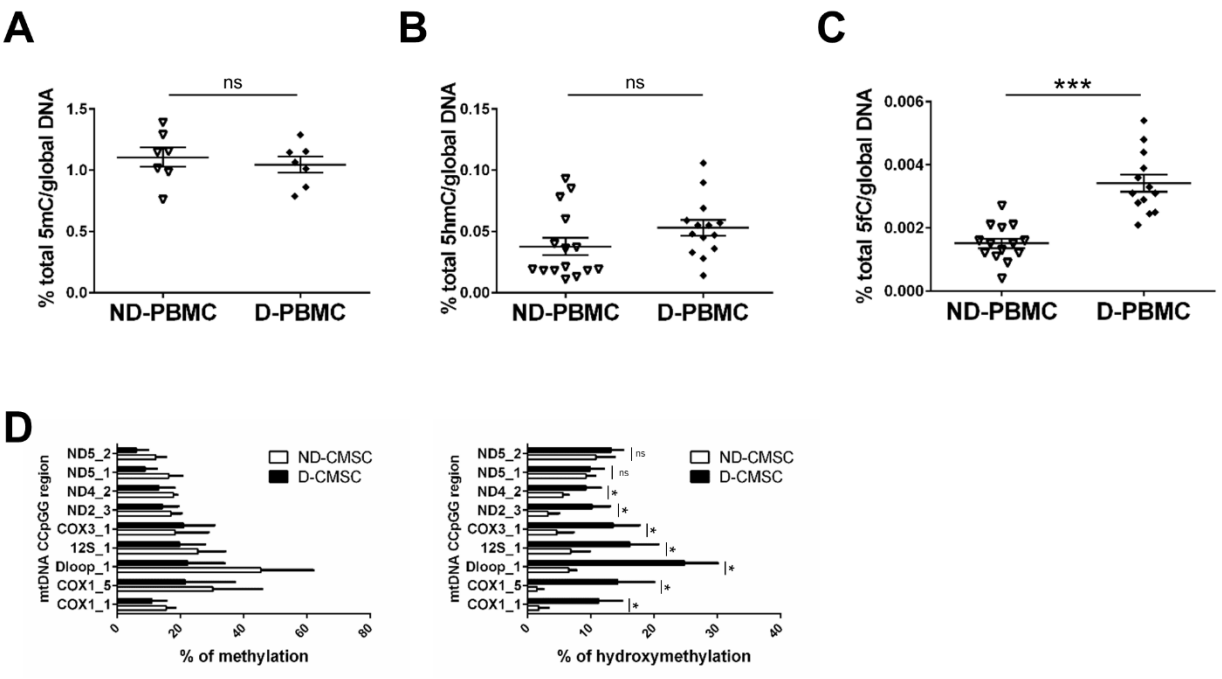

Online Figure I

Evaluation of cytosine modifications in human peripheral mononucleated cells (PBMCs) isolated from non-diabetic (ND-) and diabetic (D-) donors and in mitochondrial DNA. (A) Quantification of 5mC (n=7), **(B)** 5hmC (n=14) and **(C)** 5fC (n=13) in PBMCs isolated from ND- (white triangles) D- (black rumbles) donors. **(D)** The graphs show the percentage of enrichment in 5mC (left panel) and 5hmC (right panel) determined in CCpGG sites of the mitochondrial DNA (mtDNA) isolated from ND- (white bars) and D-CMSCs (black bars) (n=6). Error bars indicate SE. * $p < 0.05$; *** $p < 0.001$; ns: not significant. Data were analyzed by Kolmogorov-Smirnov test.

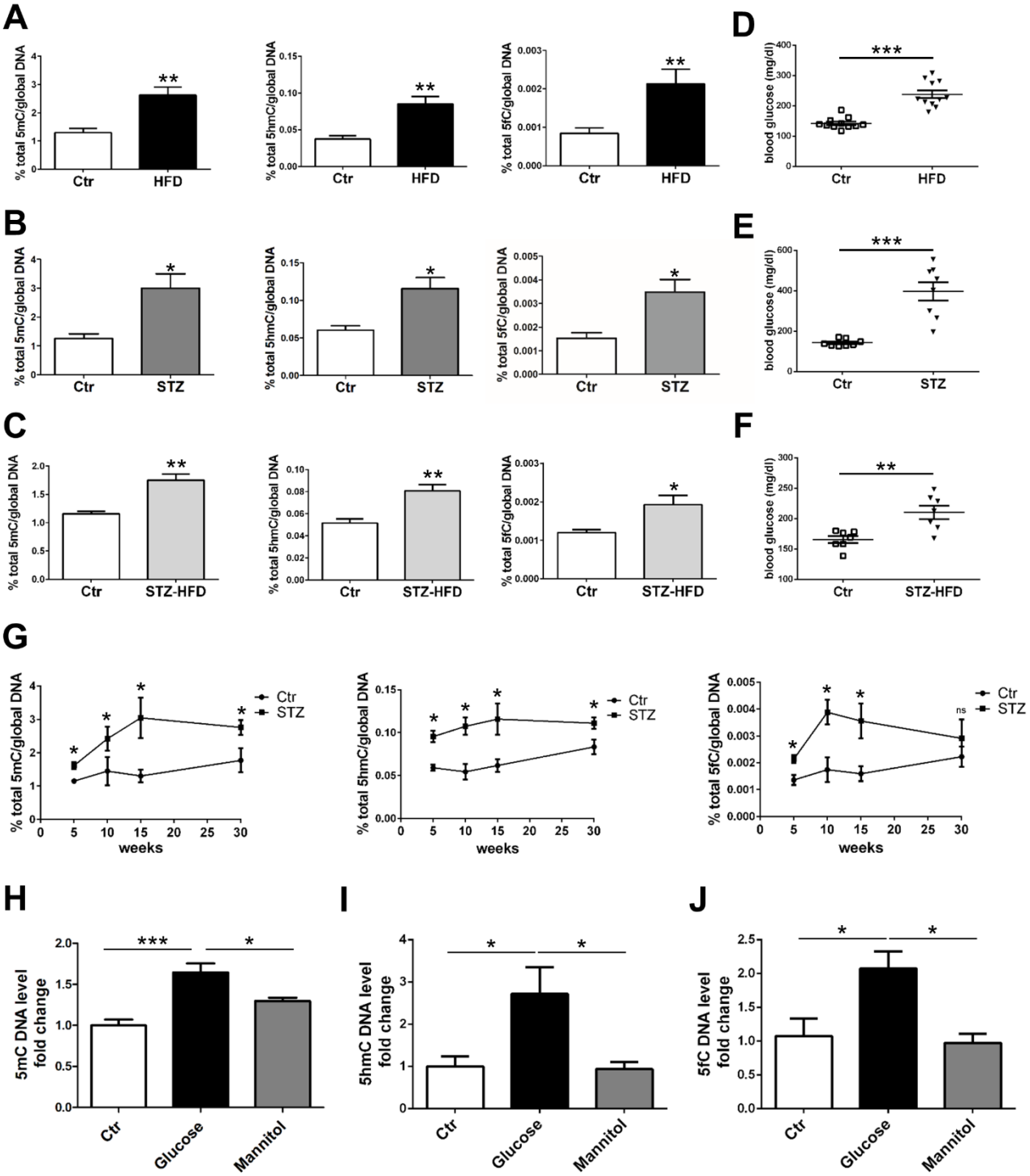

Online Figure II

Accumulation of cytosine iterative modifications in whole heart of insulin resistance, type 1, type 2 diabetic mice and in a monolayer of endothelial cells treated with high glucose. (A-C)

Whole mouse heart quantification of 5mC (left panel), 5hmC (middle panel) and 5fC (right panel). Comparison of: **(A)** Mice fed with standard diet (Ctr – white bars; n=8; 5mC: 1.30±0.15; 5hmC: 0.037±0.004; 5fC: 0.00084±0.00014) and high-fat diet (HFD – black bars; n=8; 5mC: 2.62±0.29; 5hmC: 0.085±0.010; 5fC: 0.00230±0.00037) for 15 weeks. **(B)** Streptozotocin treated mice (STZ – grey bars; n=6; 5mC: 2.99±0.49; 5hmC: 0.115±0.010; 5fC: 0.0035±0.0005) vs. control mice (white bars; n=6; 5mC: 1.25±0.16; 5hmC: 0.060±0.006; 5fC: 0.0015±0.0002). **(C)** Combination of low dose STZ followed by a HFD (STZ-HDF – light grey bars; n=7; 5mC: 1.75±0.11; 5hmC: 0.08±0.006; 5fC: 0.0018±0.0002) vs. control mice (white bars; n=7; 5mC: 1.15±0.05; 5hmC: 0.05±0.004; 5fC: 0.0012±0.0001). **(D-F)** Quantification of blood glucose levels in HFD (**D**; 238±12.98), STZ (**E**; 396±45.62) and STZ-HFD (**F**; 210±10.98) mice (black triangles) compared to controls (Ctr – white squares; **D**: 142±5.57; **E**: 142±6.19; **F**: 165±5.62). **(G)** Global cytosine modifications quantification (5mC – left panel; 5hmC – middle panel; 5fC - right panel) in a time course streptozotocin treated (STZ – black squares) and control mice (Ctr – black circles) (n=6). Numeric data are provided below. **(H-J)** Quantification of the global 5mC **(H)**, 5hmC **(I)** and 5fC **(J)** content in HUVEC monolayer maintained for 72 h in control condition (Ctr – white bars), in the presence of 25 mM glucose (black bars) or with an equivalent amount of mannitol as osmotic control (grey bar). n=5 per condition. Error bars indicate SE. * $p < 0.05$; ** $p < 0.01$; *** $p < 0.001$; ns: not significant. Data were analyzed by Kolmogorov-Smirnov test **(A, B, C, D, E, F)**, 2 way ANOVA **(G)** and 1 way ANOVA with Bonferroni post-hoc test **(H - J)**.

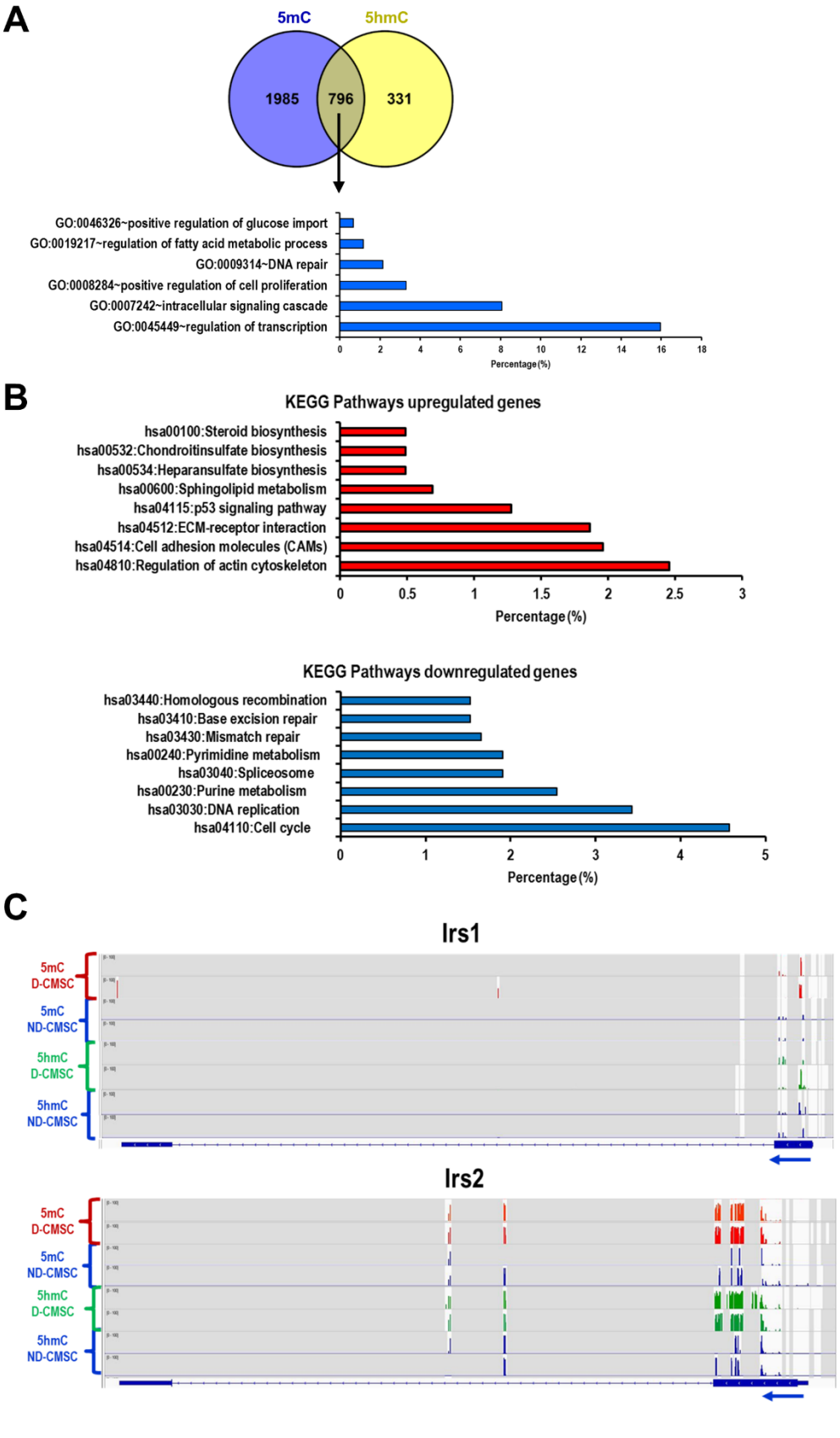
A
5mC
5hmC
1985
796
331
GO:0046326~positive regulation of glucose import
GO:0019217~regulation of fatty acid metabolic process
GO:0009314~DNA repair
GO:0008284~positive regulation of cell proliferation
GO:0007242~intracellular signaling cascade
GO:0045449~regulation of transcription
0 2 4 6 8 10 12 14 16 18
Percentage (%)
B
KEGG Pathways upregulated genes
hsa00100:Steroid biosynthesis
hsa00532:Chondroitinsulfate biosynthesis
hsa00534:Heparansulfate biosynthesis
hsa00600:Sphingolipid metabolism
hsa04115:p53 signaling pathway
hsa04512:ECM-receptor interaction
hsa04514:Cell adhesion molecules (CAMs)
hsa04810:Regulation of actin cytoskeleton
0 0.5 1 1.5 2 2.5 3
Percentage (%)
KEGG Pathways downregulated genes
hsa03440:Homologous recombination
hsa03410:Base excision repair
hsa03430:Mismatch repair
hsa00240:Pyrimidine metabolism
hsa03040:Spliceosome
hsa00230:Purine metabolism
hsa03030:DNA replication
hsa04110:Cell cycle
0 1 2 3 4 5
Percentage (%)
C
Irs1
5mC D-CMSC
5mC ND-CMSC
5hmC D-CMSC
5hmC ND-CMSC
Irs2
5mC D-CMSC
5mC ND-CMSC
5hmC D-CMSC
5hmC ND-CMSC

Online Figure III

Reduced representation of bisulfite genomic sequencing analysis. (A) Venn diagram depicting the distribution of hyper-methylated (5mC, purple; 5hmC, yellow) promoters in D- compared to ND-CMSCs. Lower panel: GO analysis of promoter regions bearing both modifications. **(B)** KEGG Pathways analysis of differentially regulated transcripts between ND- and D-CMSCs. Up-regulated genes are depicted in the upper panel, red bar graph; down-regulated genes are represented in the lower panel, blue bar graph. **(C)** Plots showing detailed peak positioning as determined by 5mC-seq and 5hmC-seq data for Irs1 (upper panels) and Irs2 (lower panels) genes. Specifically, for each plot, 5mC-seq data related to D-CMSCs (red), 5mC-seq and 5hmC-seq data related to ND-CMSCs (blue), or 5hmC-seq related to D-CMSCs (green) were represented.

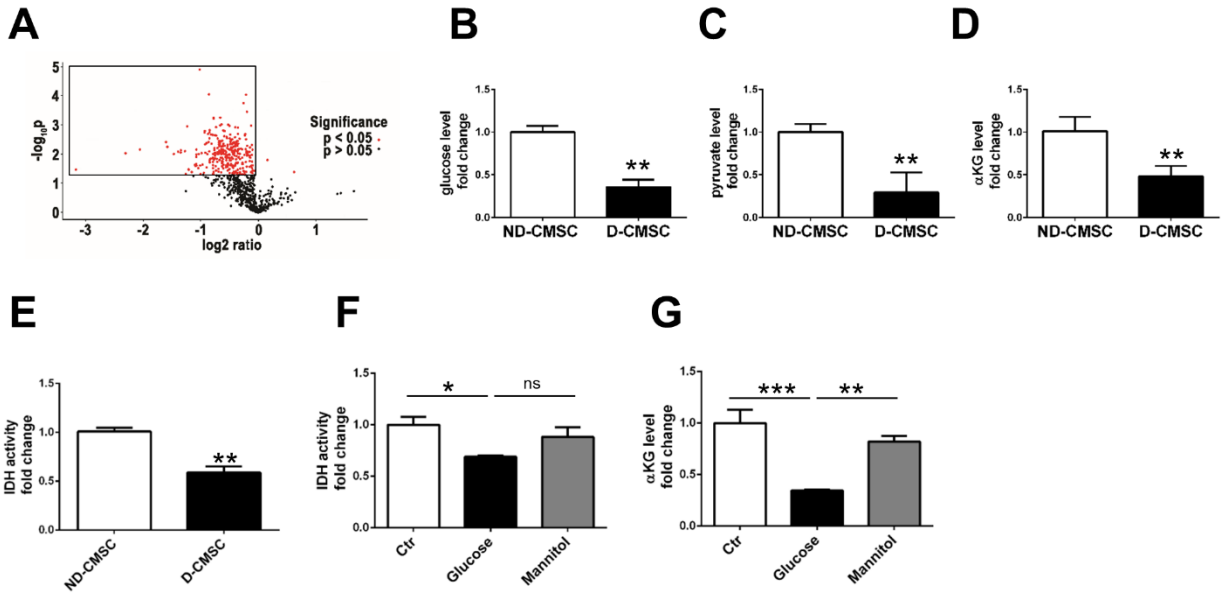

Online Figure IV

Validation of metabolomic analysis. (A) Volcano plot of differentially regulated metabolite levels of CMSCs derived from ND- or D- donors. Red dots show annotated and non-annotated metabolites with $p < 0.05$. **(B-D)** Quantification of the intracellular level of glucose (**B**, n=6), pyruvate (**C**, n=6) and α-ketoglutarate (**D**, n=10) evaluated in ND-CMSCs (white bars) and D-CMSCs (black bars). **(E)** IDH activity assay performed in ND- and D-CMSCs (n=6). **(F)** IDH activity assay performed in HUVECs cultured for 72 h in control condition (Ctr - white bar), in the presence of 25 mM glucose (black bar) and with an equivalent amount of mannitol as osmotic control (grey bar). **(G)** Quantification of αKG level in HUVECs cultured for 72 h in control condition (Ctr - white bar), in the presence of 25 mM glucose (black bar) and with an equivalent amount of mannitol as osmotic control (grey bar). Error bars indicate SE. * $p < 0.05$; ** $p < 0.01$; *** $p < 0.001$; ns: not significant. Data were analyzed by Kolmogorov-Smirnov test **(B, C, D)** and 1 way ANOVA with Bonferroni post-hoc test **(F, G)**.

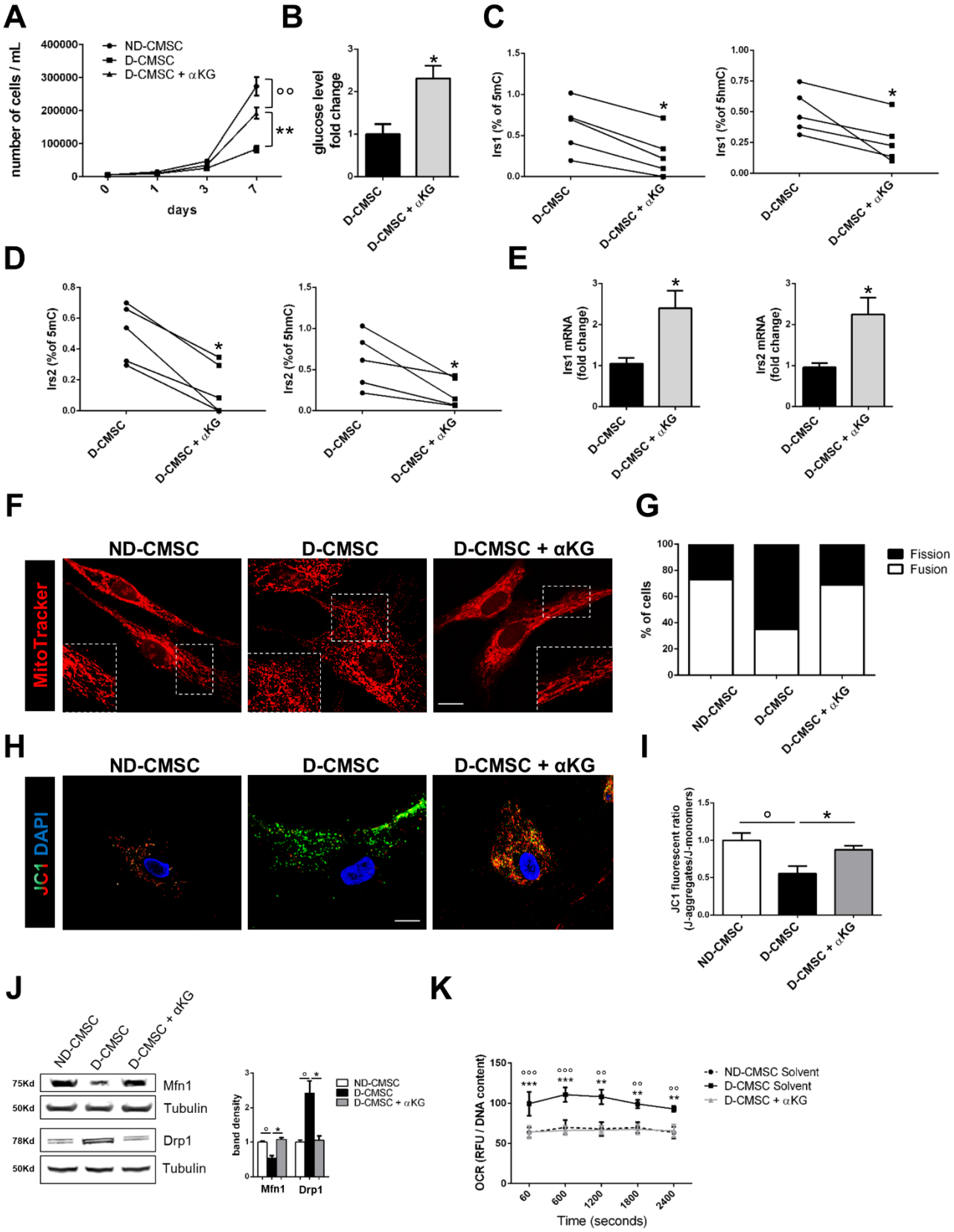
A
number of cells / mL
ND-CMSC
D-CMSC
D-CMSC + αKG
days
B
glucose level fold change
D-CMSC
D-CMSC + αKG
C
Irs1 (% of 5mC)
Irs1 (%of 5hmC)
D
Irs2 (%of 5mC)
Irs2 (%of 5hmC)
E
Irs1 mRNA (fold change)
Irs2 mRNA (fold change)
F
ND-CMSC
D-CMSC
D-CMSC + αKG
MitoTracker
G
% of cells
Fission
Fusion
H
JC1 DAPI
I
JC1 fluorescent ratio (J-aggregates/J-monomers)
J
75Kd
50Kd
78Kd
Mfn1
Tubulin
Drp1
band density
K
OCR (RFU / DNA content)
Time (seconds)
ND-CMSC Solvent
D-CMSC Solvent
D-CMSC + αKG

Online Figure V

Alpha-ketoglutarate administration ameliorates D-CMSC proliferation, glucose uptake and mitochondrial health. (A) Growth curve of ND- (black circles); D-CMSCs (black squares) and D-CMSCs + αKG (black triangles). **(B)** Quantification of glucose levels in D-CMSCs ± αKG (n=6). **(C-D)** Relative enrichment of 5mC (left panel) and 5hmC (right panel) into selected CpG island of Irs-1 **(C)** and Irs-2 **(D)** promoter after αKG treatment of D-CMSCs. **(E)** qRT-PCR analysis of Irs-1 (left panel) and Irs-2 (right panel) mRNA expression in D-CMSCs ± αKG (n=6). **(F)** Representative confocal microscopy images depicting mitochondria (MitoTracker - red) in ND- and D-CMSCs ± αKG. The insets contain enlargements of selected areas (dashed squares). Scale bar 20 μm. **(G)** The graph displays the percentage of cells containing mitochondrial fission or fusion counted in ten random fields acquired in three independent experiments. **(H)** Representative confocal microscopy images depicting the mitochondrial membrane potential in ND- and D-CMSCs ± αKG. Cells were probed by JC1 and red J-aggregated accumulated in healthy mitochondria whereas green J-monomer accumulated in poor healthy mitochondria. Scale bar 15 μm. **(I)** The graph shows J-aggregated/J-monomer quantifications in ND- and D-CMSCs ± αKG. **(J)** Left panel: representative western blot showing Mfn1 and Drp1 protein levels in ND-CMSCs and D-CMSCs ± αKG. The signal from α-tubulin antibody was used as a loading control. Right panel: relative densitometry. **(K)** Oxygen consumption rate (OCR) level quantification in ND-CMSCs, D-CMSCs ± αKG. In all experiments D-CMSCs were treated with αKG 20 μM for 7 days. Error bars indicate SE. n=6 per condition. * $p < 0.05$; ** $p < 0.01$; *** $p < 0.001$ vs D-CMSCs; ° $p < 0.05$; °° $p < 0.01$; °°° $p < 0.001$ vs ND-CMSCs. Data were analyzed by 2way ANOVA **(A, K)**, Kolmogorov-Smirnov test **(B, E, I, J)** and Wilcoxon matched-pairs test **(C, D)**.

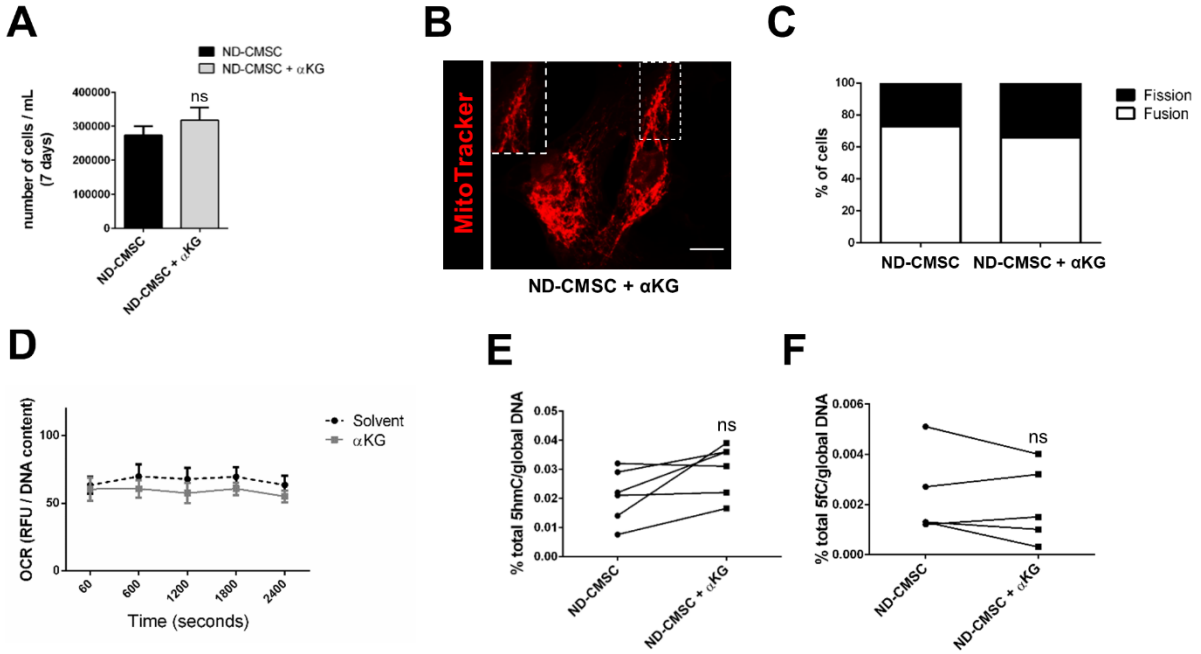

Online Figure VI

αKG effect on ND-CMSCs. (A) Graph shows the number of ND-CMSCs ± αKG 20 µM after 7 days of culture. **(B)** Representative confocal microscopy images depicting the mitochondria (MitoTracker - red) in ND-CMSCs + αKG. The insets contain enlargements of selected area (dashed squares). Scale bar 20 µm. **(C)** The graph displays the percentage of ND-CMSCs ± αKG 20 µM with mitochondrial fission or fusion counted in ten random fields acquired in three independent experiments. **(D)** Oxygen consumption rate (OCR) level quantification in ND-CMSCs ± αKG 20 µM. **(E-F)** Quantification of total 5hmC **(E)** and 5fC **(F)** in ND-CMSCs ± αKG 20 µM. Error bars indicate SE. ns: not significant. Data were analyzed by Kolmogorov-Smirnov test **(A, C)**, 2 way ANOVA **(D)** and Wilcoxon matched-pairs test **(E, F).**

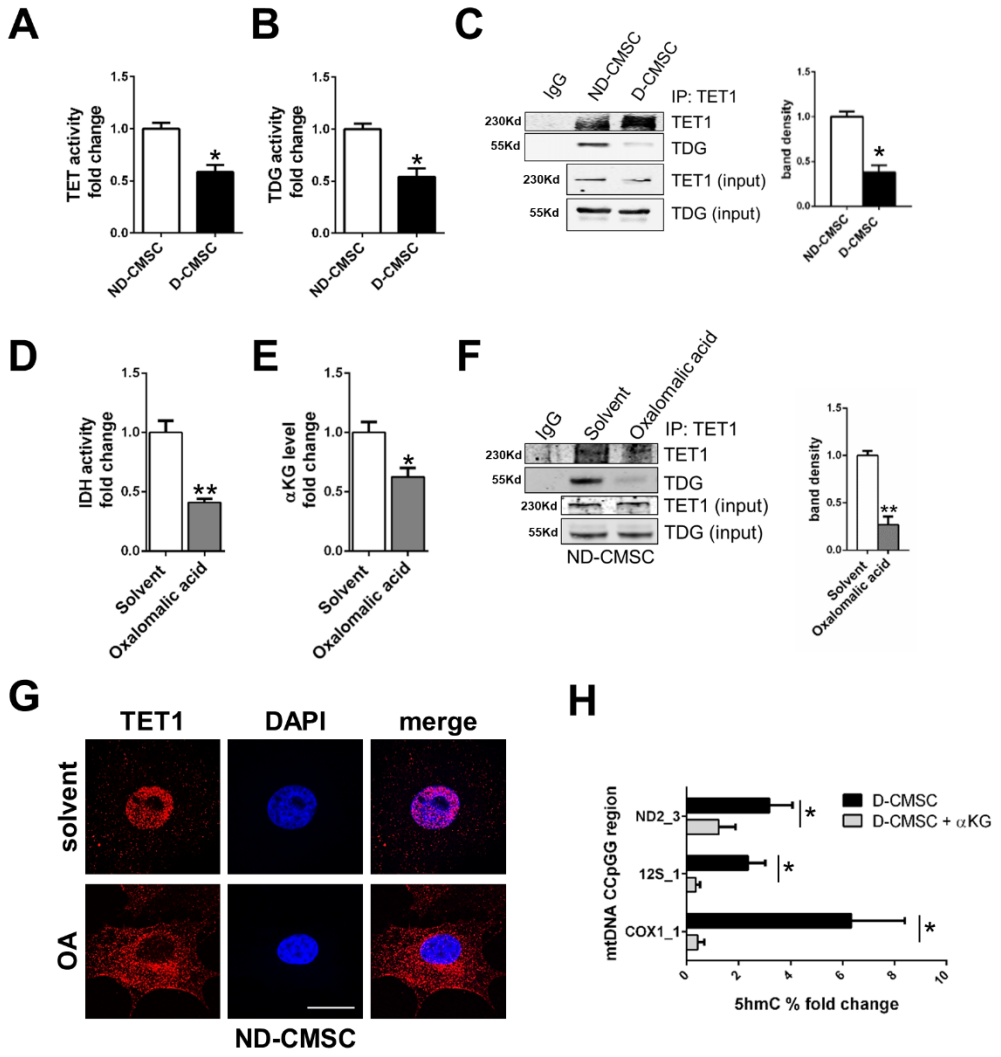

Online Figure VII

TET1/TDG association is impaired in D-CMSCs and okadaic acid delocalizes TET1 out of the nucleus. (A, B) TET **(A)** and TDG **(B)** activity level in ND- and D-CMSCs. **(C)** Representative co-immunoprecipitation (co-IP)/western blotting (WB) analysis of TET1–TDG complex formation in ND-CMSCs and D-CMSCs. Right panel: densitometry related to TDG panel obtained from three independent experiments. **(D, E)** IDH activity **(D)** and αKG levels **(E)** in ND-CMSCs cultured for 16 h in the presence of 1 mM Oxalomalic acid (grey bars). DMSO was used as solvent (white bars). **(F)** Representative co-IP/WB analysis of TET1–TDG complex performed in ND-CMSCs cultured for 16 h with 1 mM Oxalomalic acid. DMSO was used as solvent. Right panel: densitometry related to TDG

panel obtained from three independent experiments. **(G)** Representative confocal analysis depicting the subcellular localization of TET1 (red) in ND-CMSCs in presence or absence of Okadaic Acid (OA) 10 nM. Nuclei were counterstained with DAPI (blue). Scale bar 20 µm. **(H)** The graph shows the relative enrichment of 5hmC into selected CCpGG sites of the mitochondrial DNA (mtDNA) in D-CMSCs (black bars) and D-CMSCs + αKG (gray bars). Error bars indicate SE. n=6 per condition. * $p < 0.05$; ** $p < 0.01$. Data were analyzed by Kolmogorov-Smirnov test.

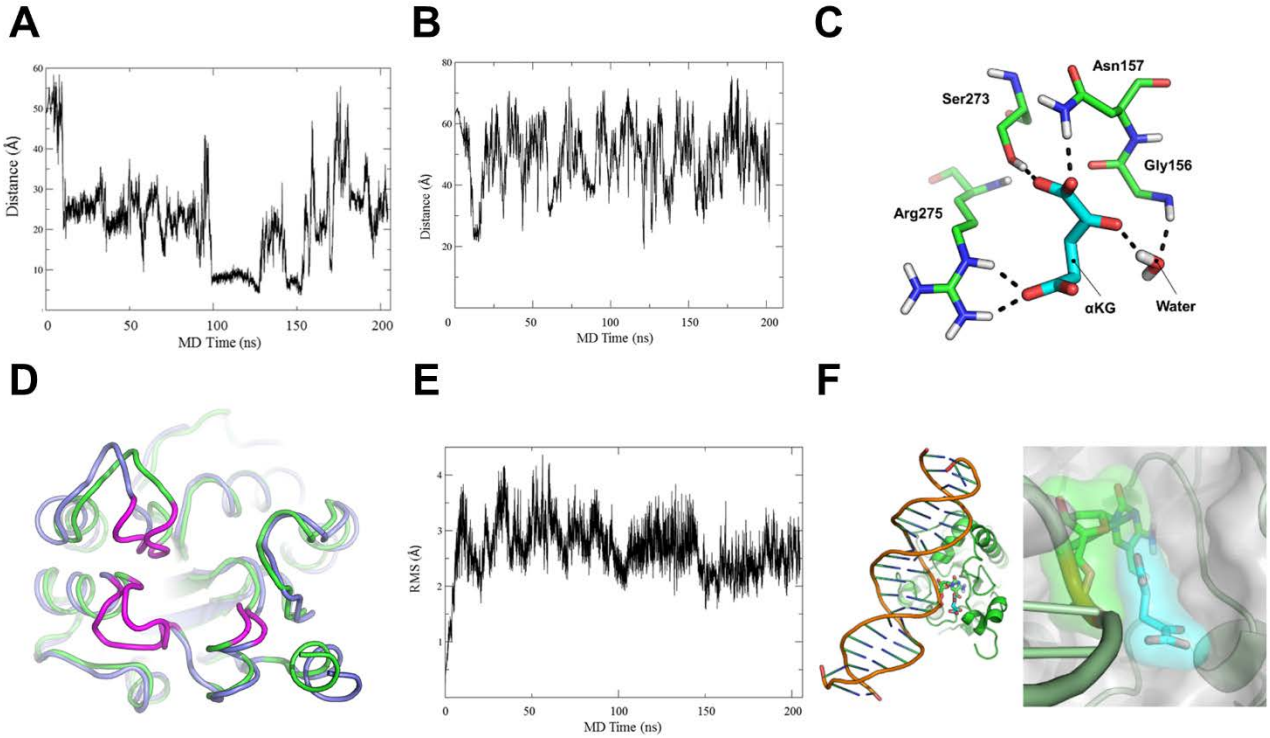

Online Figure VIII

Molecular dynamics of αKG-TDG interaction. (A) Evaluation of the distance between the centroid of the two carboxyl groups of αKG and the beta carbon of Ala275 of the R275A-TDG mutant plotted along MD simulation time. **(B)** Distance between the centroid of the two carboxyl groups of αKG and the centroid of the guanine group of the TDG Arg275 residue plotted along MD simulation time. Starting from a random distance of about 60 Å, αKG is unable to bind the TDG/DNA complex and fluctuates in the bulk solvent. **(C)** The theoretical binding mode of αKG. Residues contacted by αKG in the most populated cluster of MD frames are showed as green sticks, αKG is shown as cyan sticks, H-bonds are highlighted as black dashed lines. **(D)** Structural over-imposition between crystallographic (green) and MD-representative (blue) structure of TDG. Residues within 6 Å from the αKG -binding conformation are in magenta color. **(E)** Plot of root mean square deviation (RMSD) values of the TDG loops affected by the local conformational change in MD simulation time. The αKG binding site undergoes local conformational changes to accommodate αKG. **(F)** Structural insights into the binding of αKG to the TDG/DNA-5fC complex. Left panel: Overall structure of the ternary complex between TDG, DNA-5fC, and αKG. The

protein/DNA complex is shown as a cartoon, while the formylcytosine nucleotide and αKG are shown as green and cyan sticks, respectively. Right panel: Magnification of the TDG catalytic site simultaneously occupied by αKG and formylcytosine. DNA and protein are shown as a pale green cartoon and grey transparent surface, while the αKG and formylcytosine are shown as sticks and transparent surface to highlight the shape complementarity between the molecules.

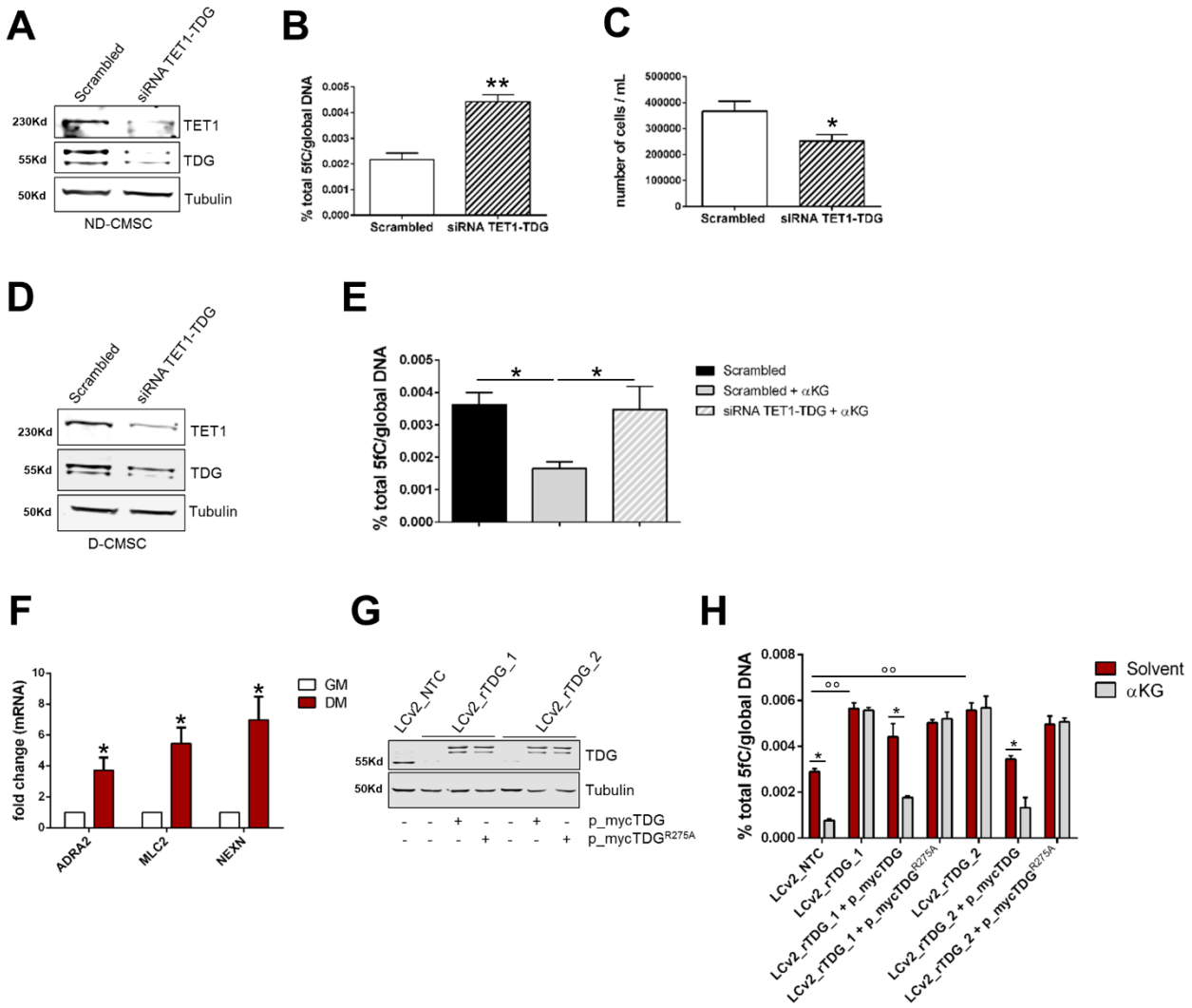

Online Figure IX

TET1/ TDG knock-down induces 5fC accumulation and abrogates αKG response in CMSCs and in H9C2 cells. (A) Representative WB shows the level of TET1 and TDG proteins in ND-CMSCs after TET1/TDG siRNA expression knockdown. Scrambled RNA has been used as control. The signal from α-tubulin antibody was used as a loading control. **(B)** Quantification of 5fC in ND-CMSCs after TET1/TDG siRNA transfection. Scrambled RNA has been used as control. **(C)** Graph shows the number of ND-CMSCs after 3 days of TET1/TDG siRNA or Scrambled RNA transfection. **(D)** Representative WB shows the level of TET1 and TDG proteins in D-CMSCs after TET1/TDG siRNA transfection. Scrambled RNA has been used as control. The signal from α-tubulin antibody was used as a loading control. **(E)** 5fC quantification in D-CMSCs after TET1/TDG siRNA expression knockdown in the presence of αKG 20 μM. Scrambled RNA has been used as control.

Scrambled cells have been treated with αKG 20 µM. **(F)** qRT-PCR analysis on cardiac markers Alpha-2A adrenergic receptor (ADRA2), Myosin regulatory light chain 2 (MLC2) and Nexilin (NEXN) in H9C2 cells maintained in growth medium (GM) or after 7 days of exposure to cardiac differentiation medium (DM). **(G)** Representative WB of TDG levels in cardiac differentiated H9C2 cells after CRISPR/Cas9 inactivation of TDG (LCv2_rTDG_1 and LCv2_rTDG_2) compare to control vector (LCv2_NTC). TDG inactivated cells have been transfected by myc-TDG and myc-TDG^{R275A} (200 ng). The signal from α-tubulin antibody was used as a loading control. **(H)** 5fC quantification in differentiated H9C2 cells transfected with LCv2_NTC, LCv2_rTDG_1 and LCv2_rTDG_2 ± myc-TDG and myc-TDG^{R275A} in presence (grey bars) or absence (dark red bars) of αKG. Error bars indicate SE. * $p < 0.05$, ** $p < 0.01$; °° $p < 0.01$ vs LCv2_NTC. Data were analyzed by Kolmogorov-Smirnov test.

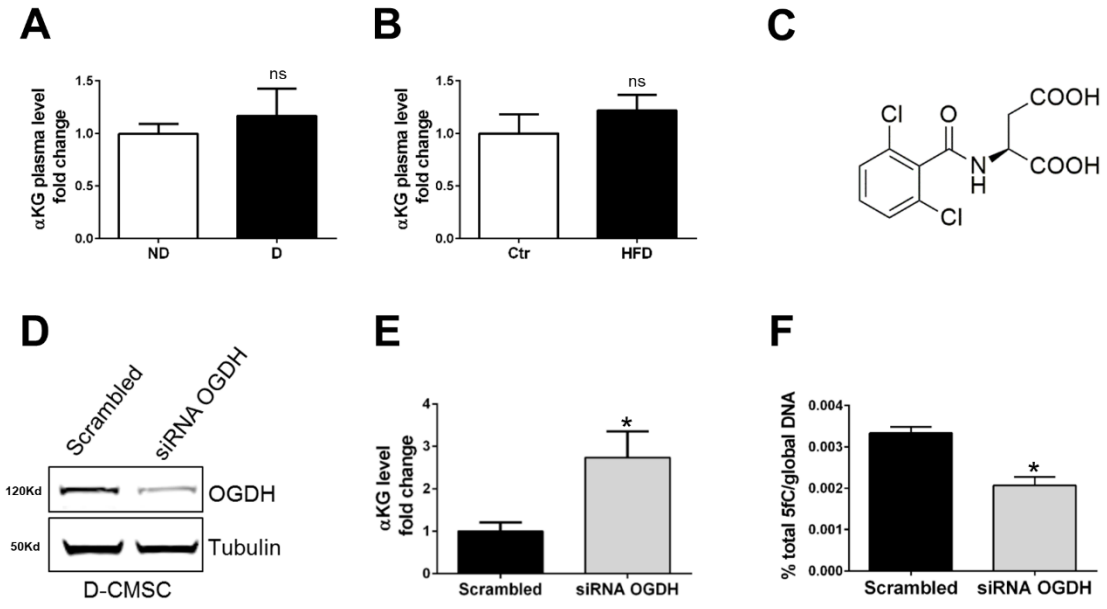

Online Figure X

Evaluation of αKG levels in donor and mouse model plasma as well as in the presence of OGDH siRNA. **(A)** Quantification of αKG plasma level in ND (white bar; 0.99±0.09) and D (black bar; 1.16±0.11) donors. n=6. **(B)** Quantification of αKG plasma levels in mice fed with standard diet (Ctr - white bar; 1.00±0.18) or HFD (black bar; 1.22±0.14). n=6. **(C)** Structure of (S)-2-[(2,6-dichlorobenzoyl)amino]succinic acid (AA6). (**D**) Representative WB shows the level of OGDH protein in D-CMSCs after OGDH siRNA transfection. Scrambled RNA has been used as control. The signal from α-tubulin antibody was used as a loading control. **(E)** Quantification of αKG level in D-CMSCs knocked down for OGDH. Scrambled cells have been used as control. **(F)** Quantification of 5fC in D-CMSCs knocked down for OGDH. Scrambled cells have been used as control. Error bars indicate SE. * $p < 0.05$; ns: not significant. Data were analyzed by Kolmogorov-Smirnov test.

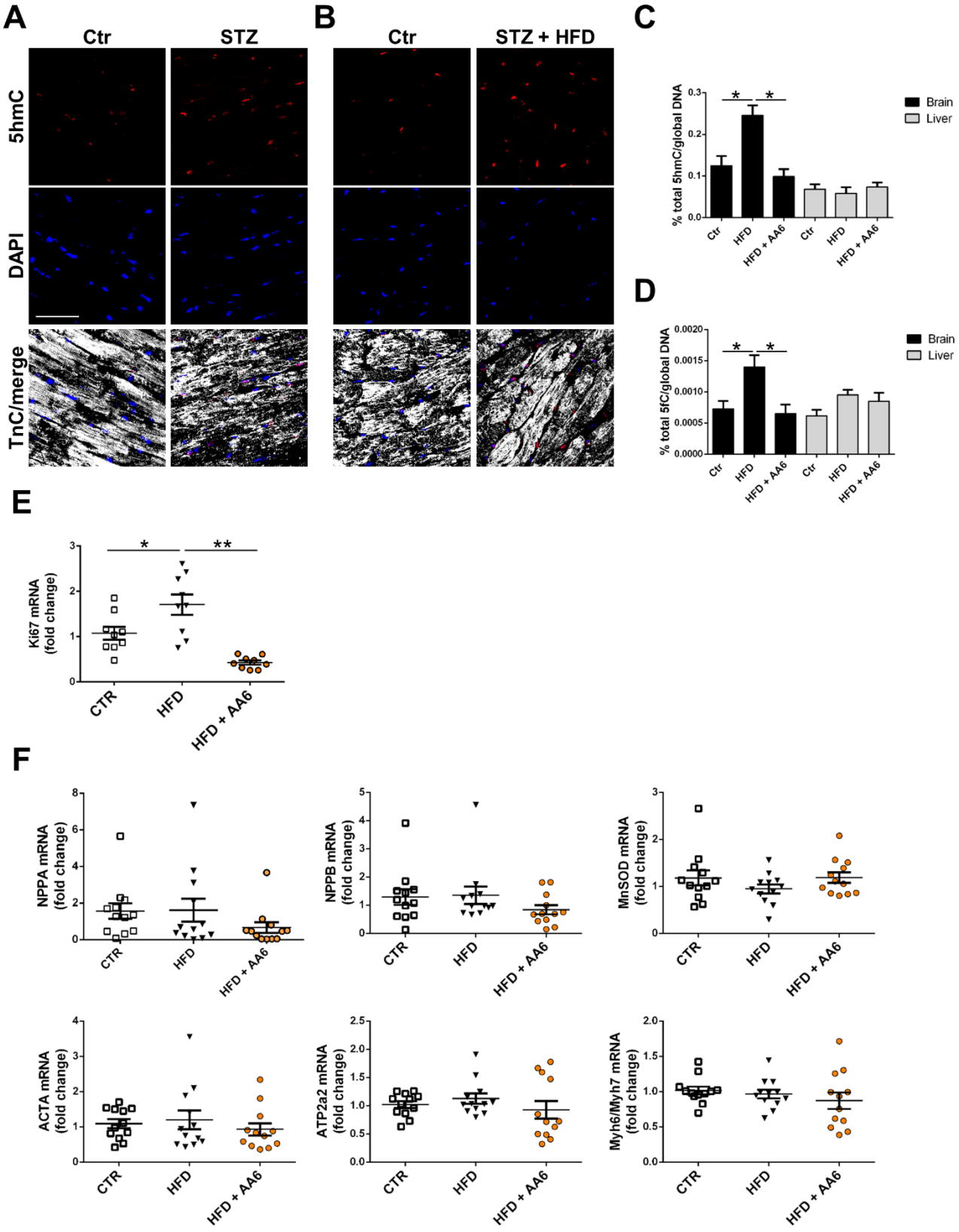
A
Ctr
STZ
5hmC
DAPI
TnC/merge
B
Ctr
STZ + HFD
C
% total 5hmC/global DNA
Brain
Liver
Ctr
HFD
HFD + AA6
D
% total 5fC/global DNA
E
Ki67 mRNA (fold change)
CTR
HFD
HFD + AA6
F
NPPA mRNA (fold change)
NPPB mRNA (fold change)
MnSOD mRNA (fold change)
ACTA mRNA (fold change)
ATP2a2 mRNA (fold change)
Myh6/Myh7 mRNA (fold change)

Online Figure XI

5hmC accumulates in the heart of STZ and STZ + HFD mice, AA6 effects on brain and liver, heart weight, proliferation and cardiotoxicity in HFD mice. (A-B) Representative confocal microscopy images depicting Ctr and STZ **(A)** and Ctr and STZ + HFD **(B)** heart. Cardiac tissue was probed by an anti-5hmC antibody (red; monoclonal) and anti-Troponin C (TnC, white; polyclonal). Nuclei were counterstained by DAPI (blue). Scale bar 45 µm. **(C-D)** Quantification of 5hmC **(C)** and 5fC **(D)** in brain and liver obtained from Ctr (**C** brain: 0.12±0.02; liver: 0.07±0.01; **D** brain: 0.00072±0.00013; liver: $0.00061 \pm 9.4 \times 10^{-5}$), HFD (**C** brain: 0.24±0.02; liver: 0.05±0.01; **D** brain: 0.00140±0.00019; liver: $0.00095 \pm 8.4 \times 10^{-5}$) and HFD + AA6 (**C** brain: 0.09±0.01; liver: 0.07±0.01; **D** brain: 0.00065±0.00014; liver: 0.00085±0.00013) treated mice. **(E)** qRT-PCR analysis on proliferative marker Ki67 in Ctr (white squares; 1.07±0.14), HFD (black triangles; 1.71±0.22) and HFD + AA6 (orange circles; 0.43±0.04) mouse heart. **(F)** qRT-PCR analysis on cardiotoxicity markers in Ctr (white squares), HFD (black triangles) and HFD + AA6 (orange circles) mouse heart: Natriuretic peptide A and B (NPPA, Ctr: 1.56±0.43 HFD: 1,61±0.63 HFD+AA6: 0.66±0.29; NPPB, Ctr: 1.29±0.28 HFD: 1.35±0.30 HFD+AA6: 0.84±0.16); Manganese superoxide dismutase (MnSOD, Ctr: 1.18±0.16 HFD: 0.95±0.09 HFD+AA6: 1.19±0.11); Sarcomeric actin (ACTA, Ctr: 1.09±0.12 HFD: 1.20±0.26 HFD+AA6: 0.93±0.17); ATPase2 A2 (ATP2A2, Ctr: 1.02±0.06 HFD: 1.13±0.09 HFD+AA6: 0.93±0.15); Myosin heavy chain 6/7 ratio (MHC6/7, Ctr: 1.01±0.05 HFD: 0.96±0.06 HFD+AA6: 0.87±0.11). Error bars indicate SE. * $p < 0.05$; ** $p < 0.01$; ns: not significant. Data were analyzed by Kolmogorov-Smirnov test **(C, D, F, G)** and 1 way ANOVA **(E)**.

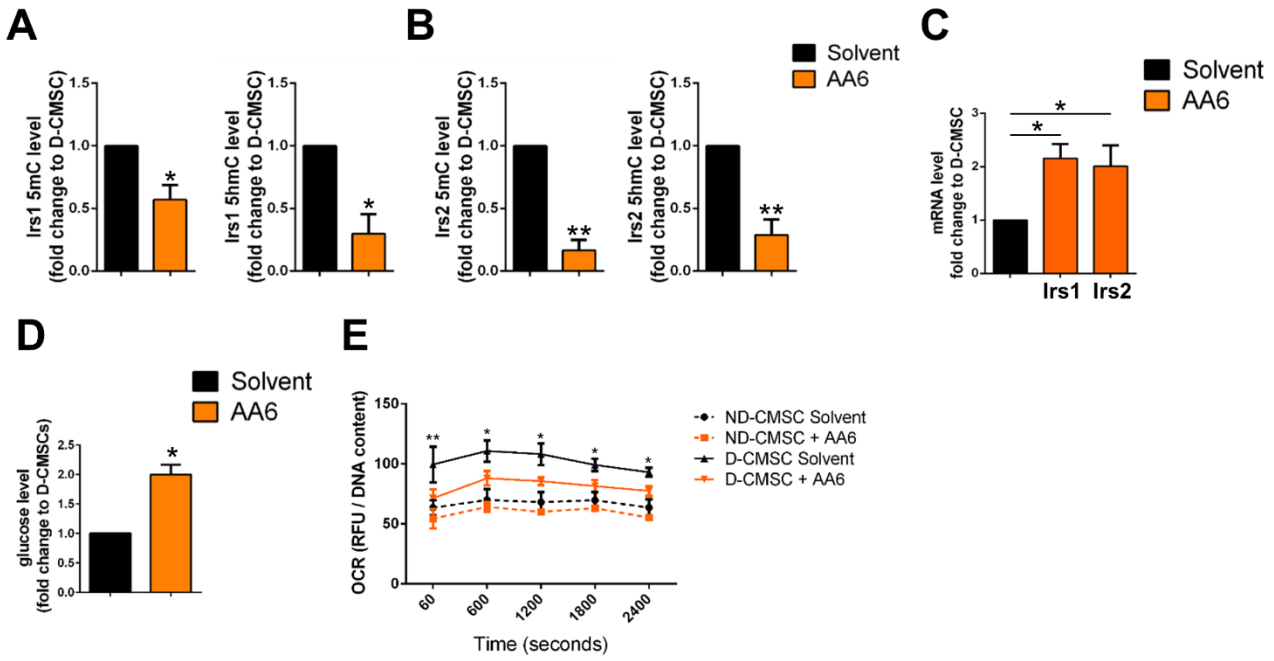

Online Figure XII

AA6 induces Irs1/2 expression via gene de-methylation/hydroxymethylation and normalizes intracellular glucose content, OCR and proliferation in D-CMSCs. (A-B) Relative enrichment of 5mC and 5hmC into selected CCpGG sites of Irs-1 **(A)** and Irs-2 **(B)** promoter after AA6 treatment of D-CMSCs (n=4). **(C)** qRT-PCR analysis of Irs-1 and Irs-2 mRNA expression in D-CMSC ± AA6 (n=6). **(D)** Glucose level quantification in D-CMSCs ± AA6 (n=6). **(E)** Oxygen consumption rate (OCR) level quantification in ND-CMSCs and D-CMSCs ± AA6 10 µM. DMSO has been used as solvent control. Error bars indicate SE. * $p < 0.05$; ** $p < 0.01$; ns: not significant. Data were analyzed by Kolmogorov-Smirnov test **(A, B, C, D, F)** and 2 way ANOVA **(E)**.

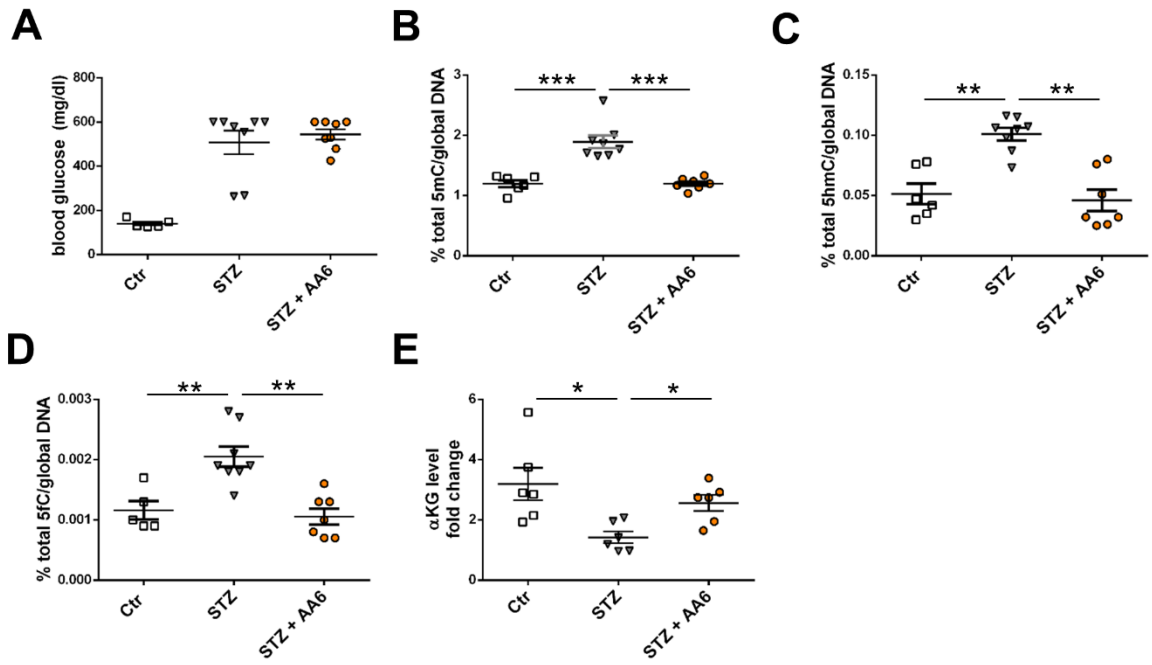

Online Figure XIII

Evaluation of blood glucose, DNA demethylation and αKG synthesis in the heart of STZ hyperglycemic mice. (A) Total blood glucose (mg/dL) measured in plasma of STZ mice after three months of hyperglycemia. Data have been obtained in control condition (Ctr, white squares; 144±8.2) and in the absence (STZ, grey triangles; 506±53)/ presence (STZ+AA6, orange circles; 543±23) of AA6. **(B-D)** Evaluation of methylated (**B**, Ctr: 1.19±0.05; STZ: 1.89±0.10; STZ+AA6: 1.19±0.03**)**, hydroxymethylated (**C**, Ctr: 0.05±0.008; STZ: 0.10±0.005; STZ+AA6: 0.05±0.008) and formyl cytosines (**D,** Ctr: 0.0011±0.00015; STZ: 0.0020±0.00015; STZ+AA6: 0.0010±0.00013) in controls (white squares) and in the absence (grey triangles) or presence (orange circles) of AA6. **(E)** αKG content in total heart lysates of STZ mice kept in control condition (Ctr, white squares; 3.19±0.54) and in the absence (STZ, grey triangles; 1.42±0.19) / presence (STZ+AA6, orange circles; 2.56±0.26) of AA6. Error bars indicate SE. * $p < 0.05$; ** $p < 0.01$; *** $p<0.005$; Data were analyzed by Kolmogorov-Smirnov test.

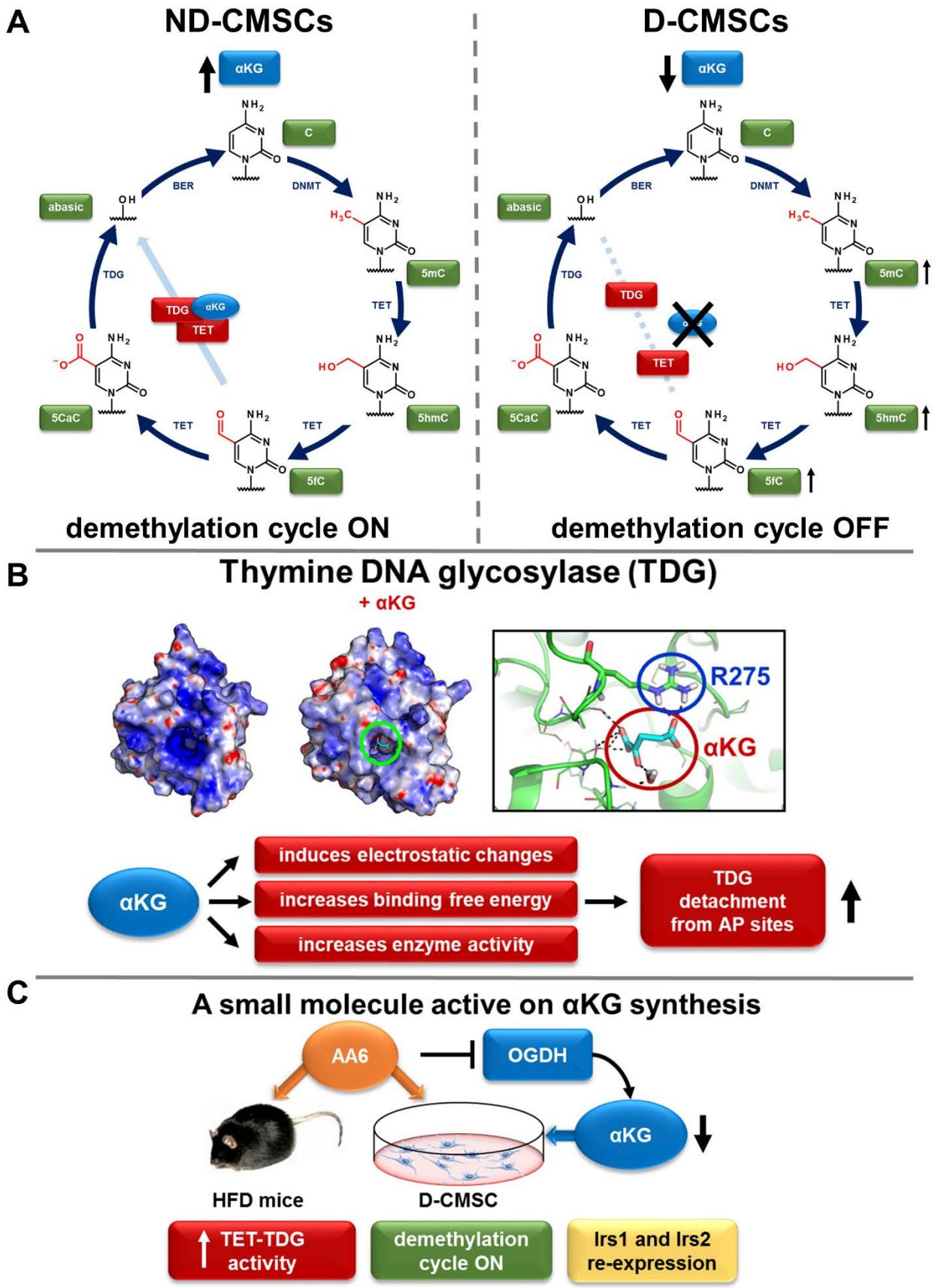
A
ND-CMSCs
D-CMSCs
αKG
C
BER
DNMT
abasic
5mC
TDG
TET
5CaC
5hmC
5fC
demethylation cycle ON
demethylation cycle OFF
B
Thymine DNA glycosylase (TDG)
+ αKG
R275
αKG
induces electrostatic changes
increases binding free energy
increases enzyme activity
TDG detachment from AP sites
C
A small molecule active on αKG synthesis
AA6
OGDH
αKG
HFD mice
D-CMSC
TET-TDG activity
demethylation cycle ON
Irs1 and Irs2 re-expression

Online Figure XIV

Consequences of αKG-TDG interaction. **(A)** αKG stabilizes TET-TDG complex during demethylation cycle in ND-CMSCs (left panel). In D-CMSCs low intracellular level of αKG leads to reduced efficiency or arrests demethylation cycle. TET-TDG complex is destabilized and oxidative forms of methylated 5´cytosine accumulate in mitochondrial and genomic DNA (right panel). **(B)** αKG acts as a TDG allosteric activator recognizing the highly conserved residue R275. **(C)** *In vitro* and *in vivo* αKG synthesis is increased by the OGDH inhibitor AA6. The drug rescues TET-TDG function, DNA demethylation cycle inducing Irs1 and Irs2 re-expression.